THE HONG KONG POLYTECHNIC UNIVERSITY

Department of Electrical Engineering

MOTION AND FORCE CONTROL IN HIGH-PERFORMANCE VARIABLE RELUCTANCE FINGER GRIPPER

by

Kenneth Kin-Chung Chan

A thesis submitted

in partial fulfilment of the requirements

for the Degree of Doctor of Philosophy

November 2004

CERTIFICATE OF ORIGINALITY

I hereby declare that this thesis is my own work and that, to the best of my knowledge and belief, it reproduces no material previously published or written, nor material that has been accepted for the award of any other degree or diploma, except where due acknowledgement has been made in the text.

_____ (Signed)

Kenneth Kin-Chung CHAN (Name of student)

Abstract

Gripper mechanism is commonly found in industrial applications. An ideal gripper should have a simple and low-cost structure, fast and robust response. Various types of grippers have been designed but none of them is capable of fulfilling the requirements of an ideal gripper. Variable Reluctance (VR) actuator has a simple and robust structure, therefore it has been used in low-cost industrial applications. Together with its high-torque density in compared with classical DC motors, VR actuator can be a very attractive solution in gripping mechanism. However, due to its nonlinear characteristics, high-precision gripping applications tend to avoid it by employing other actuators which require less control effort. As a result, VR actuator is not popular in both industrial application and academic research. Due to the recent advancement of semiconductor components and micro-processors, more complex simulation model and advanced controller can be realized. In the past few years, VR actuators have regained much research attention.

The project aims to investigate the feasibility of employing VR technology in precision two-finger gripping application. Under this overall goal, initial research efforts have been devoted to the analysis of VR actuator operating principles and the actual gripper design. Results have shown that torque density can be raised by $3-4\%$ for less than $2A$ and more than 30% with the use of mutual flux coupling effect when the pole-faces are saturated with $4A$. This is achieved by connecting the flux return paths of two single VR fingers together.

In order to fully understand the behaviour of the two-finger VR gripper prototype, detailed characterization experiments have been carried out. Flux-linkage and torque profiles are measured with Alternate Current (AC) current excitation method and direct

torque measurement respectively. Measurement results confirm that the VR gripper prototype behaves like a VR actuator and enjoys an increase in efficiency once it operates within the saturation region. Other magnetic characteristics including leakage flux, hysteresis loss and eddy current loss, and spring stiffness have also been measured.

After reviewing various modeling techniques commonly used in VR actuators, the nonlinear characteristics of the VR finger gripper, flux-linkage and torque profiles, are modeled with an exponential description function. Then, a concise dynamic nonlinear model of the VR finger gripper basing on state equations is established. This model is further verified by step responses and confirmed to be an accurate mathematical description for the VR finger gripper.

An adaptive current regulation scheme is proposed and implemented. By continuously monitoring the position and current information, flux-linkage level can be calculated with the nonlinear model. Then control parameters are varied aiming at providing fast and repeatable current responses regardless of the rotor positions. Experimental results confirm that the proposed current regulation scheme is an effective solution for adapting to the varying inductance of the VR finger gripper.

Two different control algorithms have been newly applied to tackle the nonlinearity of the VR finger gripper. The first method is to use a reduced-size nonlinear torque-current-position lookup table compensator. The main benefit of this method is simple to implement and straightforward. To further enhance the smoothness and accuracy of the table, a two dimensional interpolation scheme is proposed. Experimental results show that the proposed controller is capable of handling general applications. However, this control method fails to ensure the robustness and stability of the controlled system. In order to improve robustness qualities, a second method, the Passivity-based Control (PBC) is applied.

This nonlinear control method bases on the concept of energy transformation within a system. Moreover, the controller design of this scheme is efficient and robust. Flux-linkage

and trajectory control of the two-finger VR gripper using PBC are simulated with the mathematical model and implemented. Results show that the PBC controller is robust, offers better performance than the reduced order lookup table compensator and suitable for high-performance applications.

Finally, the two-finger VR gripper is controlled under a mixed-mode control with command scheduling. Under such arrangement, the two-finger VR gripper can be precisely controlled under closed-loop position and force control. Results show that the controller's performance is highly satisfactory with good accuracy, high trajectory performance and fast dynamic response. Conclusively, the research work confirms that the proposed two-finger VR gripper is a appropriate solution for gripping mechanism.

Acknowledgments

First of all, I would like to express my sincere appreciation and gratitude to my project supervisor, Dr. Norbert Cheung. He has always been supportive and encouraging throughout my research period. His academic guidance is extremely useful and beneficial. Without him, it would be impossible for me to fulfill my goal of pursuing for a PhD. degree.

Secondly, I would like to thank Asso. Prof. Jin-Ming Yang, a visiting Professor from South China University of Technology, Guangzhou, PRC. He has selflessly taught me the fundamental control theories. During our cooperation period, Hong Kong was severely hit by SARS, yet he never failed to visit Hong Kong every single week to teach me the control theories related to my research project.

I have to thank all my valuable friends and colleagues, who have helped me out at the times of need. Their assistances are highly appreciated.

I must also thank Prof. Daisaku Ikeda, President of Soka Gakkai International. It was his spiritual guidance that encouraged me to take up the PhD. research study and supported me to overcome through all the obstacles faced.

Lastly, I would like to thank my family and JaeYoun, my girlfriend, for their full support during my study.

Table of Contents

List of Figures

List of Tables

List of Acronyms

AC	Alternate Current
ADC	Analog-to-digital Converter
DAC	Digital-to-analog Converter
DC	Direct Current
DLR	German Aerospace Center
DSP	Digital Signal Processor
EMF	Electro-motive Force
EMI	Electro-magnetic Interference
FEM	Finite-element Method
MMF	Magneto-motive Force
MOSFET	Metal Oxide Semiconductor Field effect Transistor
EQMC	Equivalent Magnetic Circuit
PBC	Passivity-based Control
PC	Personal Computer
PCH	Port-controlled Hamiltonian
PCI	Peripheral Component Interconnect
PI	Proportional and Integral

PID	Proportional, Integral and Differential
PM	Permanent Magnet
PWM	Pulse Width Modulation
PZT	Plumbum Zirconate Titanate
RLC	Resistance, Inductance and Capacitance connected in Parallel or Series
UHV	Ultra High Voltage
VR	Variable Reluctance
VSS	Variable-Structure System

List of Symbols

B	Magnetic flux density, T
$\hat{B}$	Peak flux density, T
d	Diameter of the spring wire, m
d_{lam}	Lamination thickness of iron core, m
D_{sp}	Diameter of the spring, m
E	Elastic modulus of the spring material, kgm^{-2}
e	State error
e_{bemf}	Back emf, $Vsrad^{-1}$
e_{srh}	Search coil induced voltage, V
ϕ	Flux, Wb
F	MMF source, A
F_{imp}	Impact force, N
F_{left}	MMF source for the left finger, A
F_{right}	MMF source for the right finger, A
F_f	Force at finger tip, N
H	Magnetic field intensity, Am^{-1}
H_{total}	Hystersis loop of a magnetic circuit with air-gap

$H_{air-gap}$	Hystersis loop of a magnetic circuit constituted by air-gap
H_{core}	Hystersis loop of a magnetic circuit constituted by iron core
i	Stator current, A
i^*	Desired current, A
J	Skew symmetric matrix
J_m	Rotor inertia, kgm^2
K_{sp}	Stiffness of the torsional spring, $kgmrad^{-1}$
K_b	DC motor back EMF constant, $Vsrad^{-1}$
K_t	DC motor torque constant, $kgmA^{-1}$
K_v	Viscous damping coefficient, $kgmsrad^{-1}$
K_p	Proportional gain
K_i	Integral gain
K_d	Differential gain
l	Length of finger, m
L_l	Leakage inductance, H
L_m	Mutual inductance, H
L_s	Self inductance, H
L_a	Inductance at aligned position, H
L_u	Inductance at unaligned position, H
L_e	Electrical Lagrangian
L_{mec}	Mechanical Lagrangian
λ	Flux-linkage, Vs

λ_l	Leakage flux-linkage, Vs
λ_m	Mutual flux-linkage, Vs
λ_s	Self flux-linkage, Vs
λ_a	Flux-linkage at aligned position, Vs
λ_u	Flux-linkage at unaligned position, Vs
N	Number of turns in stator windings
N_{sp}	Number of coils in the spring
P_e	Eddy current loss at frequency f, W
P_f	Hysteresis loss at frequency f, W
P_{f0}	Hysteresis loss at frequency $f0$, W
q	Electric charge, *coulombs*
R	Dissipative matrix
R_{comm}	Reluctance of a common path within the magnetic circuit, AWb^{-1}
R_m	Resistance of stator windings, Ω
R_d	Direct-axis reluctance, AWb^{-1}
R_q	Quadrature-axis reluctance, AWb^{-1}
R_f	Fixed reluctance of magnetic circuit, AWb^{-1}
R_v	Variable reluctance of magnetic circuit, AWb^{-1}
θ	Rotor angle, rad
T_m	Rotor torque, Nm
T_{sp}	Spring torque, Nm
T_L	Load torque, Nm

W_f	Field Energy, J
W_c	Co-energy, J
ω_n	Natural frequency, $rads^{-1}$
V	Terminal voltage, *volts*
ζ	Damping ratio

Chapter 1

Introduction

1.1 Essential requirements of robotic grippers and actuators

Gripping mechanism plays an important role in material handling, factory automation and product manufacturing [32]. A large variety of gripper applications using different types of actuators are designed and employed to serve individual purposes. Typical examples of gripper actuators are:

1. DC motors
2. DC brushless motors
3. Linear motors and voice coils
4. Pneumatic actuators

Due to simplicity and compactness, most grippers have been initially dominated by Direct Current (DC) motors. With the advance of electronic commutation in recent years, DC motors are slowly replaced by DC brushless motors, which have multi-phase electronic commutation and are claimed to be maintenance free. Linear motors and voice-coils are also favorable solutions when short distance linear motions are required. However, the presence of brushes and Permanent Magnets (PMs) in the first three types of actuators reduces device reliability and robustness. Their presence also increase manufacturing complexity and overall cost. Furthermore, PMs are brittle and can be de-magnetized permanently beyond certain operating temperature. These facts hinder the usefulness

of the actuator. In addition, these PM actuators fail to offer a high power-to-size ratio compared with pneumatic actuators. Therefore, for high-force applications, pneumatic grippers are commonly used instead. Unfortunately, they fail to produce accurate gripping force with high repeatability and consistency in compared with electrical actuators.

After surveying the typical applications of grippers/actuators, the essential requirements for a good robotic gripping solution should be:

1. Low in cost.
2. Fast in force response.
3. Highly efficient, robust and accurate.
4. Maintenance free.
5. Able to operate in wide temperature range.

Surveying various existing gripper products shows that none of those available in the market is capable of fulfilling all the above mentioned requirements.

1.2 Motivation of this research project

VR motor has drawn much research attention over the past decade, mainly due to its high robustness and less-complex structure, and its potential for numerous demanding industrial applications. VR motor does not contain any PMs or brush; it is low-cost, easy-to-manufacture, highly reliable, and be able to operate in extreme temperatures. However, the VR motor has inherent nonlinear characteristics, and problems of torque-ripple and non-uniform force occur when it is driven by standard motor drives [47]. As a result, it is not widely accepted in industrial gripping applications.

During the past few years, many publications on VR motor design, commutation method, and specialized drive have emerged. VR actuators have entered the variable speed drive market [40]. These are made possible by the advancement of simulation

tools and computer control technologies. With these advancements, it is now possible to overcome most of the nonlinear problems through the redesign of the actuators magnetic circuit and the implementation of advanced control algorithm. Consequently, VR motors are beginning to be utilized in various industrial areas [23, 31, 57, 58].

Currently, typical VR applications include:

1. Electric vehicles
2. High speed fuel pumps in aircraft engines
3. High-torque robotic joints

In spite of all these developments, developing grippers using VR technology has never been explored.

The main aim of this research is to develop a novel two-finger gripper using VR technology taking the advantages of high torque efficiency, robust characteristics and simple construction. The project is motivated by following considerations:

1. VR actuators are simple in structure; it is made up of steel sheets and coil only.
2. VR actuators are extremely low-cost, robust and nearly maintenance free.
3. With the above mentioned advantages, VR actuator has a high potential to fulfill the essential requirements of a good gripper system.

This project also explores the VR actuators' potentials on high-precision gripping applications. For this type of usage, the gripper has stringent requirements on the mechanical characteristic and force profile. These investigation are seldom carried out, due to the difficulty in handling nonlinear magnetic characteristic and force profile. The work on the design and development of a high-speed and high-precision robotic gripper using VR technology would be the first of its kind.

To achieve this goal, there are some technical issues which need to be overcome:

1. To propose, design and fabricate a compact and efficient gripper structure;

2. To investigate and model the nonlinear characteristics of such a device;

3. To implement an elegant and effective nonlinear control algorithm for the position, velocity and force control of such a device.

1.3 Organization of the thesis

This research project is to investigate the present gripping mechanism and come up with an improved solution by means of VR actuators. The thesis is structured with individual chapter which focuses on a specific goal. Each chapter includes its own review of previous work, implications of the proposed work, simulation, experimental implementation and followed by a summary.

The initial stage of the research states the requirement of an ideal gripper and reviews different types of actuation techniques and their corresponding utilization in gripping mechanism. Advantages and disadvantages of their characteristics are carefully examined. Details of this work is described in Chapter 2.

Chapter 3 analyzes various arrangements of two-finger gripper using VR technology. Firstly, the basic operating principles of a VR gripper is studied. Then flux and torque production are analyzed with equivalent magnetic circuit analysis. Energy conversion analysis is then introduced to finalize the best arrangement for a two-finger VR gripper.

Then, a two-finger gripper prototype with VR technology for high-precision gripping application is constructed. Design details and its fabrication are mentioned in Chapter 4. Various flux-linkage measurement methods are compared. Measurement of flux-linkage and torque characteristics confirm that mutually coupled arrangement improves the efficiency of the VR gripper. In order to fully understand the VR finger gripper characteristics, losses of the two-finger VR gripper, including hysteresis loss, eddy current loss and leakage flux-linkage are estimated. Lastly, spring stiffness is also measured.

Modeling and simulation are critical to controller design. In order to perform

simulation with accurate results, a concise, dynamic mathematical model for the two-finger VR gripper is constructed in Chapter 5. Various flux-linkage modeling methods are reviewed. The nonlinear flux-linkage and torque characteristics are described by the exponential description method. State equations are input as block diagram and model verification is carried using step responses. Simulation and experimental results verify that the model of two-finger VR gripper is accurate.

With the proposed simulation model verified, the next step is to design a high-performance current regulation scheme. Since the load variation for VR actuators is large, in Chapter 6, an adaptive current regulation is proposed after reviewing the general current regulation schemes for VR actuated applications. The reported adaptive current regulation scheme is straightforward and can be implemented in general VR actuators especially for high precision applications. With position and current feedback, instantaneous inductance can be calculated and controller parameters are also varied to accommodate its load variation. The method was simulated and tested experimentally on the two-finger VR gripper. Results show that this method is capable in adapting to load variation and show better symmetrical current responses than classical Proportional and Integral (PI) regulation.

In order to deal with the nonlinearity of the two-finger VR gripper, two nonlinear compensation approaches are proposed in Chapter 7 and Chapter 8. The first approach is a reduced-size lookup table compensator. This approach is simple but fails to prove its global convergence and stability which leads to the need to introduce an alternative controller approach. The second approach, PBC introduced guarantees system stability and global convergence. Besides the PBC controller has a certain system robustness with respect to modeling errors and parameter variations. Results show that the PBC controller is more favorable, robust and stable under all conditions.

With the nonlinearity problem tackled, the next step is to achieve position and force control. Chapter 9 describes the detailed control block diagram for a mixed-mode control with command scheduling for position and force control of the two-finger VR

gripper. The objective is achieved mainly through switching among different modes of trajectory profiles. Besides, an S-curve trajectory command is also introduced to reduce its mechanical stress on the gripper and settling time. Results show that the gripper is stable and offer a low-cost solution for position and force (gripping) control especially for delicate objects.

Chapter 10 concludes the entire project and suggests further research directions and extensions.

1.4 Summary of contributions

This research project overcome a few obstacles using a series of innovative ideas. These contributions include:

1. Design of a tightly-coupled two-finger VR gripper based on the E-plate magnetic circuit. Efficiency of the two-finger VR gripper is raised [8];
2. Investigation of various kinds of flux-linkage measurement. Actual instrumentation is made and other magnetic properties including hysteresis and eddy current losses and leakage flux-linkage are all obtained for the two-finger VR gripper [11];
3. Construction of a concise dynamic model of the two-finger VR gripper. Model is verified with step responses and confirmed to be accurate [17];
4. Implementation of an adaptive current regulation approach for general VR motor drive systems. Implementation experiment shows that proposed approach is more favorable than classical PI current regulator [12];
5. Nonlinear controller design for two-finger VR gripper is provided with the use of PBC concept. Both simulation and experimental results show that the proposed controller is robust and offers global asymptotic stability [13];
6. Implementation of mixed-mode control with command scheduling approach. Both the simulated result and the hardware implementation result show that the proposed

gripper can perform high-speed grasping of very delicate objects with high precision. The proposed gripper also inherits many advantages of VR actuators, including ease of construction, low cost, high robustness, and high reliability [9].

Chapter 2

Structures of grippers and actuators

This chapter reviews various types of actuator techniques and their corresponding utilization in grippers. Requirements for an ideal gripper, operating principles and characteristics of various gripper technologies are presented in section 2.1. Section 2.2 describes the basic characteristics of a VR gripper. Its strengths and weaknesses are studied in section 2.3.

2.1 Types of grippers and actuators

Gripping mechanism plays an important role in material handling, automation and product manufacturing. In many industries, like the semiconductor packaging industry, the applications become increasingly demanding as their product technologies advance. These lay pressure to their manufacturing machineries. A low-cost and robust motion-system solution with high performance and reliability must be developed for these machineries.

2.1.1 Performance and characteristics of the ideal robotic gripper

An ideal gripper should be low in cost; it should have a simple structure and a high torque to current ratio. It can provide fast and accurate response and be able to operate under a wide temperature range. Furthermore, an ideal gripper must be highly robust and be maintenance free.

Numerous grippers were designed for specific gripping applications [45, 43, 42, 22, 50, 6]. These actuators exist in many forms, namely, voice coils, DC motors, DC brushless motors, piezoelectric, thermal and pneumatic actuators.

2.1.2 DC motor gripper

DC motor is compact and relatively straightforward to control. It has linear control characteristics which can be described as:

$$V = K_b\dot{\theta} \tag{2.1}$$

$$T_m = K_t i \tag{2.2}$$

where V, K_b, $\dot{\theta}$, T_m, K_t and i are terminal voltage, back Electro-motive Force (EMF) constant, angular velocity, motor torque, torque constant and armature current respectively.

From Equation 2.1 and Equation 2.2, it can be clearly seen that velocity and torque can be linearly controlled by terminal voltage and armature current respectively. As a result, DC motor had once been the most favorable solution for gripper drive systems. Figure 2.1 shows the cross sectional structure of a DC motor. PMs are mounted onto the stator, which is stationary and encloses the entire motor. Windings are wounded onto the rotor and commutated through a pair of carbon brushes.

Figure 2.2 shows one possible form of DC motor gripper. Fingers are indirectly driven

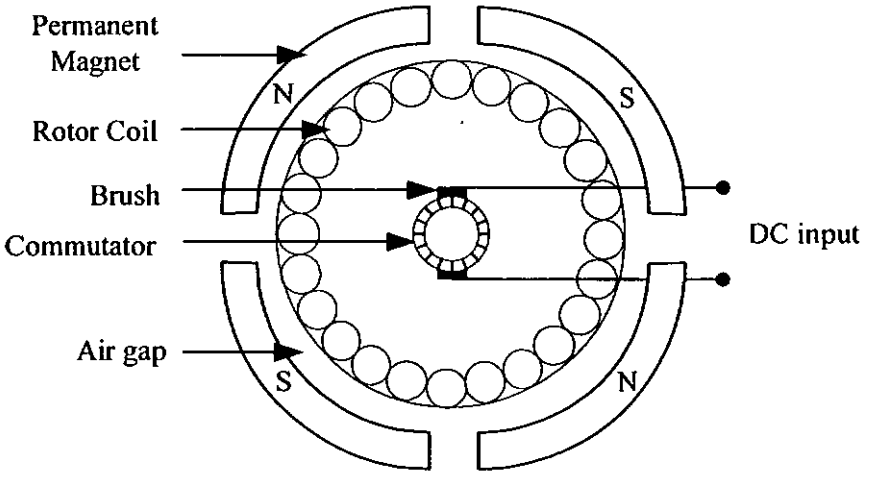

Figure 2.1: A DC motor

by a DC motor, which is connected with a gearbox. The secondary gear is linked up with a bi-directional ball screw, which couples the motion of the two fingers mechanically [45].

The most severe disadvantage is wearing out of the commutation brushes. Another problem is the limitation on the maximum transfer of armature current [53]. Moreover, electrical noise generated by the brushes causes interference to other delicate electronic circuits. In addition, with the presence of PM, assembly and material cost for the actuator become costly. Since PMs can only operate within a limited temperature range; actuator performance varies with temperature change. Furthermore, PMs are brittle and can be permanently de-magnetized beyond certain operating temperature. All of the above points hinder the robustness of the actuator.

2.1.3 Voice coil gripper

Voice coil has an incomplex construction. It is a linearized version of the rotary DC motor and very useful under limited stroke linear motion.

Unlike the DC motor; mechanical parts like screw threads can be eliminated for cost reduction when linear motion is required. Figure 2.3 shows a typical voice coil. It consists of PM, a moving coil and soft iron material to complete the magnetic circuit.

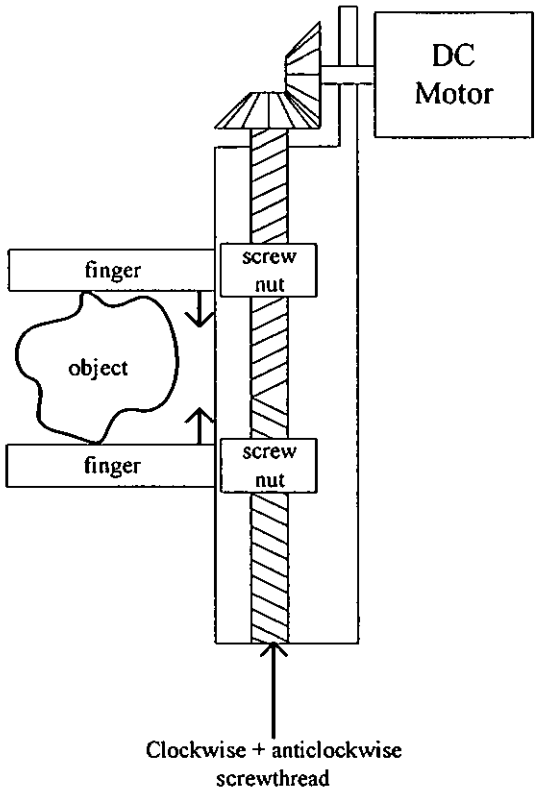

Figure 2.2: A DC gripper

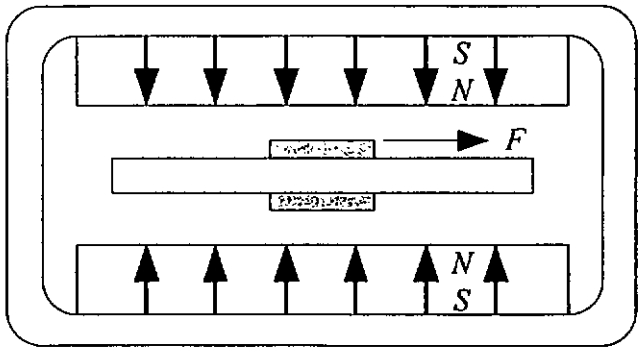

Figure 2.3: A voice coil

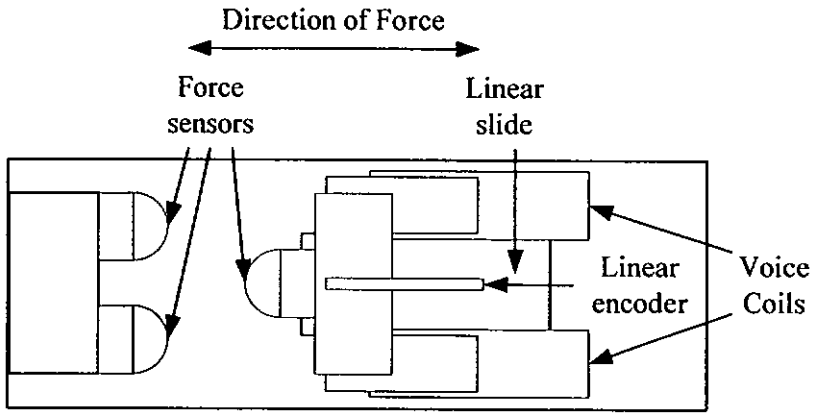

Figure 2.4: A voice coil gripper

Figure 2.4 shows a voice coil gripper which consists of a linear slide, a linear encoder, force sensors and voice coils [43]. The linear slide provides a guide-way for the actuator to move back and forth. It also maintains a constant air-gap between the magnet and the coil. Position and force control is accomplished by utilizing the feedback from the linear encoder and force sensor. Force generated is directly proportional to the applied winding current. Depending on the direction of the excitation current, force can be generated in both directions.

Apart from the disadvantages of the PM, the coil is a moving element, which is difficult to ensure the reliability of the actuator. The moving element can be the magnet but this would increase the moving mass and power consumption.

2.1.4 DC brushless motor gripper

Another popular choice of actuator for grippers is DC brushless motor. Unlike classical DC motor, the windings are wounded onto the stator while PMs are placed on the rotor. In this way, the DC brushless motor commutates without any brush. For this reason, it greatly improves its life and reliability. Figure 2.5 shows a brushless DC motor.

Without any electrical contact between the stator and rotor, electrical noise

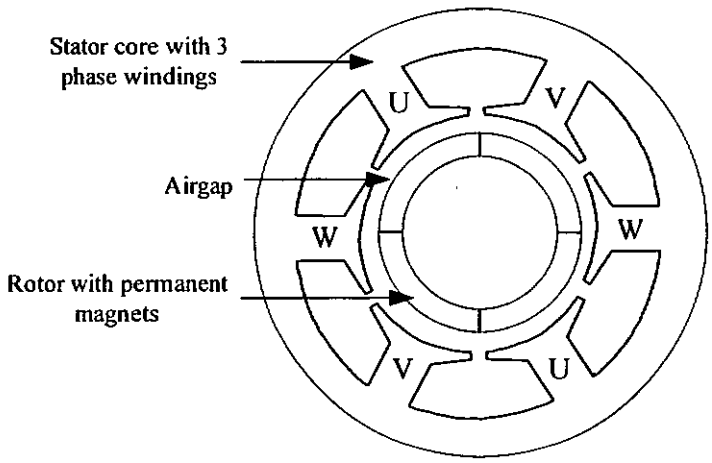

Figure 2.5: A typical 3 phase DC brushless motor

generated is much less. To increase its efficiency, windings are located on the stator where its heat can be removed more easily. Position sensors are mounted onto the rotor shaft for providing position information. Commutation is carried out by the controller [46].

With all of the above advantages, DC brushless motors can be commonly found in industrial robots and grippers. The multisensory articulated hand produced by German Aerospace Center (DLR) is an example [42].

The actuator is multi-phase, which increases the complexity of the driving circuit. It is also difficult to achieve high-precision accuracy due to the drifting and imbalance of the phase circuit elements like op-amps and current sensors. This generates torque ripple of the actuator and reduces its accuracy.

2.1.5 Thermal gripper

When a material is heated up, it expands in size. This type of gripper can be designed with different materials and shapes, using thermal technology. Thermal gripper shown in Figure 2.6 is a tailor-made gripper for micro-assembly and micro-operation applications [22]. It mainly consists of a thermal expansion element and a displacement transfer element. The thermal expansion element is etched onto the gripper. It is then

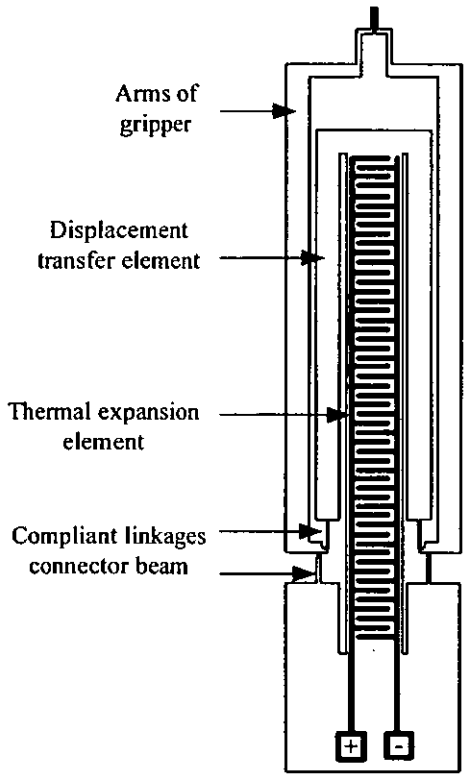

Figure 2.6: A thermal gripper

connected to a pair of electrode with low impedance. Therefore, only a low driving voltage is required to energize the thermal element.

In general, the thermal gripper suffers from very slow force response because its generated force is produced by material deformation. Besides, the opening distance of the gripper is limited to $120\mu m$. Furthermore, the external temperature of the working environment must be controlled strictly. Any alternation of this environment affects the gripping force. For these problems, thermal gripper is not widely used in industrial applications.

2.1.6 Piezoelectric gripper

Piezoelectric actuator is a favorable solution in recent years due to its compact size and high-precision. Piezoelectric materials change dimension when an electric field is

applied. A typical piezoelectric material is Plumbum Zirconate Titanate (PZT). Despite its response is extremely fast, this change is quite small, approximately equals to 0.1%.

In many ways, piezoelectric materials are similar to magnetic materials and both exhibit hysteresis. As the operating temperature approaches the Curie Temperature the actuators depole, the domains become unaligned, and the expansion with applied field is greatly reduced [73].

For small electric driving signal, the displacement of the piezoelectric actuator, δL_j can be estimated by:

$$\delta L_j = S_j L_o = d_{jj} E_i L_o \tag{2.3}$$

where S_j, L_o, d_{jj} and E_i represent mechanical strain in direction j, material thickness in field direction, piezoelectric deformation coefficient and electric field in direction i respectively [30]. Equation 2.3 shows that δL_j has a direct relationship with the electric field. Consequently, it would be necessary to provide high input voltage for a long travel distance.

Researchers reduce the input voltage to the piezoelectric actuator by adopting the multilayer approach [69]. A multilayer piezoactuator is a stack of PZT thin films electrically connected in parallel. The thinner the film, the lower the voltage required for maximum expansion of the multilayer stack. Generally, the lowest commonly found input voltage for piezoelectric actuator is $150V$ and over $300V$ for Ultra High Voltage (UHV) applications. With such high electric voltage input, Electro-magnetic Interference (EMI) noise can be easily generated and interfere with electric components and affect their operations.

Figure 2.7 shows a piezoelectric gripper [50]. The piezoelectric actuator is linked up with mechanical displacement transfer element to provide a gripping motion. However, the force deliverable is low and it is similar to the characteristic of the thermal gripper. It also suffers from small opening areas. It is only useful in miniature mechatronic systems.

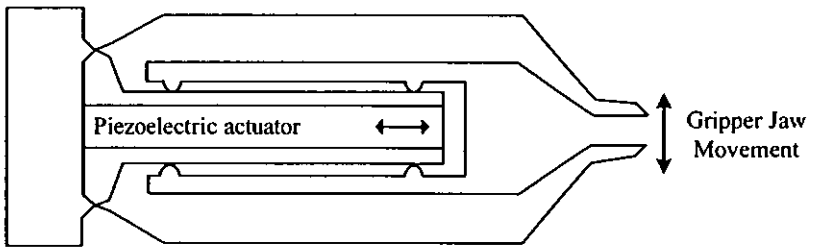

Figure 2.7: A piezoelectric gripper

2.1.7 Pneumatic gripper

Pneumatic systems are commonly found in high-force industrial applications. Pneumatic cylinders are relatively low-cost and fundamental. In pneumatic systems, force is produced by air pressure acting on the surface of a piston or valve. Compressed air is produced in a compressor and stored in a receiver. From here it is routed to valves which control the direction of fluid flow, flow control valves which control the amount of power produced by the cylinders which convert the potential energy of the compressed air into kinetic energy at the output.

Dexterous hand is a typical pneumatic gripper for industrial applications [6]. It is capable of producing high force up to $250N$. However, it is extremely difficult to control the pressure accurately in order to produce force at a high-precision level. Furthermore, it is very slow for the actuator to build up the force [5]. Unlike its electrical counterparts, its force response is much slower and it is in the order of seconds. Besides, operating under open-loop control, it is difficult to achieve high-precision especially when there is friction within the system. This might introduce tracking error between fingers. Therefore, pneumatic actuator is a poor choice for constructing a two-finger gripper for high-precision application.

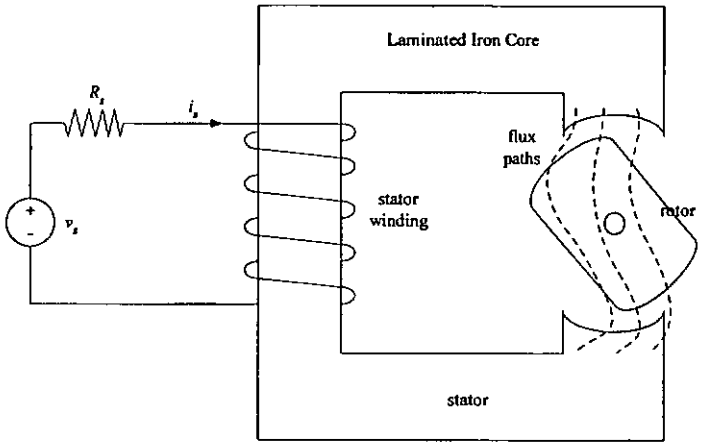

Figure 2.8: A rotating VR motor

2.2 The VR gripper

VR actuator has a basic and robust structure. Figure 2.8 shows a rotating VR motor [52]. The VR motor is a doubly-salient, singly-excited motor. This means that it has salient poles on both the rotor and the stator, but only the stator (in usual case) carries windings. Without any PM or cage winding, the rotor and the stator is built up from a stack of salient-pole laminations [39]. When a current passes through the stator winding, then magnetic flux links through the iron core and eventually the rotor will be attracted into the alignment with the pole pieces. On the other hand, if an external restraining torque is applied to the rotor and displaced from the this aligned position, the rotor will stay in an equilibrium position where the rotor reluctance torque balances out the external restraining torque.

The rotor and the stator are laminated to reduce the eddy current effect. With the absence of PM, it tends to have a lower inertia and the maximum permissible operating temperature is relatively higher. The stator windings do not have any phase-phase crossovers, and they are easy to fabricate. Therefore, the actuator has a very low manufacturing cost [48]. The operating principle of a VR actuator is similar to a solenoid; it has a higher inductance and slower current response than PM actuator. Furthermore, due to its salient pole structure, VR actuator inherits nonlinear properties; thus increases its control complexity. Due to the above reasons, the use of VR technology

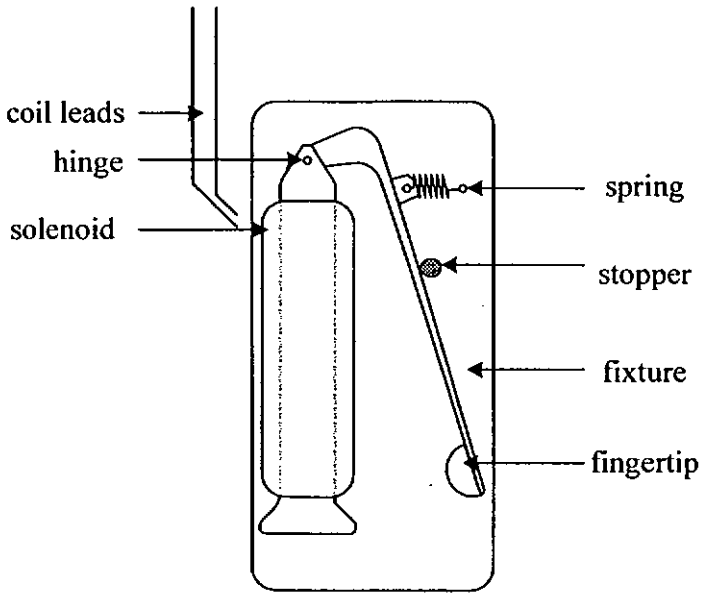

Figure 2.9: A VR finger

in high-precision gripper application is seldom explored.

Figure 2.9 shows a VR finger [16]. The VR finger is driven by a solenoid which behaves like a VR actuator. The moving element which is spring loaded for bi-directional motion, hinges on the upper end of the stationary part of the solenoid. When the solenoid is unenergized, the fingertip moves outwards.

2.3 Performance comparison

Table 2.1 shows the performance comparison of various actuators mentioned in this chapter. Data tabulated are the typical values of the actuators.

Due to the presence of PM, the cost of voice coil, DC and DC brushless motors are higher in terms of material and manufacturing costs. Besides, DC brushless motors, driving circuit is also expensive due to its multi-phase operations. Thermal and piezoelectric actuators have special structures; they require special techniques to construct and also high in costs. However, for thermal actuator, its force is generated

Actuators	Major cost	Response	Temperature range
DC motor	PM	$15ms$	-20–$65°C$
Voice coil	PM and linear guideways	$10ms$	-20–$155°C$
DC brushless motor	PM and drive	$15ms$	-20–$85°C$
Thermal actuator	Manufacturing process	$> 5s$	25–$125°C$
Piezoelectric actuator	Manufacturing process	$50ms$	20–$200°C$
Pneumatic actuator	Cylinder and valves	$> 1s$	-45–$180°C$
VR actuator	Iron core	$200ms$	-20–$300°C$

Table 2.1: Performance comparison of various actuators

with the deformation of materials would definitely be the slowest amongst all. For motors with PM, the operating temperature is limited by the demagnetization temperature of the PM. Besides, thermal actuator produces force with heat, the operating temperature has a great influence on its operation. Even in the case of piezoelectric actuators, its operating temperature is also limited by its Curie temperature at which the actuator depole. In terms of EMI interference, DC motor and piezoelectric actuator has the worst performance. DC motors can generate sparks easily by the commutation brushes. On the other hand, piezoelectric actuators require high input voltage which can influence with delicate electronic circuits.

VR actuator consists mainly of its iron core; it is simple in structure and easy-to-manufacture. Thus, it has a lower inertia and behaves as an electric actuator which is also fast in response. Without PM, VR actuator has a much wider operating temperature. Furthermore, it has a simple driving circuit and does not have severe EMI problem like piezoelectric actuators do.

2.4 Summary

This chapter states the requirements for an ideal gripper. Various types of actuators and their corresponding grippers are investigated. Their characteristics are studied and compared with each other. VR actuators are inherently robust, simple and low-cost when compared with electric motors and other actuators. VR actuators also enjoy faster

response and do not suffer from small openings and grippers actuated by thermal or piezoelectric technologies. VR actuators do not have a tight temperature limit and show good EMI properties. However, it is well-known of its nonlinear torque properties and has been a challenge to control it as a proportional device. With the advancement of Digital Signal Processor (DSP), implementation of novel control algorithm is now possible. By introducing a VR gripper, it can become an answer to all these problems.

Chapter 3

Analysis of VR grippers

This chapter describes the analysis of various arrangements of two-finger gripper using VR technology. Section 3.1 describes the basic principles of VR gripper. Section 3.2 analyzes the flux and torque production of various arrangement of two-finger VR gripper. In section 3.4, the principle of energy conversion analysis is introduced and an arrangement of two-finger VR gripper is chosen.

3.1 Principles of the VR gripper

Figure 3.1 shows a basic VR single-finger gripper. Its structure is similar to the VR actuator shown in Figure 2.8 with the exception of an extra finger attached to the rotor. When the rotor rotates, the finger swings along with the structure, producing a force acting onto the finger tip. The force F_f can be described as:

$$F_f = \frac{T_m}{l} \tag{3.1}$$

where T_m and l are the rotor torque and length of the finger respectively.

As mentioned in Chapter 2.2, when current is applied to the stator windings, the rotor has a tendency to reduce its reluctance by rotating itself to the fully aligned position. As a result of this rotation, torque is generated. Under such structure, only unidirectional

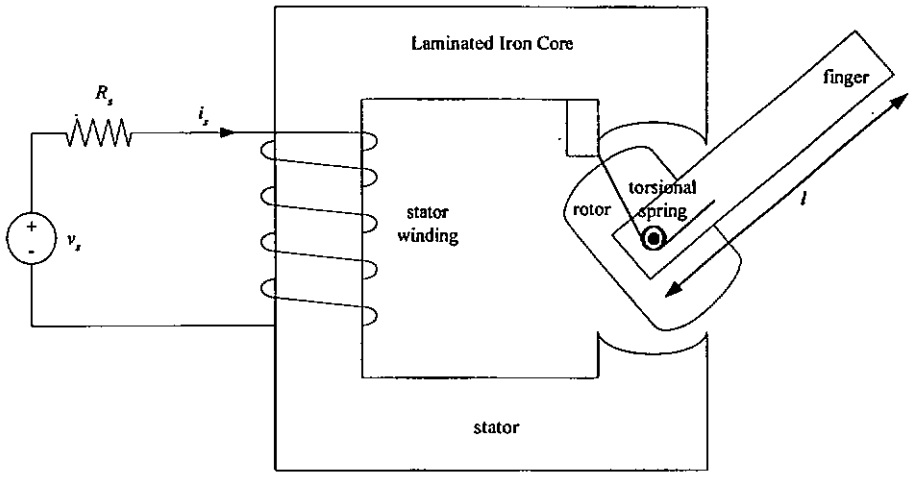

Figure 3.1: Basic single-finger VR gripper

torque can be generated. In order to produce torque in the other direction, extra poles and stator windings need to be added. This arrangement makes the structure more complicated and the overall cost more expensive. The simplest solution is to employ a torsional spring to produce the retracting force. The torsional spring has a linear relation against rotor positions, as shown in Equation 3.2 and 3.3 below [19].

$$K_{sp} = \frac{d^4 E}{64 D_{sp} N_{sp}} \tag{3.2}$$

$$T_{sp} = K_{sp}\theta \tag{3.3}$$

where K_{sp}, d, E, D_{sp}, N_{sp}, T_{sp} and θ represents the stiffness of the torsional spring, diameter of the spring wire, elastic modulus of the spring material, diameter of the spring, number of coils in the spring, applied torque onto the spring, and angular displacement of the spring respectively.

With the torsional spring installed, the rotor stays in an equilibrium positions where the reluctance torque balances out the counter-acting spring torque. By controlling the current applied into the stator windings, the required motion and rotor positions can then be achieved. Figure 3.1 becomes the basic building block of a VR finger gripper.

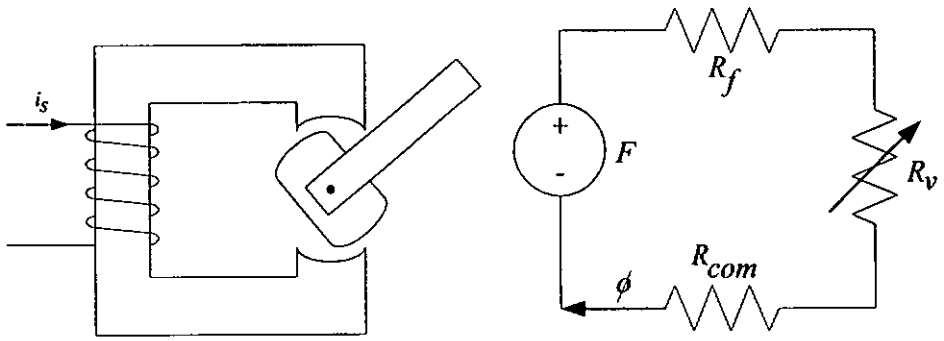

(a) mechanical structure (b) EQMC

Figure 3.2: A single-finger VR gripper

3.2 Equivalent magnetic circuit analysis

The magnetic structure of a single-finger gripper can be characterized by an Equivalent Magnetic Circuit (EQMC) [7]. By employing electric circuit elements to represent the features of the magnetic circuit, and by applying basic electric circuit theories, analyzing a magnetic system would be equivalent to analyzing an electric circuit. This becomes a major main advantage of transforming a magnetic system to its equivalent.

In an EQMC, stator winding, stator and rotor reluctances can be represented by Magneto-motive Force (MMF) source, F and fixed reluctance, R_f and variable reluctance, R_v as described in Equation 3.4. This is analogous to equations of electric circuits.

$$\begin{aligned} F &= Ni \\ &= (R_f + R_v + R_{com})\phi \\ &= (R_{vf} + R_{com})\phi \end{aligned} \tag{3.4}$$

where N is the number of turns in the stator windings, i is the stator current and $R_{vf} = R_v + R_f$.

For an idealized sinusoidal reluctance variation, the rotor reluctance, R can be approximated as [28]:

$$R = \frac{1}{2}(R_q + R_d) - \frac{1}{2}(R_q - R_d)cos2\theta \tag{3.5}$$

where R_d and R_q refer to the minimum and maximum value of reluctance, namely, direct-axis reluctance and quadrature-axis reluctance. R_d is directly in line with the axis of the stator poles.

Furthermore, the rotor torque T_m can be calculated by:

$$\begin{aligned} T_m &= -0.5\phi^2 \frac{dR(\theta)}{d\theta} \\ &= -0.5\phi^2(R_q - R_d)sin2\theta \end{aligned} \tag{3.6}$$

As described in Equations 3.5 and 3.6, the rotor torque of the two-finger VR gripper has a square relationship with flux, ϕ.

3.2.1 Two-finger VR gripper with separate magnetic circuits

To implement a two-finger VR gripper, the simplest method is to allow each finger being driven by an individual actuator. Figure 3.3(a) and 3.3(b) shows the basic mechanical structure and the EQMC of a two-finger VR gripper driven by independent VR actuators.

In this configuration, the stator windings, rotor and stator core are represented by two MMF sources, F_{left} and F_{right}, two variable reluctances, R_a, R_d and two fixed reluctances R_b, R_c.

The left and right magnetic circuits link through path ABC and DEG without any mutual flux coupling. Due to the symmetrical structure of the actuator, the left and right excitation currents during gripping motion can be considered equal, and the left and right variable and fixed reluctances on the two magnetic circuits can also be assumed equal. Equations 3.7-3.9 describe these simplifications mathematically.

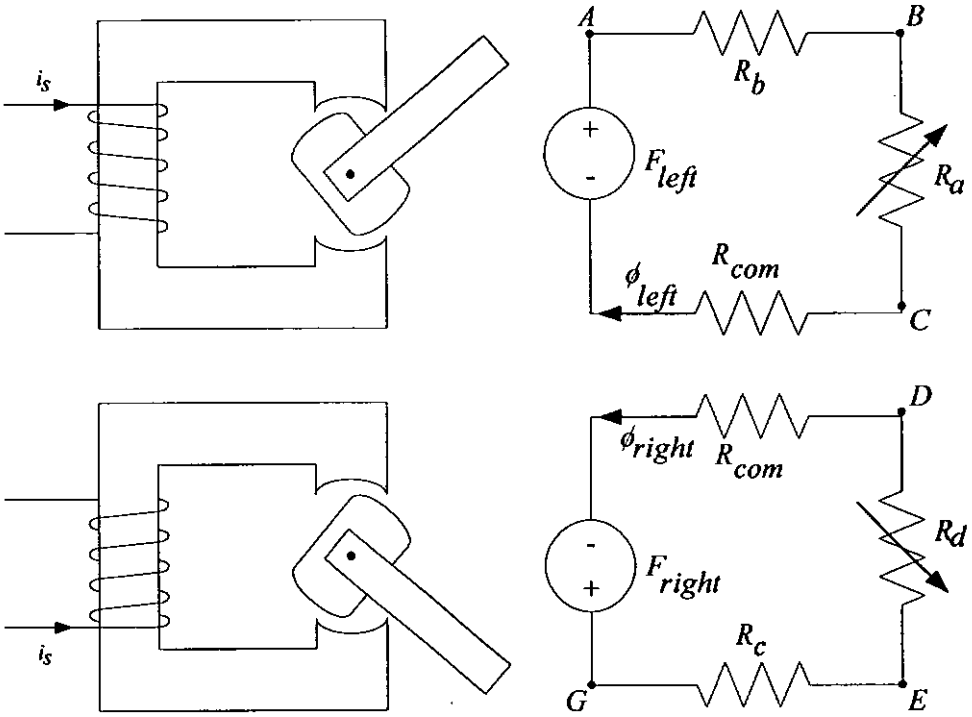

(a) mechanical structure (b) EQMC

Figure 3.3: A two-finger VR gripper driven by two separate magnetic circuits

$$F = F_{left} = F_{right} \tag{3.7}$$

$$R_f = R_b = R_c \tag{3.8}$$

$$R_v = R_a = R_d \tag{3.9}$$

where F, R_f and R_v represent the MMF source, fixed reluctance and variable reluctance respectively.

Then the flux passes through the rotor, ϕ_{sep}, can be described as:

$$\phi_{sep} = \phi_{left} = \phi_{right} \tag{3.10}$$

$$= \frac{F}{R_{vf} + R_{com}} \tag{3.11}$$

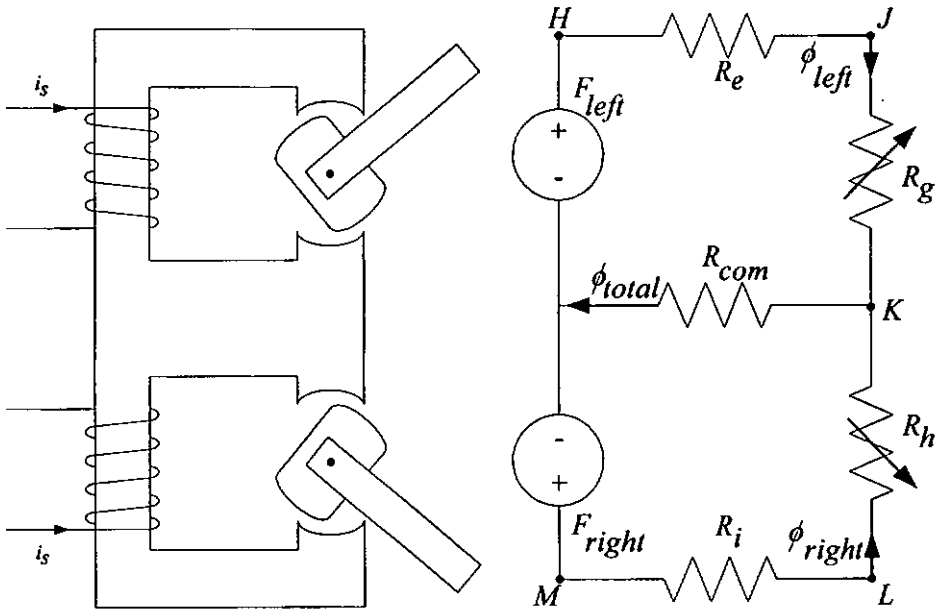

(a) mechanical structure (b) EQMC

Figure 3.4: A two-finger VR gripper driven by two combined magnetic circuits

3.2.2 Two-finger VR gripper with combined magnetic circuit structure

Another alternative is to combine the two magnetic circuits together. This allows the two-finger VR gripper to be more compact. The major difference is the appearance of mutual flux on the magnetic circuit.

Figure 3.4(a) and 3.4(b) shows the basic mechanical structure and the EQMC of a two-finger VR gripper driven by two combined magnetic circuits. In the same manner, the stator windings, rotor and E-core can be represented by MMF sources, F_{left} and F_{right}, variable reluctance, R_g and R_h, and fixed reluctance, R_e and R_i. Under this arrangement, it can be considered as two individual rotating VR motors combined together. Besides, return paths of both magnetic circuits are connected together at node K. Similarly, the symmetrical structure has equivalent force and reluctance on the left and right side. Therefore,

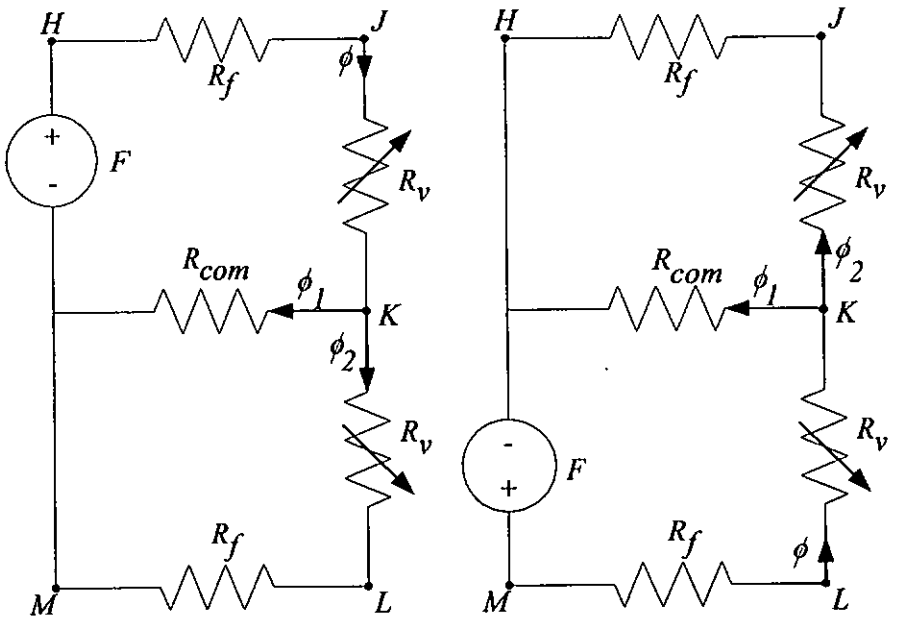

(a) Consider left MMF source only (b) Consider right MMF source only

Figure 3.5: Superposition of magnetic circuit

$$F = F_{left} = F_{right} \tag{3.12}$$

$$R_f = R_e = R_i \tag{3.13}$$

$$R_v = R_g = R_h \tag{3.14}$$

By linear superposition, considering the left MMF source only, the EQMC can be simplified as in Figure 3.5(a). As a result, the system magnetic equations can be written as:

$$\begin{aligned} \phi &= \phi_1 + \phi_2 \\ &= \frac{F}{R_{vf} + (R_{com} \parallel R_{vf})} \end{aligned} \tag{3.15}$$

Since $R_{com} \ll R_{vf}$, then it can be assumed that,

$$\phi \simeq \frac{F}{R_{vf} + R_{com}} \tag{3.16}$$

and

$$\phi_2 = \phi \frac{R_{com}}{R_{com} + R_{vf}} \tag{3.17}$$

So the flux passes through the rotor,

$$\begin{aligned} \phi_{comb} &= \phi - \phi_2 \\ &= \frac{F}{R_{com} + R_{vf}} - \phi \frac{R_{com}}{R_{com} + R_{vf}} \\ &= \frac{F - \phi R_{com}}{R_{com} + R_{vf}} \\ &< \phi_{sep} \end{aligned} \tag{3.18}$$

According to Equation 3.6, the arrangement shown in Figure 3.4(a) should produce less torque than arrangement shown in Figure 3.3(a).

3.3 Limitation of the equivalent magnetic circuit analysis

However, there are some major assumptions made for adopting such a model:

1. Hysteresis loops of the materials are narrow and they have little effect on the overall magnetic circuit.
2. Magnetization curve of such material may be approximately represented by a straight line through the origin where μ_r is a constant.
3. Reluctance variation is approximately sinusoidal.

To put it simply, if the magnetic characteristic of the gripper is linear or pseudo-linear, the magnetic system may be represented by a linear EQMC, and the techniques of linear electric circuit analysis may be used [37]. For VR actuators, it is operated under saturated region for most of the time to maximize its efficiency, thus the proposed linear method of analyzing magnetic circuit may produce substantial error.

So the above mentioned analysis is only valid inside the linear region. Nevertheless, once the motor enters saturation region, analyzing with EQMC will produce large error.

3.4 Energy conversion analysis of VR gripper

When analyzing torque production of a VR actuator in both the linear and saturated region, the concept of energy conversion is usually used. Magnetization curves shown in Figure 3.6(a) and Figure 3.6(b) are curves of flux-linkage λ versus current i, at a particular rotor position for both linear and saturated magnetic devices [38]. From the diagram, the stored magnetic energy W_f and the co-energy W_c can be expressed as:

$$W_f = \int_0^{\lambda} i(\lambda, \theta) d\lambda \tag{3.19}$$

$$W_c = \int_0^{i} \lambda(i, \theta) di \tag{3.20}$$

Notice that, these equations are applicable to both linear and saturated devices. In this analysis, the magnetic characteristics of the VR gripper, λ is expressed in terms of its current and its rotor angle. For cases shown in Figures 3.2-3.4, each has a unique flux-linkage profile against current and rotor angle depending on the magnetic system.

The instantaneous torque production, T_m, of the VR actuator is given by:

$$T_m = \left[\frac{\partial W_c}{\partial \theta}\right]_{i=const} \tag{3.21}$$

From Equation 3.21, it can be clearly seen that the shaded area of co-energy determines torque production. For VR motor, it becomes more efficient once it enters the saturation region. Hence, it is a common practice to increase the stator current for a higher torque production.

3.5 Comparisons between equivalent magnetic circuit analysis versus energy conversion analysis

Table 3.1 tabulates the comparison between EQMC and energy conversion analysis. For EQMC analysis, the computation is simple and linear electric circuit theories can be used

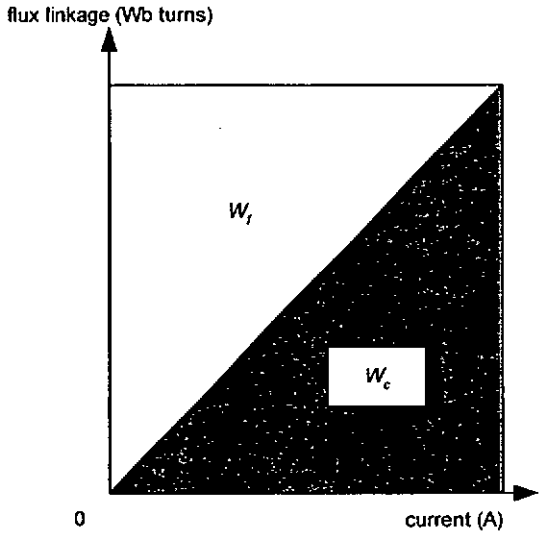

(a) linear device

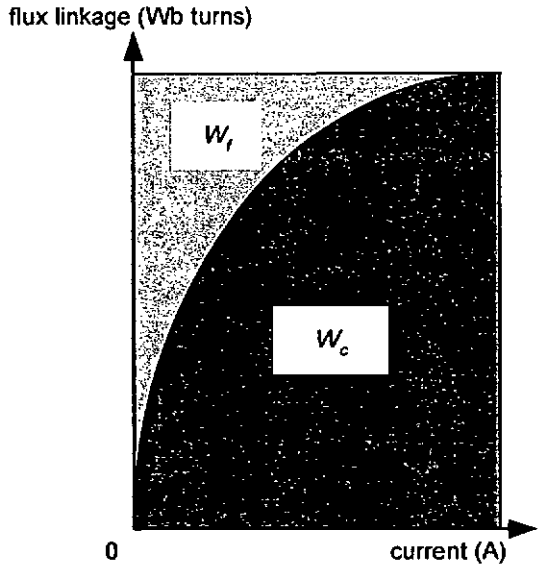

(b) saturated device

Figure 3.6: Magnetization curves of linear and saturated magnetic devices at a particular rotor angle

Methods	Advantages	Assumptions
EQMC	Simple	Linear devices
	Linear circuit theories are applicable	Sinusoidal reluctance variations
Energy conversion	Complex	N/A

Table 3.1: Performance comparison of magnetic analysis

while solving complex multi-phase magnetic systems. However, it only limits itself to linear magnetic devices. For torque production, it also assumes an approximate sinusoidal reluctance variation. On the other hand, energy conversion analysis is relatively complex and valid for both linear and saturated devices. It calculates the torque production through the system magnetic characteristics which is in terms of co-energy.

As shown in Table 3.1, it is clear that EQMC is favorable for magnetic actuator operating in the linear region. For those operating within the nonlinear region, energy conversion analysis is necessary. By not assuming any idealized reluctance variation, energy conversion analysis is valid in both linear and saturated regions. Therefore, it is suitable for analysing or modeling a two-finger VR gripper.

Under the separate magnetic circuit arrangement shown in Figure 3.3, it produces more torque than combined magnetic circuit arrangement within linear region as shown in Figure 3.4. This is due to the fact that for combined magnetic circuit arrangement, both magnetic circuits share the same return paths. By linking the two return paths together, the magnetic circuit can be saturated more easily with two MMF sources. In other words, the two finger VR gripper using the structure shown in Figure 3.4, has a higher flux-linkage value with the same current level. Moreover, by combining the two fingers into a single magnetic housing, this has made the finger alignment process much simpler and the overall size much smaller the individual single finger actuator.

This project aims at designing a two-finger VR gripper which produces more torque than an ordinary VR actuator. For VR actuators, it is generally operated under the saturation region, so the combined magnetic circuit arrangement is more favorable.

3.6 Summary

In this chapter, the EQMC and energy conversion analysis of various types of VR finger gripper are introduced. It has been mentioned that the energy conversion analysis is a more appropriate method when analyzing the two-finger VR gripper. It is because VR actuators usually operate under saturation region and its permeability cannot be represented by a constant. Various types of two-finger VR gripper are introduced and the combined magnetic circuit should provide a better performance than the separate magnetic circuit arrangement. Characterisation of the two-finger VR gripper will be discussed in the next chapter.

Chapter 4

Construction and performance of two-finger VR gripper

The main objective of this chapter is to describe the design and fabrication of a novel two-finger VR gripper suitable for position and force control applications. In this chapter, details of the construction and measurements of the two-finger VR gripper are described. In order to evaluate the performance and to obtain the characteristics of the gripper, an extensive magnetic characterization exercise was conducted. Various flux-linkage measurement methods were reviewed and characterization experiments of the actuator were carried out. The results show that the proposed actuator exhibits as VR motor characteristics and it becomes more efficient through the use of mutual coupling.

Section 4.1 gives the details of the construction of the two-finger VR gripper. Details of the controller system employed for this research project is given in section 4.2. Then section 4.3 derives the basic control model of the two-finger VR gripper. Equations representing electrical, mechanical and magnetic characteristics are derived. Section 4.4 and section 4.5 review and compare the different flux-linkage measurement methods. Section 4.6 and section 4.7 conduct the flux-linkage and direct torque measurement for the two-finger VR gripper. Then sections 4.8 and 4.9 investigate the losses of the two-finger VR gripper, which include leakage flux-linkage, eddy current and hysteresis losses. Finally, the torsional spring stiffness measurement is discussed in section 4.10.

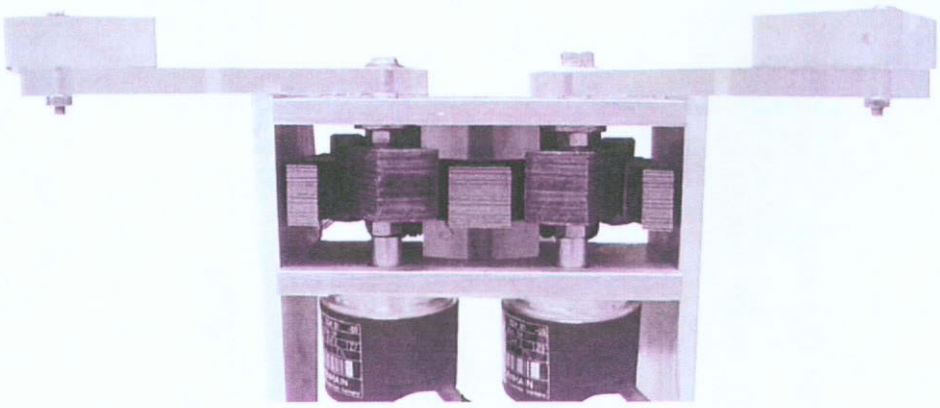

Figure 4.1: The two-finger VR gripper used in this research project

4.1 Construction of the project two-finger VR gripper

In order to further explore the proposed design mentioned previously, a prototype two-finger VR gripper with combined magnetic circuit is developed. Figure 4.1 shows the front view of the two-finger VR gripper.

The two-finger VR gripper can be classified as a precision type which places its emphasis on dexterity and sensitivity [20]. The stator is made from laminated DT42 E-core steel which links the two magnetic circuits together. Both the rotors and stators are laminated to reduce eddy current effects. The laminated mild steel plate is shown in Figure 4.2.

Figure 4.3(a) and 4.3(b) shows the rotors and stator windings of the two-finger VR gripper respectively. The two-finger VR gripper has two rotating axes. Each of the two rotors are mounted onto two individual shafts, which are supported by a pair of bearings, with the rotating axes normal to the magnetic plates. The moving elements may rotate freely between the poles of the stator. For each rotating axis, there is an incremental encoder with a resolution of 0.09^o, connected onto the rotor.

Each of the two rotors of the two-finger VR gripper has a detachable finger attached to it. The two fingers of the gripper are $90mm$ long and are preloaded with torsional springs. This arrangement allows bi-directional movements from a single-direction coil

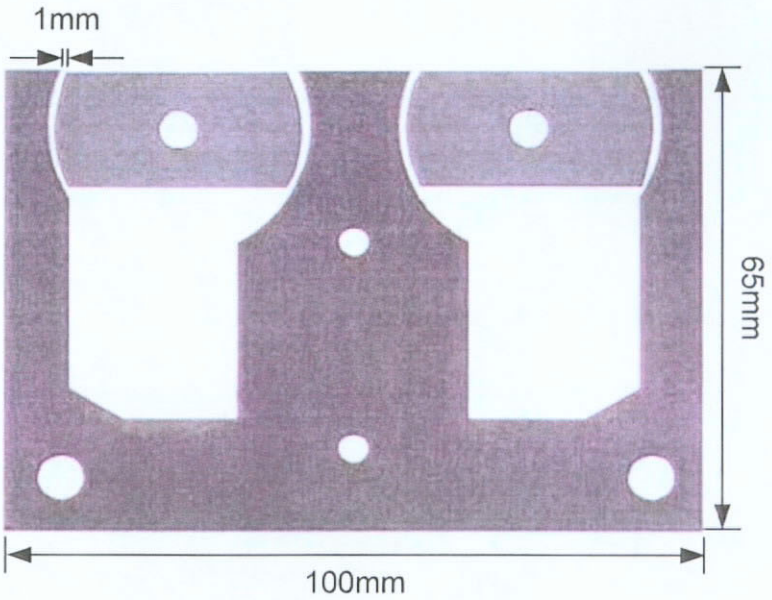

Figure 4.2: Stator and rotor steel plates of the two-finger VR gripper

excitation in a cost-effective manner. There are also two individual stator windings wound around the stator core with 400 turns each. The use of detachable finger allows for wear and interchangeability. These fingers which are shown in Figure 4.4 can also be redesigned to adapt to any kind of gripping object.

Figure 4.5 shows the basic operating principle of the two-finger VR gripper constructed for this research project. When currents are applied to the stator windings, the rotors will rotate away from their initial rest positions with a tendency to reduce their reluctance by alignment torque. The rotor will stop when alignment torques comes into equilibrium with restraining torques provided by the torsional springs. When the fingers rotate by 65^o, the fingertips will be fully closed.

The overall construction is extremely simple and robust, and it is very similar to rotary solenoids, used in on-off mechanical actuation. Combining the two fingers into a single magnetic housing has made the finger alignment process much simpler and the overall size much smaller. Details of the two-finger VR gripper is tabulated in Table 4.1

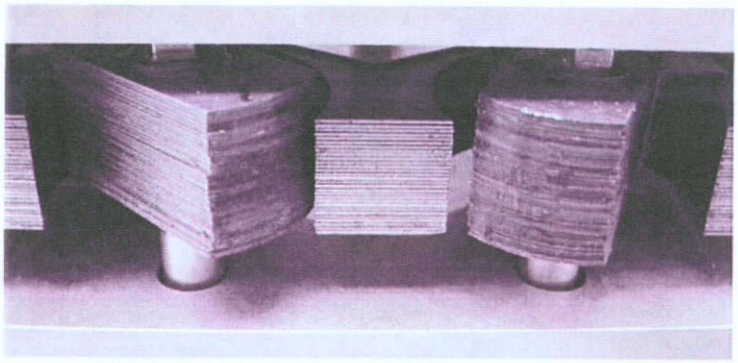

(a) Rotors

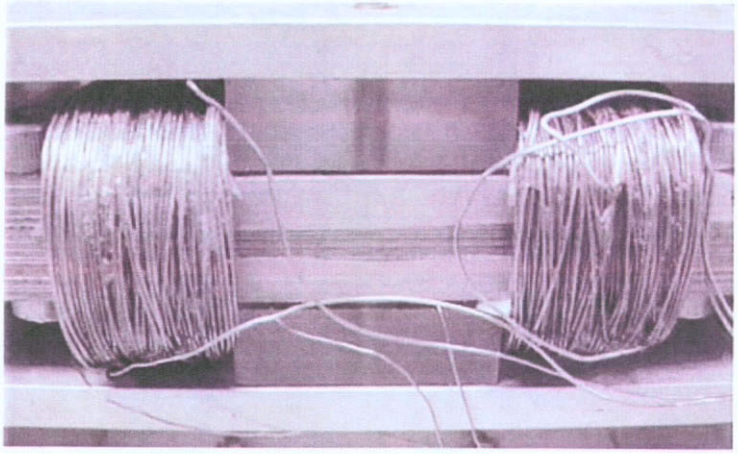

(b) Stator windings

Figure 4.3: The proposed two-finger VR gripper

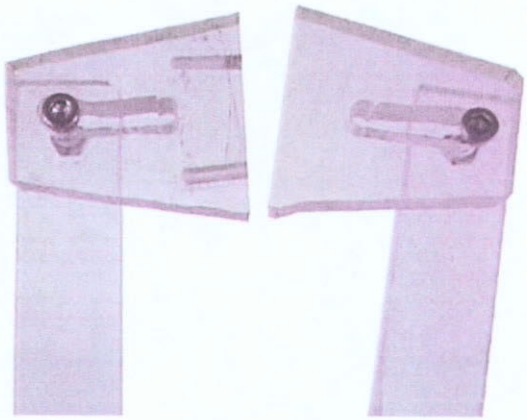

Figure 4.4: Detachable fingers of the two-finger VR gripper

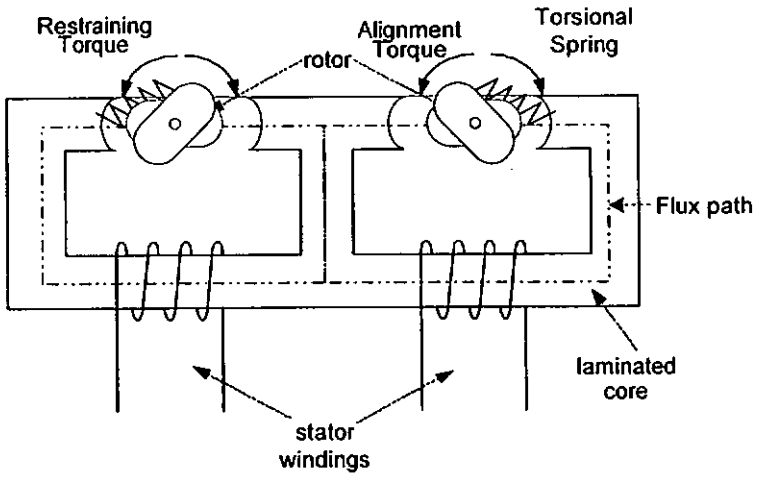

Figure 4.5: Basic operating principle of the two-finger VR gripper

	Notation	Values	
Stroke angle	θ	65	degrees
Operating voltage	V	60	VDC
Operating frequency	f	3	Hz
Maximum instantaneous current	$I_{inst.}$	7	A
Maximum continuous current	$I_{cont.}$	4	A
Resistance of stator winding	R_m	4	Ω
No. of turns in stator winding	N	400	turns
Rotor inertia	J_m	0.015	kgm^2
Viscous constant	K_v	0.0075	$gmrad^{-1}s$

Table 4.1: Two-finger VR gripper profile

4.2 Controller system

Figure 4.6 shows the dSPACE Kit 1104 which is used as the data acquisition and the system controller in this project. The main components of the dSPACE Kit 1104 which are applicable to this project are,

- Single-Board-Hardware DS1104 Controller Board
- Implementation Software programming from *SIMULINK* with Real-Time Interface (RTI)
- Experiment Software *ControlDesk Standard*

The DS1104 controller board is a one PCI-slot half size board which has an on-board 250MHz MPC8240, PowerPC 603e core floating-point processor for real-time computation. It interfaces with the Personal Computer (PC) through the Peripheral Component Interconnect (PCI) bus. The interface circuit includes two 24-bit digital incremental encoder interfaces, four 16-bit Analog-to-digital Converter (ADC), four 12-bit ADC, eight 16-bit Digital-to-analog Converter (DAC) and seven Pulse Width Modulation (PWM) channels.

In connecting with *MATLAB* RTI and *SIMULINK*, graphical programs or even control block diagrams can be converted into real-time control C-code with a *SIMULINK* diagram. Assembly codes can be compiled and downloaded to the DSP running in real-time. On the other hand, the experiment software *ControlDesk Standard* interfaces with the user, accepting their inputs graphically, displaying the current status of the controlled system and logging of necessary data.

In this project, the two incremental encoder interfaces receive the encoder signals from the two-finger VR gripper, while the ADC channels receive and convert current or other measurements into digital signals. For control experiments, the DS1104 controller board calculates the control algorithm on the basis of the measured values and determines the corresponding PWM values.

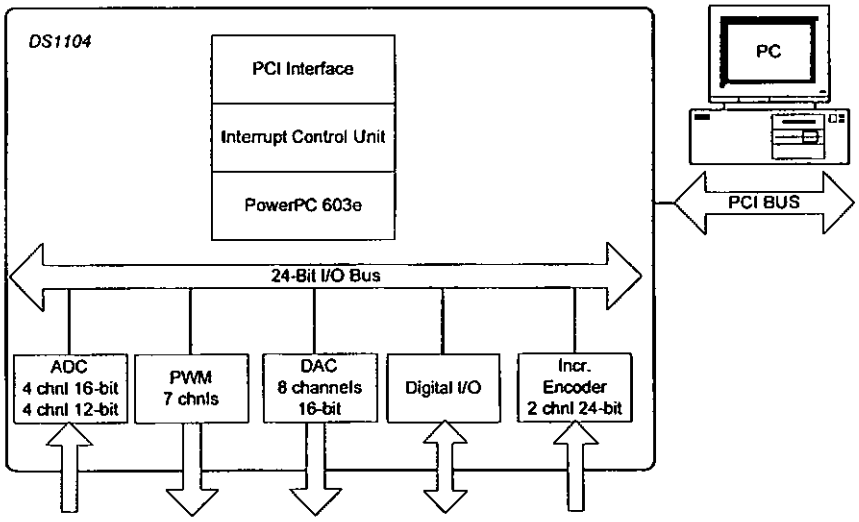

Figure 4.6: The Dspace controller system used for the research project [21]

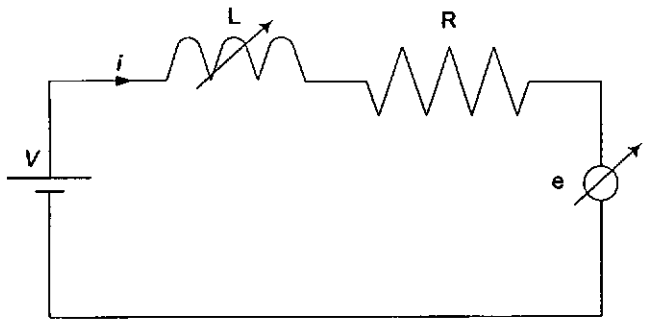

Figure 4.7: General VR motor electrical representation

4.3 Basic mathematical model

The electrical characteristics of the two-finger VR gripper can be described as a resistive and inductive structure which is shown in Figure 4.7.

Its voltage equation can be expressed as:

$$V = R_m i + \frac{d\lambda(\theta, i)}{dt} \tag{4.1}$$

$$\lambda = \lambda_s + \lambda_m + \lambda_l \tag{4.2}$$

where V, R_m, i, θ, λ, λ_s, λ_m and λ_l are terminal voltage, coil resistance, current, angular

position of the rotor, total flux-linkage, self flux-linkage, mutual flux-linkage and leakage flux-linkage respectively [28]. Therefore, the voltage equation can be expanded as:

$$V = R_m i + \frac{\partial \lambda(\theta, i)}{\partial i} \cdot \frac{di}{dt} + \frac{\partial \lambda(\theta, i)}{\partial \theta} \cdot \frac{d\theta}{dt} \tag{4.3}$$

where

$$e_{bemf}(i, \theta, \dot{\theta}) = \frac{\partial \lambda(\theta, i)}{\partial \theta} \cdot \frac{d\theta}{dt} \tag{4.4}$$

For low speed operations, back EMF, $e_{bemf}(i, \theta, \omega)$ can be omitted and Equation 4.3 can be simplified to:

$$V = R_m i + L(\theta, i)\frac{di}{dt} \tag{4.5}$$

Furthermore, mechanical dynamics of the two-finger VR gripper can be determined by equating all the torque contributing elements as below:

$$T_m = J_m \ddot{\theta} + K_v \dot{\theta} + K_{sp}\theta + T_L \tag{4.6}$$

where T_m is the torque required, J_m is the total rotor and load inertia, K_{sp} is the spring constant, K_v is the damping constant and T_L is the load torque.

As described in the previous chapter flux-linkage has a nonlinear relation with current and position. In order to control the motion and force of the VR gripper of high-precision, an accurate flux-linkage model needs to be obtained. Otherwise, the behavior of the two-finger VR gripper would be difficult to simulate. Hence, all the nonlinear elements of the actuator need to be embedded into simulation model and the corresponding real-time controller.

4.4 Review of flux-linkage measurement methods

The flux-linkage characteristics of VR actuator changes with different rotor positions. Due to its doubly salient construction, the actuator can easily be saturated. When the rotor poles align with the stator pole, i.e. at aligned position, the reluctance for the flux path is at its minimum and the actuators magnetic circuit is highly saturated. When the stator pole moves away from the rotor pole, i.e. at unaligned position, the reluctance is higher and the actuator does not saturate as much as it is at the aligned position.

The study of flux-linkage characteristics can be conducted by Finite-element Method (FEM). FEM analysis can be useful in optimizing the actuator design. However, the accuracy of the result depends on the skill of the user in choosing the mesh elements. Besides the method is computational complex. Generally, it is easier for to obtain the magnetic characteristics of the actuator through measurement.

Due to the nonlinear relationship of VR actuators with current and rotor positions, various flux-linkage measurement methods have been proposed [47, 61, 14]. However, only two methods are commonly in use and these two methods will be reviewed in this section.

4.4.1 Step measurement

The first method is to apply a step voltage across the stator winding. By recording the current and voltage levels, flux-linkage at a certain position can be evaluated offline easily. This method is one of the most favorable method for VR motor researchers [47, 61, 14, 27].

Rearranging Equation 4.1, flux-linkage can be obtained through Equation 4.7:

$$\lambda(\theta, i) = \int (V - R_m i) dt \tag{4.7}$$

where θ, V, R_m, i represent the rotor position, input voltage across the stator winding, resistance of the stator winding and stator winding current respectively.

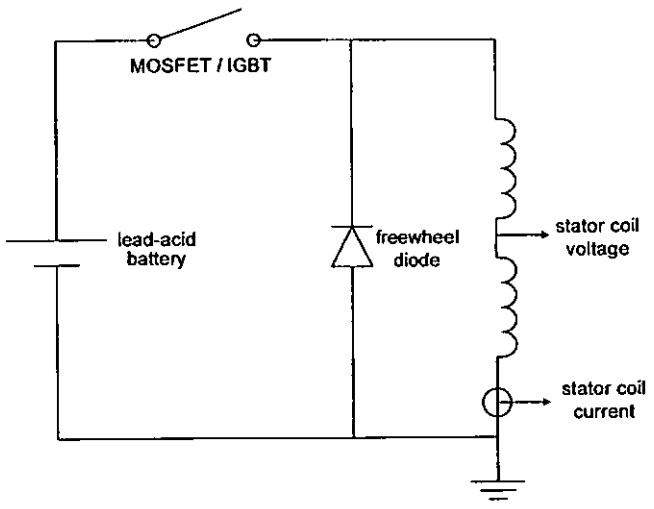

Figure 4.8: Flux-linkage measurement circuit

Figure 4.8 shows the circuit diagram for the flux-linkage measurement setup. For this method, a step voltage is injected into a stator winding with the rotor being locked into a fixed position. The supplied voltage provides a steady-state stator winding current typically 120% of the full load current. Waveforms of the voltage and current are recorded. By assuming winding resistance being constant, the flux-linkage at a certain rotor position versus different current level can be determined with an offline integration of Equation 4.7. And the entire experiment is repeated with the rotor rotated to a set of equally spaced position, ranging from the fully aligned to fully unaligned positions [47]. For the case of two-finger VR gripper both windings are connected in series to ensure the current flows through both windings are equal. Besides, both rotors have to be locked at the same rotor positions.

This method is further improved by employing a lead-acid battery as the voltage source [65]. This can completely eliminate current ripples due to RLC oscillations. Instead of a classical mechanical switch which would introduce unnecessary mechanical bouncing and voltage disturbance, a high-speed semi-conductor switch should be used. This arrangement can offer fast switching response and vibration free voltage transient.

The main advantage of this experiment is its simplicity. As the step input voltage is applied across the stator windings, the stator current rises, therefore, instantaneous flux-linkage versus different current can be evaluated without repetition measurement. Besides, it does not require any fitting of extra sensing coils onto the stator.

However, the main difficulty with this method is the choice of a suitable R_m. An inaccurate R_m introduces drifting into the flux-linkage integration. In practical situation, the value of R_m used in the digital integration is adjusted arbitrarily until the zero sections of the flux-linkage waveform are truly horizontal. In addition, the injected step input voltage consists of numerous high frequency components, and therefore this introduces extra eddy current into the measurement results.

Figure 4.9 suggests the flux-linkage profile of the two-finger VR gripper measured with step flux profile. The result is similar to the measurement of a VR actuator using step measurement method.

But, referring to Equations 4.1 and 4.2, it can be clearly noticed that the flux-linkage obtained with this method has the self, mutual and leakage flux-linkage all summed up as a single unit. Generally, mutual and leakage flux-linkages are assumed negligible for VR motors. However, for the mutually coupled two-finger VR gripper, the step measurement method is not applicable. As a result, a more accurate method is preferred.

4.4.2 AC excitation method

Another commonly employed method is the use of AC excitation method [27]. The proposed method is based on the digital integration of the EMF induced by flux variations in a search coil mounted on the stator poles. When a flux, ϕ passes through a search coil with N_s turns, an EMF, $e_{srh}(t)$, would be induced and thus flux can be expressed as:

$$\phi(t) = -\frac{1}{N_s}\int e_{srh}(t)dt \tag{4.8}$$

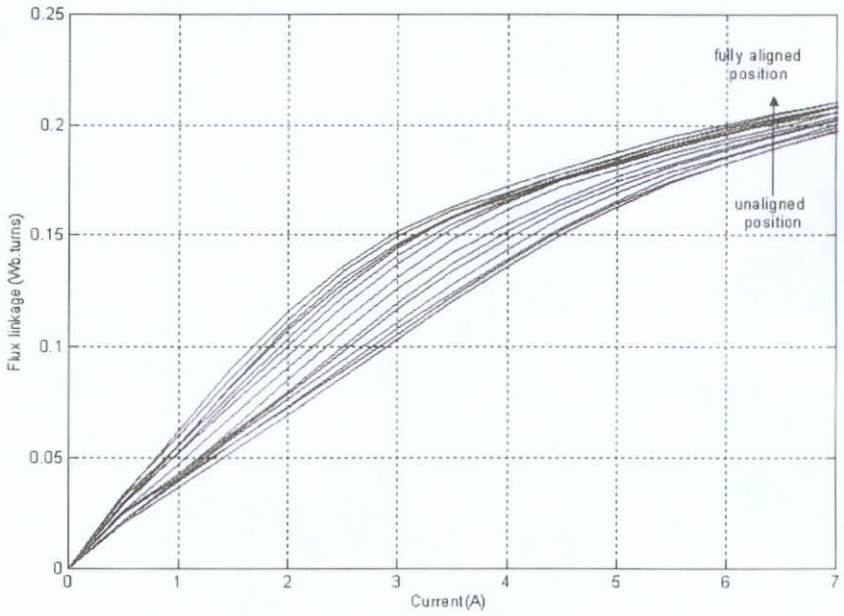

Figure 4.9: Flux-linkage profile at different rotor angles with step measurement method

In this measurement, rotor is locked at a particular rotor angle and the excitation winding is supplied by a sinusoidal current. Under such condition, the actuator behaves as any magnetic circuit under cyclical magnetization.

Since flux calculation is an integration process, a slight DC offset in the integration process will produce a significant shift in the integrated value over a prolonged period. To eliminate this error, a compensation value of δe_{srh} is added to the integration process, as:

$$\delta e_{srh} = \frac{\int_0^T e_{srh}(t) - e_{srh}(0)}{N_{samples}} \tag{4.9}$$

where T is the period of the input AC current, $e_{srh}(0)$ is the initial measured voltage across the search coil and $N_{samples}$ is the number of samples during one period T. Since the input current and voltage across the stator winding are symmetrical with zero mean values, the flux output can also be assumed to be symmetrical with zero mean value. In other words, the flux signal, $\phi(t)$ should have the same maximum and minimum values. As a result, the initial flux, $\phi(0)$, having the effect of shifting $\phi(t)$ to a symmetrical position, can be obtained as:

$$\phi(0) = \frac{\phi(2) - \phi(1)}{2} \tag{4.10}$$

Combining Equations 4.9 and 4.10, 4.8 can be rearranged as suggested in [15].

$$\phi(t) = -\frac{1}{N_s} \int_0^T [e_{srh}(t) + \delta e_{srh}]dt + \phi(0) \tag{4.11}$$

By joining the vertices of the first quadrant produced by various current levels, the flux-linkage profile of the two-finger VR gripper can be constructed [67]. As mentioned before, the experiment requires the use of search coils in the machine. For standard VR motors, it is difficult to wound extra search coils onto the stator because the motor is enclosed. However, for the case of two-finger VR gripper, this is feasible because the fitting of search coils can be installed at the prototype development stage. Besides, if additional search coils are placed at other poles, mutual and leakage flux-linkage can also be measured. In this manner, the accuracy of the experiment can be improved substantially. Unlike, the step measurement method, variations in electrical parameters of the VR motors have no impact on the measurement accuracy, because readings are directly measured from the search coils.

Furthermore, it is verified that the flux-linkage result do not change for a specified maximum value of the excitation current in a wide range of excitation frequency values [27]. It can be expected that as the operating frequency increases, there is a reduction in flux-linkage values. This is mainly due to the demagnetization effect of eddy currents. However, since eddy currents are negligible in two-finger VR gripper with the presence of laminated iron core. As a result, the reduction in flux-linkage value in change of frequency can be neglected.

Moreover, even though the input winding excitation is not purely sinusoidal, the measurement method can still be considered valid [26].

	Step measurement	AC excitation
Feasible for two-finger VR gripper	✓	✓
Number of measurements	N_p[a]	$N_p \times N_c$[b]
Leakage flux-linkage measurement	×	✓
Hysteresis measurement	×	✓
Eddy current measurement	×	✓
Measurement accuracy	Fail to determine λ_s, λ_m and λ_l alone	λ_s, λ_m and λ_l are determined separately

[a] N_p refers to no. of flux-linkage measurements between intermediate positions
[b] N_c refers to no. of flux-linkage measurements between intermediate current levels

Table 4.2: Comparison of flux-linkage measurement methods

4.5 Comparison of flux-linkage measurement methods

From Table 4.2, it is clear shown that AC excitation method is the most suitable for characterizing the magnetic properties of the two-finger VR gripper. It can be applied to the two-finger VR gripper with good measurement accuracy. The AC excitation method has the advantages of independence of electrical characteristics and mutual and leakage flux-linkage are separated from the measurement. Moreover, hysteresis effect and eddy current effect can be obtained.

The major disadvantage is the tedious repetition of measurement for different values of excitation currents for all rotor positions at which measurements are undertaken for this method. Since this is a one-off measurement task, the benefits of measurement accuracy outweighs the inconvenience of repetitive measurements. Extra measurement procedures are still worthwhile.

4.6 Flux-linkage measurement

4.6.1 Assumptions

Before conducting the actual flux-linkage measurement, basic operation of the two-finger VR gripper must be understood, otherwise the range of experimental measurements would

be very large. Since the two-finger VR gripper is designed for gripping purposes, certain reasonable assumptions can be made:

1. The gripping object is symmetrical and the grasp of the object is at its centre of mass so that no moment would tend to rotate the centre of mass.

2. The two-finger VR gripper is symmetrical in size and both fingers are always at the same rotor positions. As a result, both stator current would be equal at all times, and thus both rotors producing same amount of torque.

3. With the same flux level, no mutual flux-linkage can be found because the common path shares the same potential.

With the above mentioned assumptions, during the experiment, both stator windings are connected in series which guarantees both windings are excited with same current level simultaneously. Moreover, both rotors have to be locked at the same rotor positions.

4.6.2 Implementation

A $50Hz$ variable current can be produced easily with an isolated autotransformer connected to a $240VAC$ power source. A high speed semi-conductor switch is used to energize the stator windings for a period of $500ms$. Since the inductance value of the two-finger VR gripper is relatively high, for the stator current to flow at $50Hz$ with both windings connected in series, it can be expected that the $d\lambda/dt$ term would generate a significant proportion of voltage potential difference. Current information can be measured from a low impedance current resistor.

In order to simulate the two-finger VR gripper with separate magnetic circuit, one rotor of the two-finger VR gripper is removed. Figure 4.10 shows the equivalent magnetic circuit of the two-finger VR gripper with one rotor being removed and only one stator winding being excited. With one rotor being removed, it can be assumed that the flux link through path HJK and such setup can be assumed to be equivalent as a two-finger

VR gripper with separate magnetic circuits as shown in Figure 3.3(b).

Flux-linkage is measured with stator current ranging from $0.5A$ to $7A$, in incremental current steps of $0.5A$. The angular position ranges from the fully unaligned position of 0^o to the fully aligned position of 65^o in an incremental steps of 0.5^o. Under this condition, two sets of flux-linkage results, λ versus current, i and λ versus angular positions, θ are recorded.

The measured data is acquired at a frequency of $5kHz$. This provides a data rate of 100 samples per cycle. Two VR grippers configuration are measured. The VR gripper with only one rotor is shown in Figure 4.10(a). The corresponding equivalent magnetic circuit is shown in Figure 4.10(b). This can be assumed to be simulating the effect of the finger driven by an ordinary VR actuator without any magnetic coupling effect. The other set of results were recorded with both stator windings being excited at the same current level and rotors being locked at same angular positions. These data shows the actual performance of the VR finger gripper with magnetic coupled effect.

Figure 4.11 shows the experimental setup for AC excitation flux-linkage measurement of the two-finger VR gripper. Search coils are placed on the input limb and the rotor of the magnetic circuits. Different voltages induced from the search coils and stator current levels are filtered, amplified and fed into the ADC channels. Encoders are also connected to measure angular position accurately. The overall experimental setup for two-finger VR gripper is shown in Figure 4.11.

For simplicity, hysteresis loops of a magnetic circuit with air-gap, H_{total}, can be decomposed into two separate components, namely H_{core}, the core and $H_{air-gap}$, air-gap. The magnetic circuit can be described as:

$$H_{total} = H_{core} + H_{air-gap} \tag{4.12}$$

Figure 4.12(a), Figure 4.12(b) and Figure 4.12(c) show the hysteresis loops of the iron

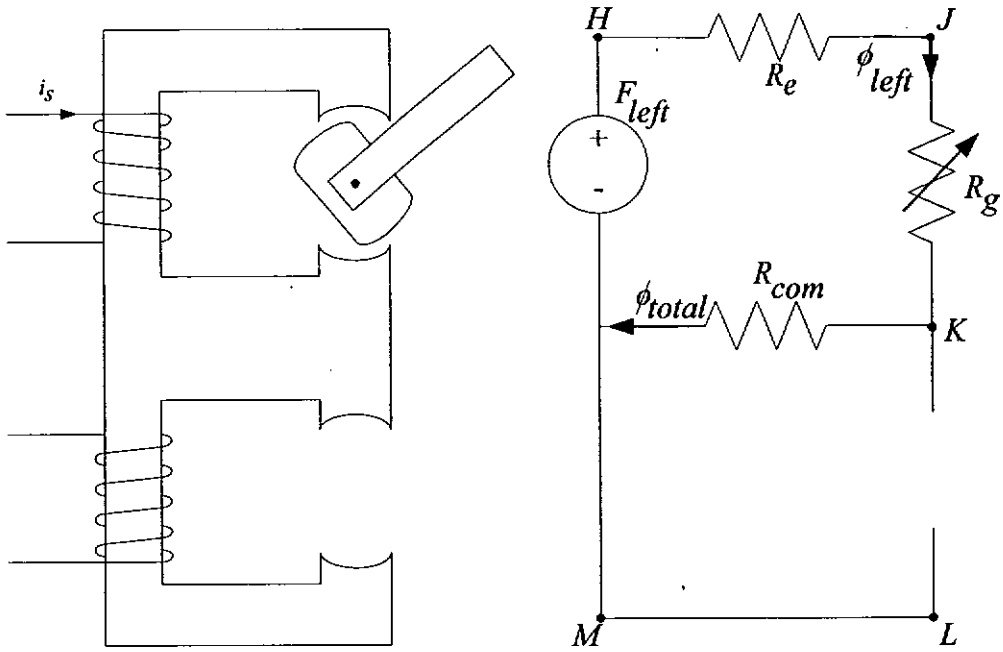

(a) Two-finger VR gripper with only one rotor installed (b) Simulated equivalent magnetic circuit

Figure 4.10: The two-finger VR gripper setup for simulating without magnetic coupling

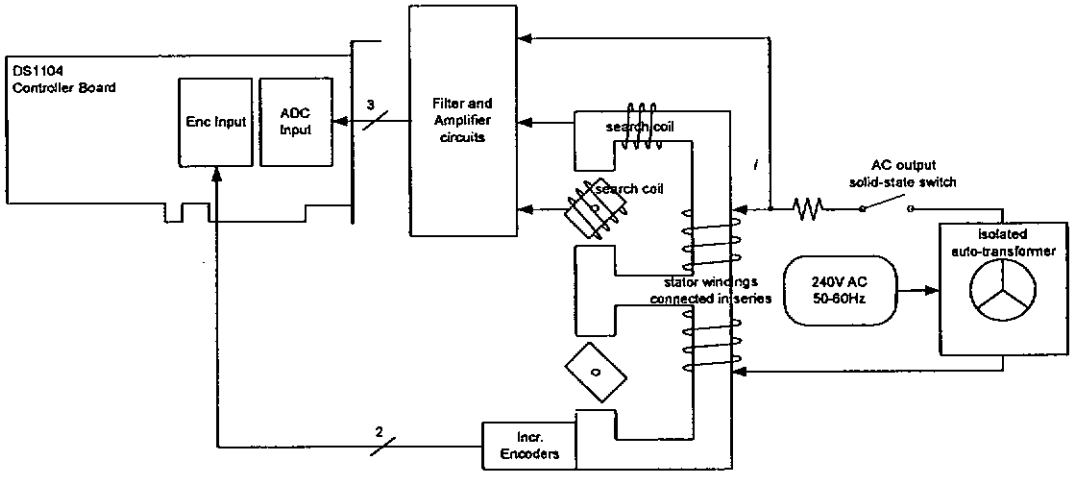

Figure 4.11: Experimental setup for AC excitation flux-linkage measurement of the two-finger VR gripper

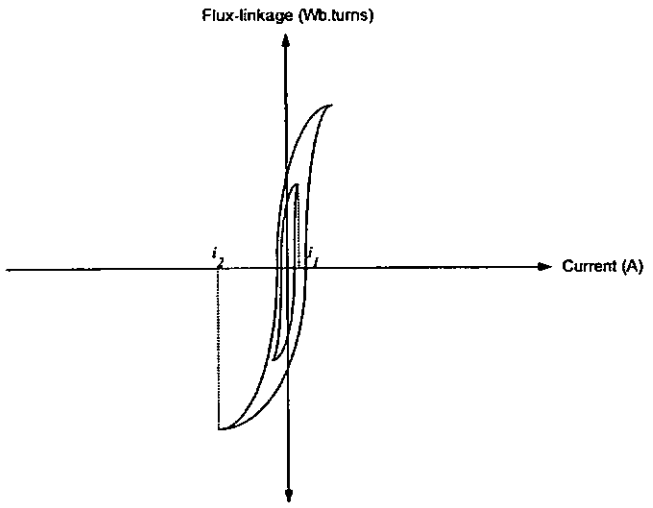

(a) Hysteresis loop of an iron core

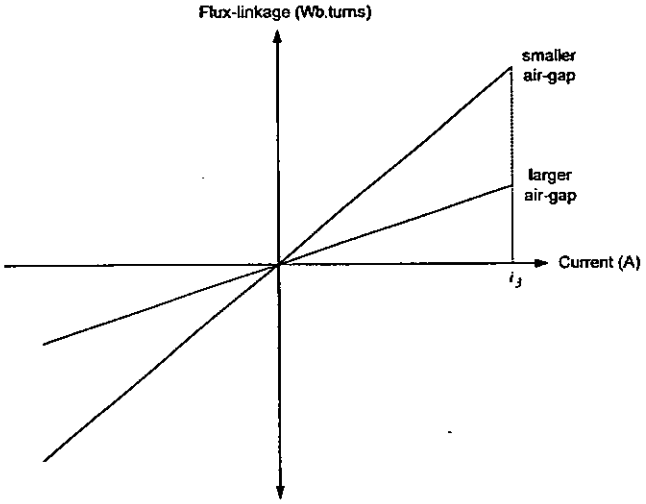

(b) Hysteresis loop of an air-gap

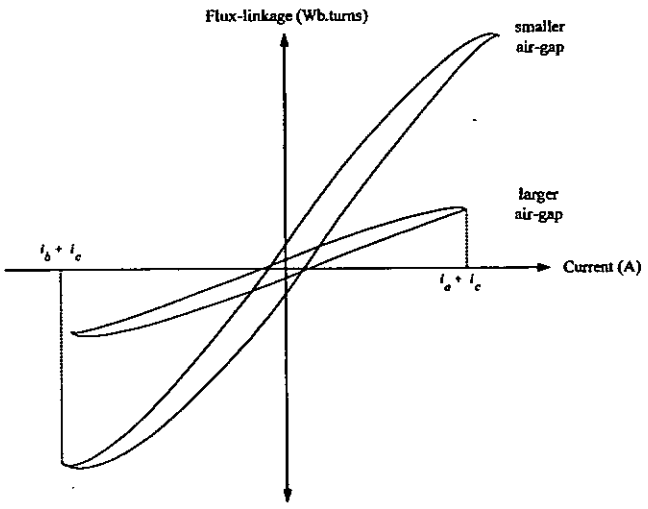

(c) The complete magnetic circuit loop

Figure 4.12: Hysteresis loop of a magnetic circuit with air-gap

core, air-gap and the complete magnetic circuit [67].

The iron core suffers from hysteresis loss. As shown in Figure 4.12(a), small value of reluctance in the core tends to have a steep slope. As the current level increases from i_a to i_b, the flux-linkage value tends to increase with the similar slope but with a larger area. This indicates that hysteresis loss is increased. However, this increase in flux-linkage value would change once the magnetic circuit reaches and enters saturation region. The saturation effect is due to the nonlinear relationship between Magnetic flux density, T (B) and Magnetic field intensity, Am^{-1} (H) of the iron core.

On the other hand, the air-gap has no iron and thus Figure 4.12(b) shows no hysteresis loss. But, with its high reluctance value, it tends to have a gentle slope. As the rotor position changes with the current level remains at i_c, the air-gap size varies. The slope of the hysteresis loop for the air-gap also varies.

The hysteresis loop of the complete magnetic system can be seen as the summing up of the two hysteresis loops. Consequently, any changes within either the air-gap or the iron-core can be reflected upon the hysteresis loop for the complete magnetic system. As the magnetic system approaches to saturation, nonlinear effects exhibit and play critical roles.

Since the reluctance introduced by the air-gap is significantly larger than the core, as a result, it can be expected that any slight variation on the air-gap would produce a large change of flux-linkage value. This causes the complete system to increase its flux-linkage value with its same slope in the similar manner.

4.6.3 Experimental results

Figure 4.13(a) and Figure 4.13(b) show a period of the stator current waveform with peak-peak current at $7A$ and induced voltage sensed by the rotor search coil. The rotors are both at fully aligned positions. Due to the large inductance value, the current has

a large phase delay with respect to stator winding voltage while lead the flux waveform. Besides, the current waveform, i, contains other harmonics [66]:

$$i = i_1 + i_3 + i_5 + \cdots \tag{4.13}$$

where i_1, i_3 and i_5 represent the first, third and fifth harmonics of the current, i, respectively.

Figure 4.14(a) and Figure 4.14(b) show the hysteresis loops of the two-finger VR gripper with both rotors installed. Results are measured at different rotor positions and different current levels respectively.

From Figure 4.14(a), it is clearly shown that flux-linkage level varies significantly with respect to the change of rotor positions. Changing from fully aligned to fully unaligned positions, flux-linkage value can differ by as much as seven times. At different rotor positions, the two-finger VR gripper enters saturation region at different current levels. The two-finger VR gripper enters saturation region with the lowest current level when the rotors are located at the fully aligned position. The two-finger VR gripper stays within the saturation region below $2A$ without significant flux saturation.

Figure 4.14(b) shows that the flux-linkage increases significantly with current level changes, but less so for rotor position changes. Figure 4.15(a) and 4.15(b) show the hysteresis loops of the emulated VR actuator at different rotor positions and different current levels respectively.

Comparing Figure 4.14(a) and Figure 4.15(a), it can be found that the variation of flux-linkage is larger for two-finger VR gripper that the VR actuator. Since actuator torque is proportional to the change of flux-linkage, in other words, the two-finger VR gripper should produce a larger torque overall. However, it can also be noticed that before entering into saturation region, VR actuator produces slightly higher flux-linkage value than the two-finger VR gripper. So there might be under certain condition, the

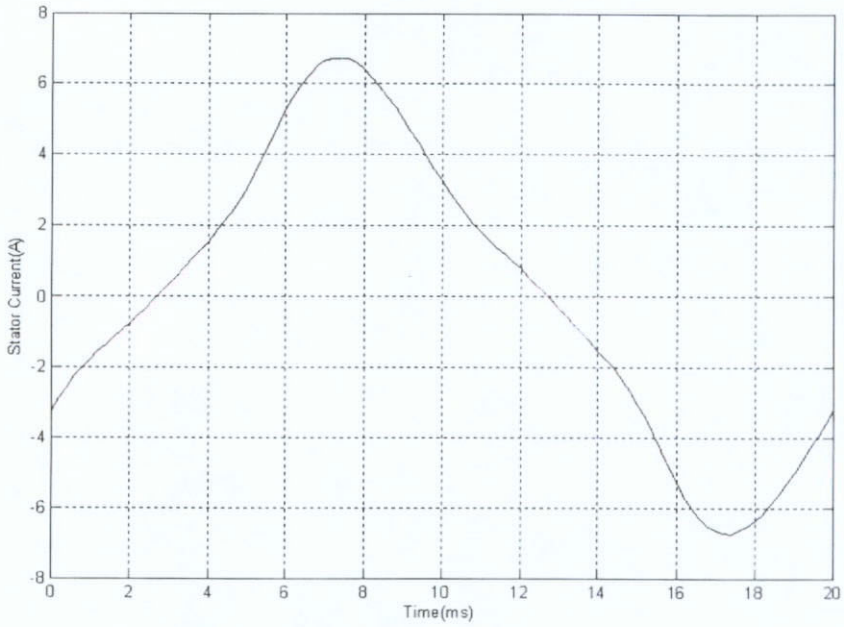

(a) stator current

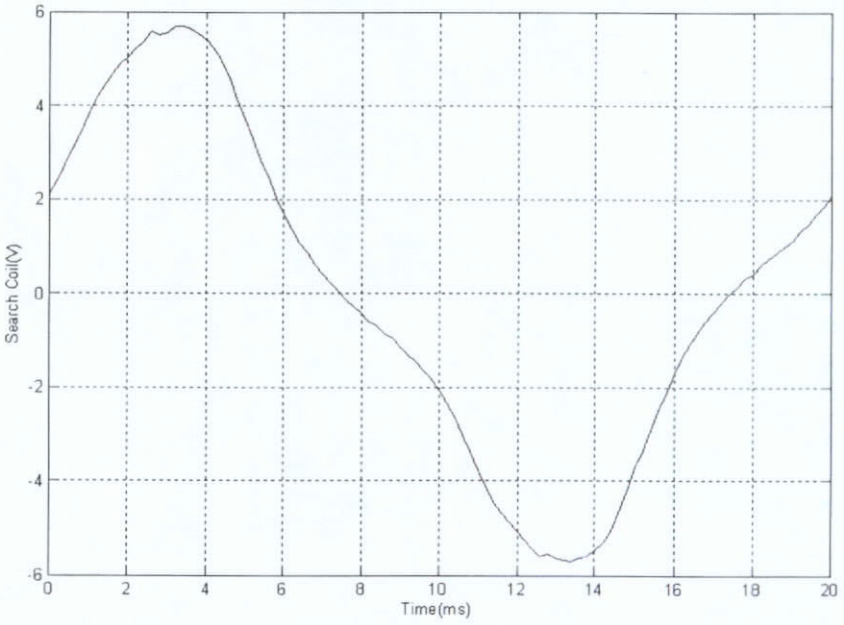

(b) induced voltage by search coil wounded around one of the rotors

Figure 4.13: Alternating excitation measurement

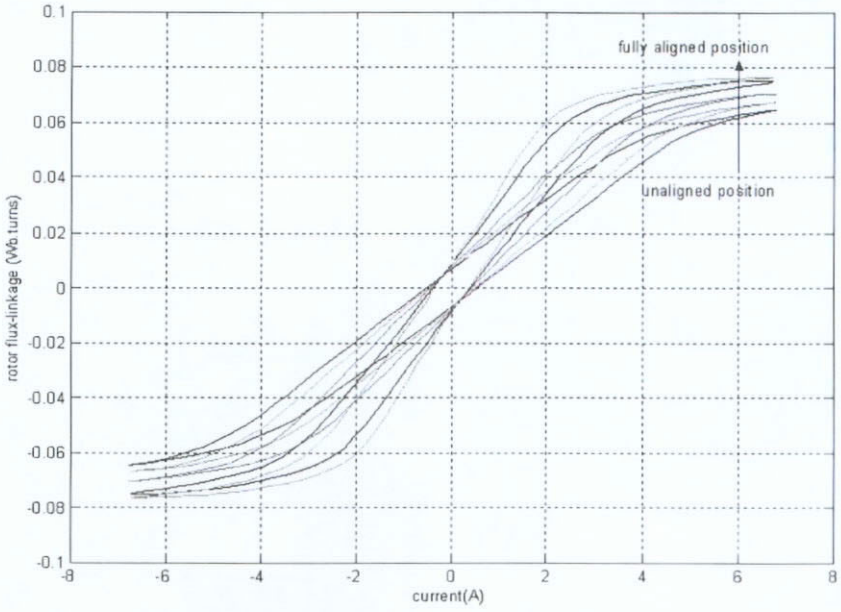

(a) Measured at different rotor angles

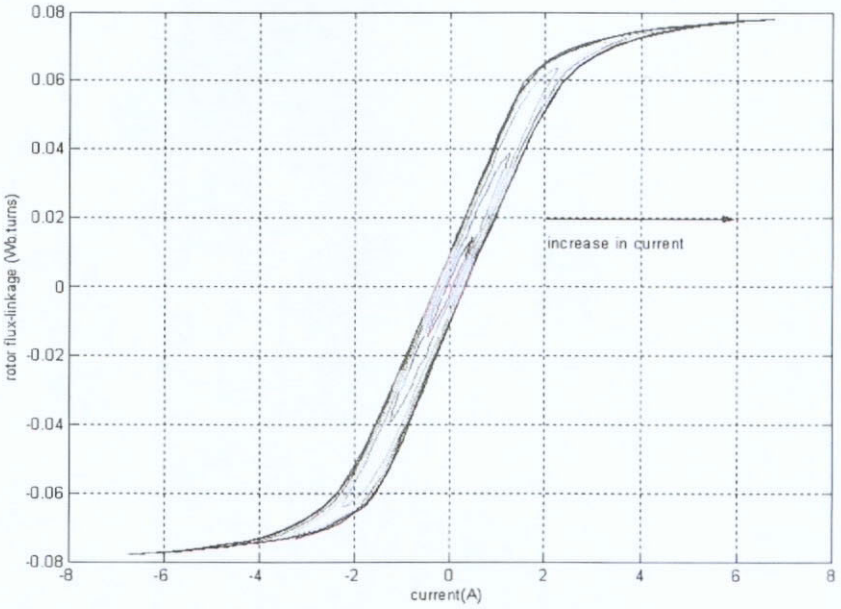

(b) Measured at different current levels

Figure 4.14: Hysteresis loops of the two-finger VR gripper

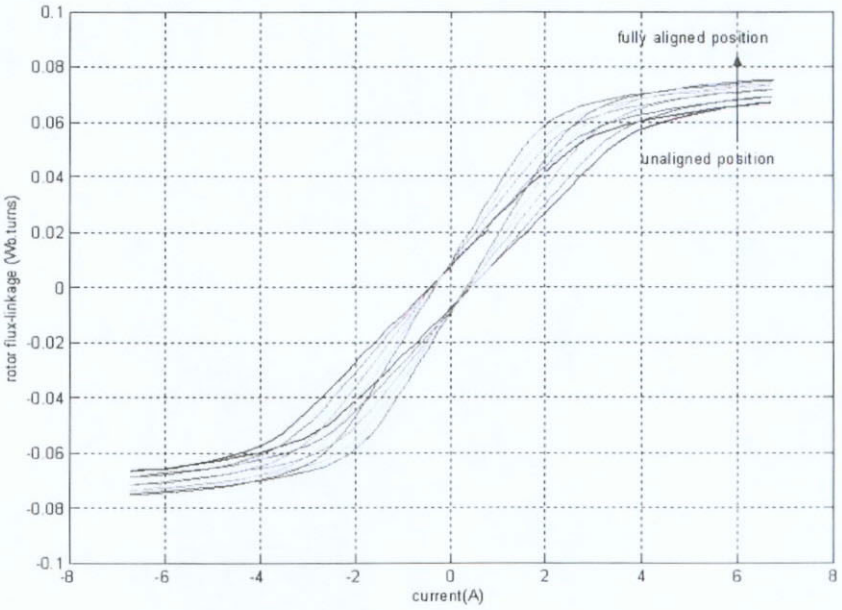

(a) Measured at different rotor angles

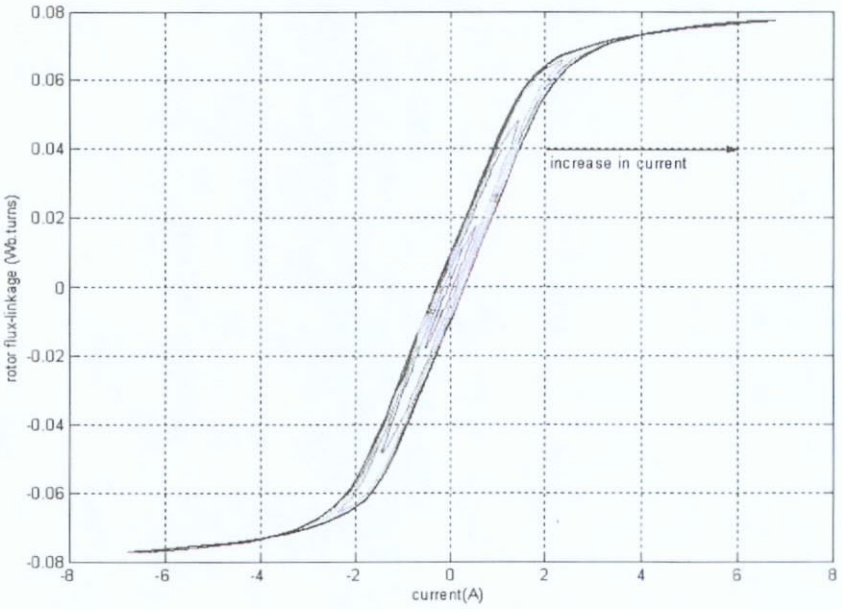

(b) Measured at different current levels

Figure 4.15: Hysteresis loops of an emulated VR actuator

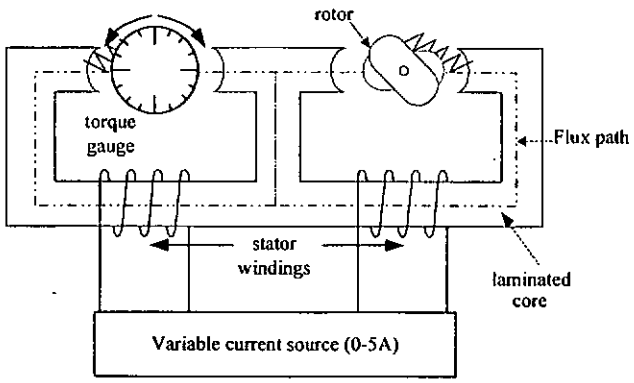

Figure 4.16: Direct torque measurement setup for the two-finger VR gripper

VR actuator can generate higher torque than the two-finger VR gripper. With the information obtained, it is difficult to get a clear picture whether the two-finger VR gripper or VR actuator is more efficient.

4.7 Direct torque measurement

In order to distinguish that whether by combining two VR actuators, configuration A, is more efficient than driving the two fingers by individual VR actuators, configuration B, the simplest way is to measure the rotor torque of the two-finger VR gripper directly.

Figure 4.16 shows the setup of the direct torque measurement. A torque gauge is mounted onto the rotor shaft. Torque measurement are recorded from current level ranging from $0.5A$ to $4A$ with both rotors fixed at same angles ranging from 0^o to 65^o.

4.7.1 Experimental results

Figure 4.17(a) and Figure 4.17(b) show the torque measurement for the two-finger VR gripper with configurations A and B. As shown from the experiment results, when the two-finger VR gripper operates within the linear region i.e. below $2A$, configuration B produces slightly more torque than configuration A, around $3 - 4\%$. It is because before the iron core is saturated, more flux flow within the magnetic circuit. Unlike

configuration A, both flux produce by the two MMF sources counteract against each other. But once the two-finger VR gripper enters the saturation region, configuration A precedes configuration B. At $4A$ current level, the torque production of configuration A exceeds its counterpart by more than 30%. Such difference can be expected to be more obvious as the stator current increases. Since most of the time the two-finger VR gripper operates under saturation region, like the VR actuators, it has shown that with combined magnetic circuit is more effective than single finger gripper with individual magnetic circuit.

For both configuration, both maximum torque readings occur when rotor angle is 35^o. It is because that the rotor pole tips have just overlapped with the stator pole tips and they become heavily saturated. This sudden change of flux results in a high torque generation.

4.8 Leakage flux-linkage

Leakage flux-linkage can be seen as any flux-linkage which does not link through the rotor. Such flux-linkage produces no torque but affects the electrical performance of the two-finger VR gripper. For non-saturated magnetic systems, this effect is often neglected. However for two-finger VR gripper, it operates in saturation region for maximizing its efficiency, so leakage flux cannot be neglected.

Possible leakage flux path is shown in Figure 4.18. With the flux-linkage measurement method employed in section 4.6, leakage flux-linkage can be obtained easily with Equation 4.2.

According to Figure 4.11, search coils are placed at the input limb and rotor of the two-finger VR gripper. Leakage flux-linkage can be calculated:

$$\lambda_l = \lambda - \lambda_s \tag{4.14}$$

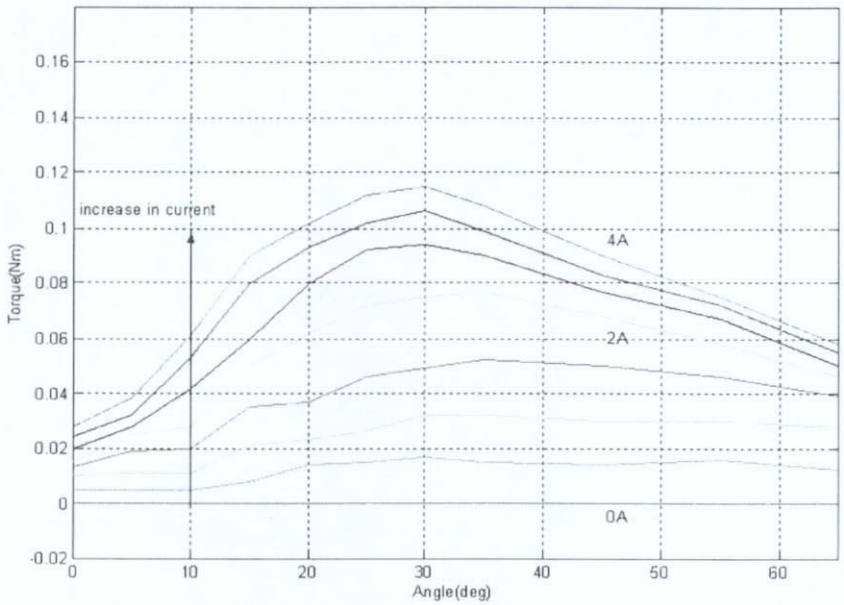

(a) with one stator winding energized

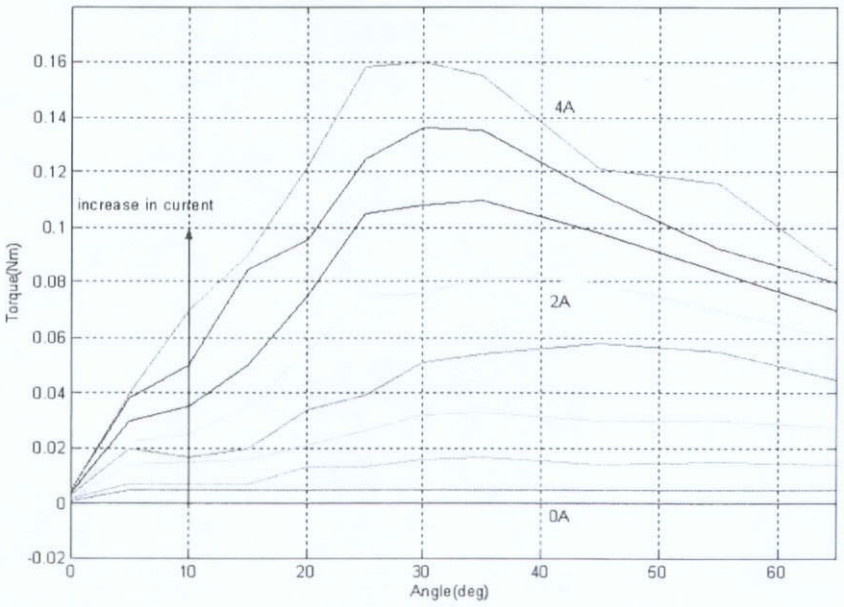

(b) with both stator windings energized

Figure 4.17: Direct torque measurement for the two-finger VR gripper

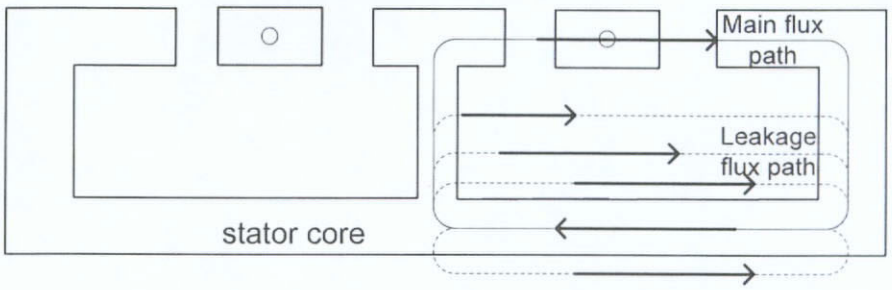

Figure 4.18: Leakage flux-linkage path of the two-finger VR gripper

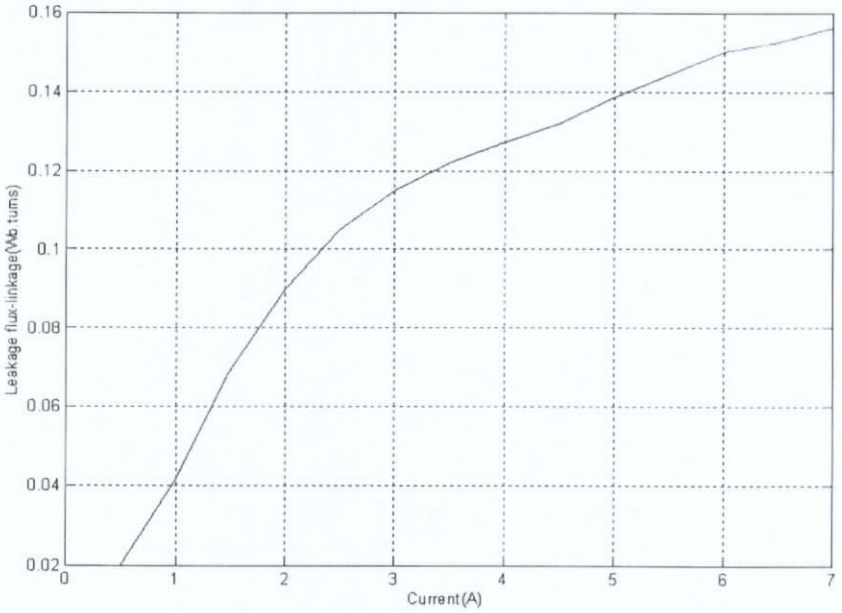

Figure 4.19: Leakage flux-linkage of the two-finger VR gripper

4.8.1 Experimental results

Figure 4.19 shows the leakage flux-linkage of the two-finger VR gripper. The leakage flux-linkage does not show significant variations with respect to changes in rotor positions. Once again, beyond $2A$, the two-finger VR gripper enters the saturation region and leakage flux-linkage saturates. At $7A$, leakage flux-linkage value reaches $0.15Wb.turns$.

	Notation	Values	
Mass	m	0.78	kg
Volume	v	6.63×10^{-5}	m^3
Thickness of lamination	d	0.35×10^{-3}	m
Maximum hysteresis loss at test frequency	P_{f0}	0.6	W/kg
Test frequency	$f0$	60	Hz

Table 4.3: Details of the iron core of the two-finger VR gripper

4.9 Core loss

Core loss is made up of hysteresis loss and eddy current loss. Hysteresis loss, P_f at frequency f is commonly estimated as suggested in Equation 4.15 [44]:

$$P_f = P_{f0}(\frac{f}{f0})^{1.3} \tag{4.15}$$

where P_f and P_{f0} represent the maximum hysteresis loss at frequencies f and $f0$ respectively.

From the information tabulated on Table 4.3, hysteresis loss of the two-finger VR gripper at $3Hz$ can be evaluated with Equation 4.15. Therefore, the hysteresis loss of the two-finger VR gripper at $3Hz$, $P_f = 0.012W$.

Eddy current loss occurs when there is a rapid change of flux within the magnetic circuit [67]. Most of the electrical machineries and transformers are made up of laminated material to reduce the eddy current loss. This is same for the two-finger VR gripper. Generally, lamination of iron cores is an adequate means of limiting eddy currents up to $50kHz$ [67].

The eddy current loss, P_e is given by:

$$P_e = K_e v(\hat{B} f d_{lam})^2 \tag{4.16}$$

where K_e is determined by the type and dimensions of the material, v is the volume

of the stator and rotor, $\hat{B}$ refers to the peak flux density, d_{lam} is the thickness of lamination.

The maximum core loss at $50Hz$ can be obtained by calculating the area enclosed by the hysteresis loop when the stator current is at $7A$ and $\hat{B}$ is equal to $0.7T$. Then, the eddy current loss at $50Hz$ can be found by subtracting the hysteresis loss at $50Hz$ from the core loss.

Core loss in the two-finger VR gripper at $50Hz$ is $11.93W$. Then, the eddy current loss for the two-finger VR gripper at $50Hz$ is $11.47W$. With these information, K_e of Equation 4.16 can be evaluated which is equal to 1.15×10^9. Similarly, the eddy current loss at $3Hz$ is $0.041W$.

With the above results, both the hysteresis and eddy current losses are very low. Then, the flux-linkage model can be simplified by excluding the hysteresis and eddy current effects. Such simplification would contribute less than 10% error.

4.10 Spring stiffness measurement

From Equation 4.6, it is clearly shown that spring torque is one of the variable need to be characterized for the VR gripper. The simplest way of obtaining the spring stiffness is to measure it directly. This can be obtained with direct torque measurement with no current injected into any of the stator windings. So the spring torque can be measured at any angle.

Figure 4.20(a) and Figure 4.20(b) show the spring characteristics and its linearity measurement respectively. In this case, the springs can be assumed to be linear with worst case error less than 6%.

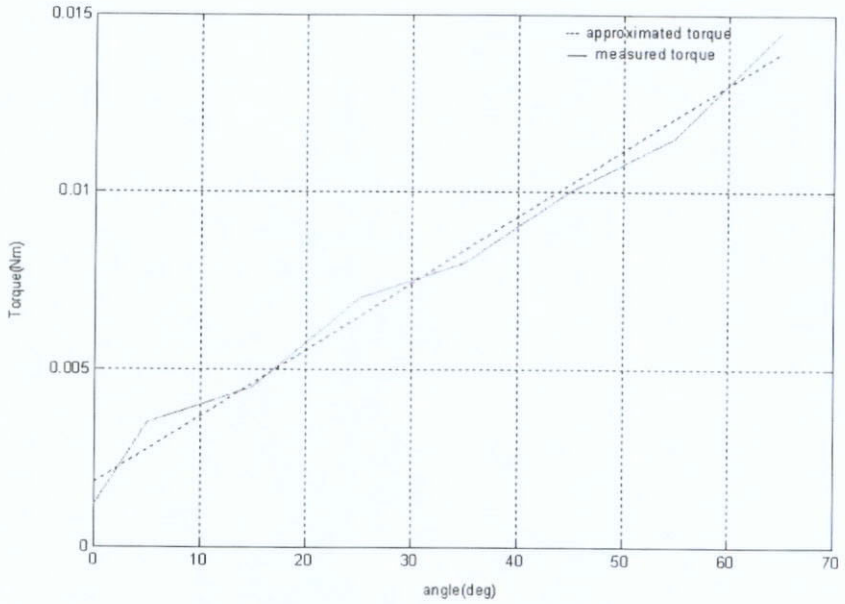

(a) measured and approximate torque

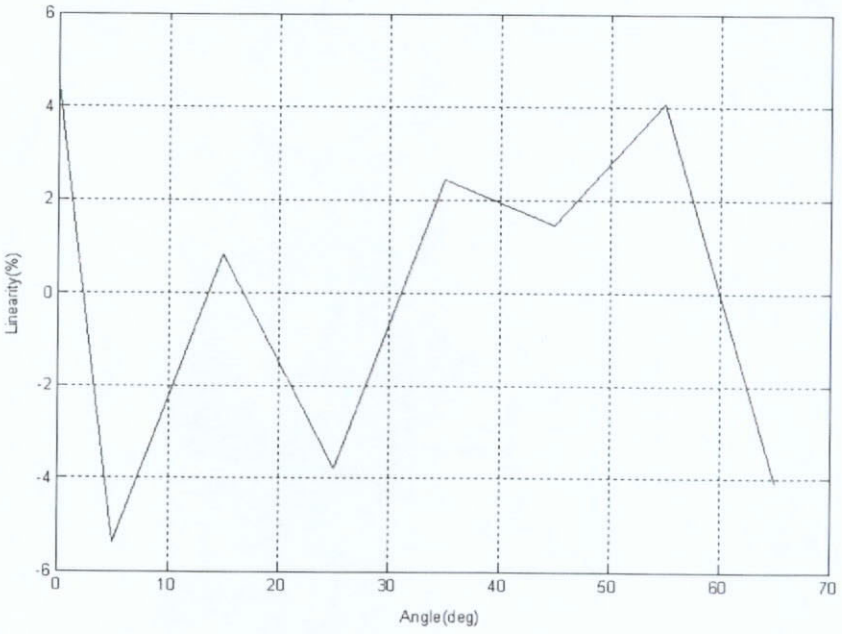

(b) spring torque linearity

Figure 4.20: Torsional spring characteristic

4.11 Summary

In this section, a novel tightly-coupled two-finger VR gripper has been fabricated. The main objective of the chapter is to describe the fabrication of a novel two-finger VR gripper. By combining the two VR actuators, the torque density can be improved. This paper describes the construction of the proposed two-finger VR gripper and its detailed mechanical structure. Various flux-linkage measurement methods have been reviewed. AC excitation method is chosen to be the most appropriate. Flux-linkage measurement was carried out. The measurement results confirmed that the two-finger VR gripper has magnetic characteristics similar to a rotary VR actuator. Direct torque measurement on the VR gripper confirmed that the two-finger VR gripper has a higher efficiency at saturation region by combining the two magnetic circuits. In addition of magnetic measurements, other characterisation measurements of the VR gripper, including leakage flux, hysteresis and eddy current losses have been carried out. From these detailed characterisation information, a model of the VR gripper can be constructed for controller design and simulation purposes. This will be described in the next chapter.

Chapter 5

Modeling of the two-finger VR gripper

The main objective of this chapter is to construct a mathematical model of the two-finger VR gripper for controller design and simulation purposes. This chapter describes the construction of the dynamic model, its simulation and verification.

The model of the VR gripper bases on a set of state equations with the nonlinear flux-linkage and torque characteristics described by the exponential description function. The model is verified and confirmed to be accurate. Section 5.1 reviews the general modeling methods for VR actuators. Then section 5.2 and section 5.3 describes the flux-linkage and torque modeling of the two-finger VR gripper and its overall dynamic model. Lastly, section 5.4 shows the simulation and experimental results, which verify that the model of two-finger VR gripper is an accurate representation of the actual device.

5.1 Review of flux-linkage modeling methods

Modeling of flux-linkage and torque of the two-finger VR gripper play important roles on model construction. Over the years, several flux-linkage models were proposed, namely piecewise approximation, parabolic approximation, cubic spline function and exponential description function [70, 64, 74, 34]. Some even directly incorporate a large scale lookup

table which stores the entire flux-linkage characteristic into the model [68].

5.1.1 Piecewise linear approximation

Piecewise approximation is one the simplest flux-linkage approximation for VR motors [70]. Instead of modeling the flux-linkage characteristic directly, it bases on the flux-current plane only and models the flux-current relationship in different sections. This method models the flux-linkage with few different linear polynomials. Generally, the region is divided into three sections, namely linear, saturated and highly saturated regions.

This approximation method is extremely simple and not costly for implementation. However, once the VR motors enter saturation region, the flux-linkage does not necessarily behave linearly. Modeling with a linear equation introduce extra modeling error. It would be simple and useful for rated and average torque generation. However, for simulation and controller design purposes, such method fails to describe the VR finger gripper accurately. So this method is not appropriate for the VR finger gripper.

5.1.2 Parabolic approximation

Similar to piecewise approximation, parabolic approximation models the magnetic characteristics of the VR motor by separating into three different sections. This method has been employed in several research works mentioned in [64, 33]. One curve is used to approximate the magnetization curve for the aligned and unaligned position and two curves are used for both linear and nonlinear part at aligned position. [64] suggested that flux-linkage at unaligned position λ_u can be represented as:

$$\lambda_u(i) = L_u i \tag{5.1}$$

where L_u represents the equivalent inductance for the unaligned position. For flux-linkage at the aligned position, λ_a is divided into two parts. When current is below the saturation current, i.e. the motor is still within the linear region, the flux-linkage is then:

$$\lambda_a(i) = L_a i \tag{5.2}$$

where L_u represents the equivalent inductance for the aligned position in unsaturated region. For the saturated region, λ_a is represented by Equation 5.3.

$$\lambda_a(i) = \lambda_{so} + \sqrt{4a(i - i_{so})} \tag{5.3}$$

where a, λ_{so} and i_{so} are constants describing the parabolic function.

Parabolic approximation is a simple modeling solution for VR motors, however, it assumes the saturation current is constant at all angular positions. However, for actual VR motors, this phenomena is not necessarily true. This technique introduces modeling error especially when the motor operates within saturated region. As a result, this method is not suitable for the VR finger gripper.

5.1.3 Cubic spline function

Cubic spline function is one of the modeling techniques which offers high modeling accuracy especially for nonlinear characteristics [4]. For high accuracy applications, a two-dimensional curve fitting can be found suitable for wide range of VR motors [74].

In [74], this method considers the flux-linkage value at different angular positions and current levels as nodes of defined rectangles. As a result, the entire modeling region is divided into numerous rectangle which can be represented by the nodes. For each rectangle, the flux-linkage can be represented with Equation 5.4.

$$\lambda(\theta, i) = [g_{k1}(\theta), g_{k2}(\theta), g_{k3}(\theta), g_{k4}(\theta)]A \begin{bmatrix} g_{j1}(i) \\ g_{j2}(i) \\ g_{j3}(i) \\ g_{j4}(i) \end{bmatrix} \tag{5.4}$$

where θ and i are angular positions and current levels which are bounded by the nodes of corresponding rectangle. Besides g_{kl} and g_{jl} have to satisfy Equation 5.5 (l=1,2,3,4):

$$\begin{cases} g_{k1}(i) = 1 \\ g_{k2}(i) = \theta - \theta_k \\ g_{k2}(i) = (\theta - \theta_k)^2 \\ g_{k2}(i) = (\theta - \theta_k)^3 \end{cases}, \quad \begin{cases} g_{j1}(i) = 1 \\ g_{j2}(i) = i - i_j \\ g_{j2}(i) = (i - i_j)^2 \\ g_{j2}(i) = (i - i_j)^3 \end{cases} \tag{5.5}$$

and the matrix A is 4×4

$$A = \begin{bmatrix} a_{kj11} & a_{kj12} & a_{kj13} & a_{kj14} \\ a_{kj21} & a_{kj22} & a_{kj23} & a_{kj24} \\ a_{kj31} & a_{kj32} & a_{kj33} & a_{kj34} \\ a_{kj41} & a_{kj42} & a_{kj43} & a_{kj44} \end{bmatrix} \tag{5.6}$$

Cubic spline method suggested in [74] divides the entire modeling range into many separate regions and thus requires high computation power. Generally, it is commonly to choose a fixed point DSP for cost reduction, therefore implementing complex modeling function is difficult. As a result, this method is not suitable for the VR finger gripper especially for real-time modeling and controller design purposes.

5.2 Exponential description function

Above all, the exponential description function is a model tailored for VR motors. First of all, it does not split the magnetization curve into different regions. Unlike other methods, (e.g. piecewise approximation, parabolic approximation), exponential description function avoids the continuity problem.

The self flux-linkage, λ_s is described by an exponential flux model [34]. Then a least square fitting method is applied to the flux-current chart so that the nonlinear exponential function can be represented by the following equations:

$$\lambda_s(\theta, i) = \lambda_{sat}(1 - e^{-if(\theta)}) \tag{5.7}$$

and

$$f(\theta) = a + b\cos\theta + c\cos 2\theta + d\sin\theta + e\sin 2\theta \tag{5.8}$$

where λ_{sat} is a constant of which the magnitude $\geq$ the saturation flux of the motor. From Equation 3.21, the rotor torque T_m, can be represented as [49]:

$$T_m(\theta, i) = \frac{\lambda_{sat}\frac{df(\theta)}{d\theta}}{f(\theta)^2}\left\{1 - [1 + if(\theta)]e^{-f(\theta)i}\right\} \tag{5.9}$$

There are a few advantages with this modeling method.

1. The periodicity of the flux-linkage characteristic is provided by the periodic function shown in Equation 5.8;
2. The saturation effect can also be seen in the torque equation in Equation 5.9 bounded between 0 to $\frac{\lambda_{sat}\frac{df(\theta)}{d\theta}}{f(\theta)^2}$;
3. At any circumstances, the sign of the torque is only determined by the term, $\frac{df(\theta)}{d\theta}$;

Figure 5.1(a) and Figure 5.1(b) show the 3D flux-linkage and torque profiles of the two-finger VR gripper respectively modeled with exponential description function where the modeling parameters are tabulated in Table 5.1.

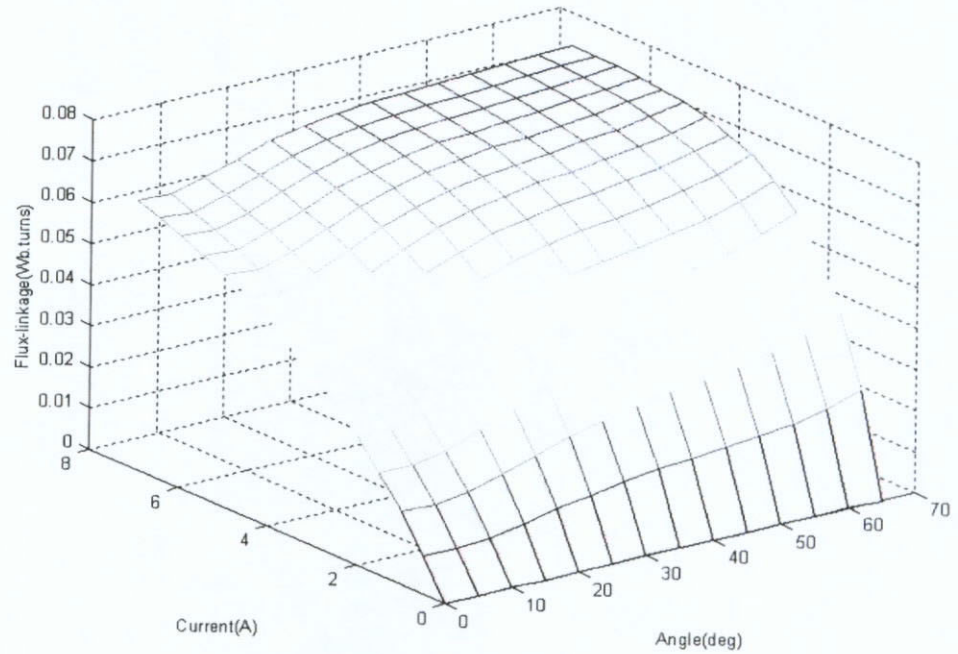

(a) flux-linkage

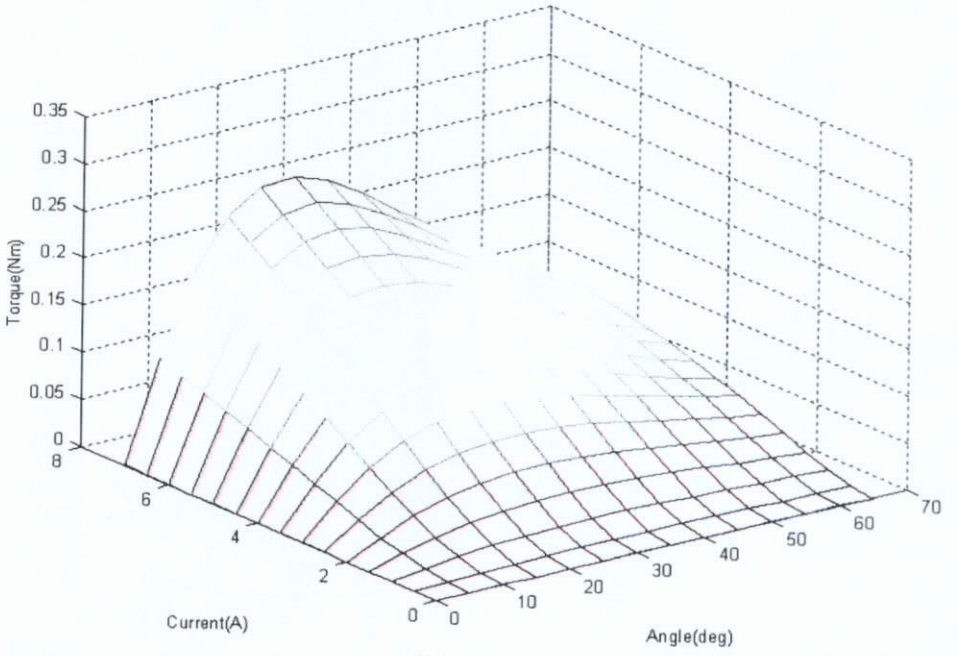

(b) torque

Figure 5.1: 3D characteristic profiles of the two-finger VR gripper

Parameters	Values
a	11.5271
b	-13.194
c	1.9226
d	-7.3743
e	3.5513
λ_{sat}	0.078

Table 5.1: Modeling parameters of the two-finger VR gripper

5.3 Dynamic model of the project two-finger VR gripper

The dynamic model of the two-finger VR gripper can be described by its state equations which are made up of Equation 4.1, 4.2 and 4.6 is rewritten as:

$$\frac{d\theta}{dt} = v \quad . \tag{5.10}$$

$$\frac{dv}{dt} = \frac{1}{J_m}\left(T_m - K_v\dot{\theta} - K_{sp}\theta - T_L\right) \tag{5.11}$$

$$\frac{di}{dt} = \left[V - R_m i - \frac{\partial\lambda_s}{\partial\theta}\cdot\frac{d\theta}{dt}\right]\frac{1}{L_l + \frac{\partial\lambda_s}{\partial i}} \tag{5.12}$$

where L_l represents the leakage inductance of the two-finger VR gripper which can evaluated by :

$$L_l(i) = \frac{d\lambda_l(i)}{di} \tag{5.13}$$

Then,

$$\frac{\partial\lambda_s}{\partial\theta} = \lambda_{sat} i e^{-if(\theta)}\frac{\partial f(\theta)}{\partial\theta} \tag{5.14}$$

$$\frac{\partial\lambda_s}{\partial i} = \lambda_{sat} e^{-if(\theta)} f(\theta) \tag{5.15}$$

In this model, nonlinear friction, hysteresis and eddy current effect are not included.

5.4 Model verification

To verify the proposed model of the two-finger VR gripper, a step pulse is injected into the actuator to find out its overall response. From the system control perspective, impulse responses can be considered as the fingerprint of a particular system under test. However, it is impractical to produce a perfect impulse response; therefore step response is generally used.

In this verification exercise, a block diagram model is built with *SIMULINK* control block, and it is subjected to a step response measurement with a duration of $0.4sec$. Both current waveforms and the rotor positions are recorded. In the experiment, a step voltage is applied across both stator windings of the two-finger VR gripper simultaneously with the current and the rotor positions captured at a sampling frequency of $5kHz$.

Figure 5.2 and Figure 5.3 show the simulation and experimental current and position step responses of the two-finger VR gripper for left and right fingers respectively.

As shown in the results, both simulation and experimental results match closely with each other. When the step voltage is applied at $t = 0$, current rises immediately producing a steep rising slope. Once the current approaches steady state, there is a slight undershoot, which is due to the relatively large back EMF in the magnetic circuit. This is the instance when the rotor reaches its maximum velocity. When the rotor begins to decelerate, the current slowly rises.

For the position responses, there is a slight delay of $20ms$ compared with the current responses. It is because mechanical systems has lower bandwidth compared to the current responses. Besides, the rotor must overcome its static friction and load torque, T_L, before any movement can be made. This can be easily understand from Equation 5.11.

Furthermore, by comparing Figure 5.2(b) and Figure 5.3(b), it can be seen that the right finger peaks $10ms$ earlier than the left finger even though the current level for the

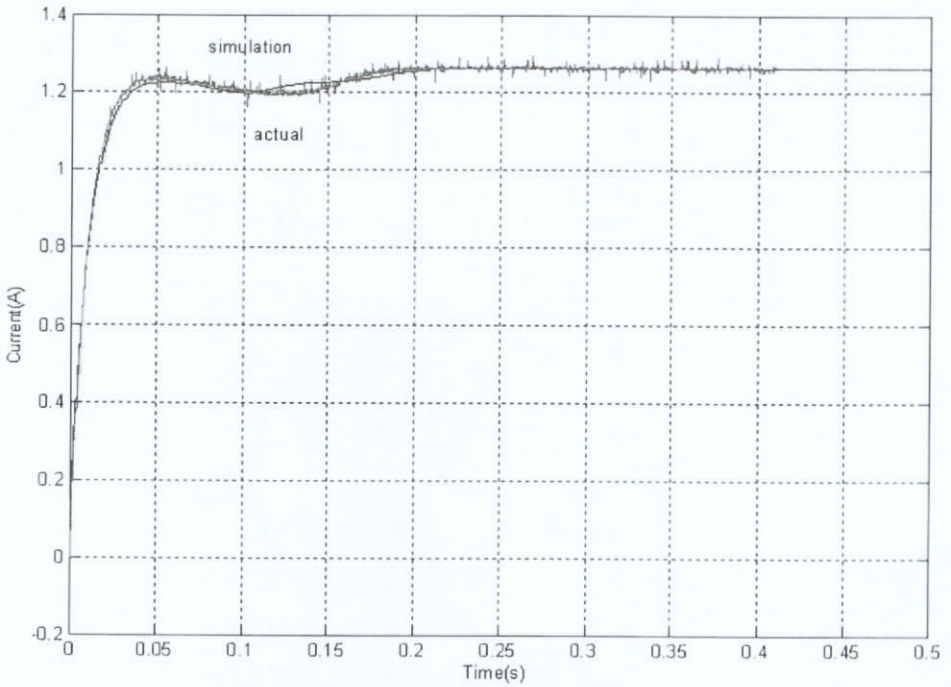

(a) Current step response

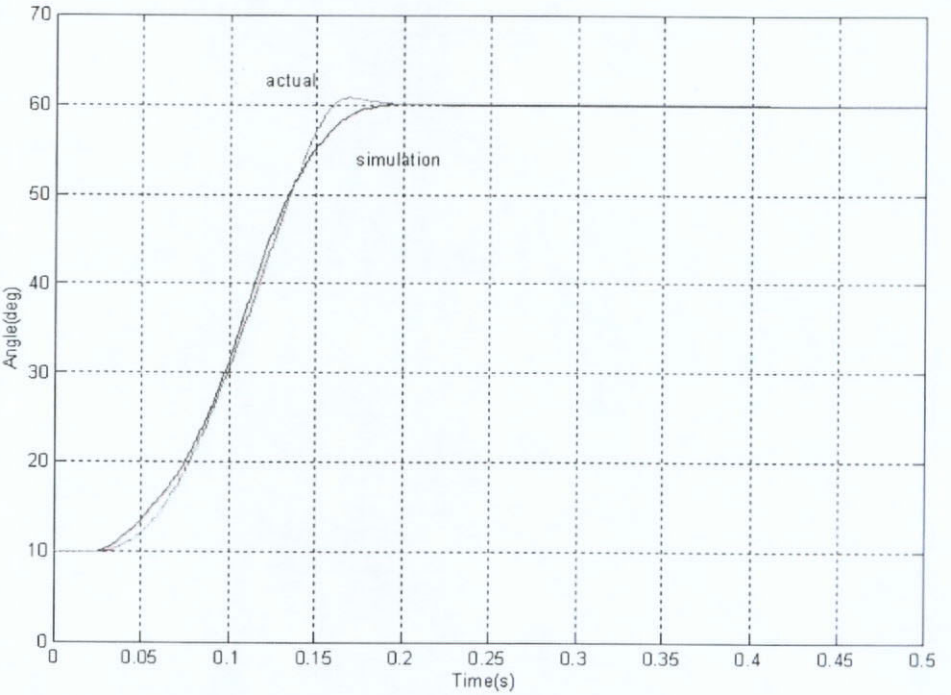

(b) Angle step response

Figure 5.2: Verification results for the left finger of the VR gripper

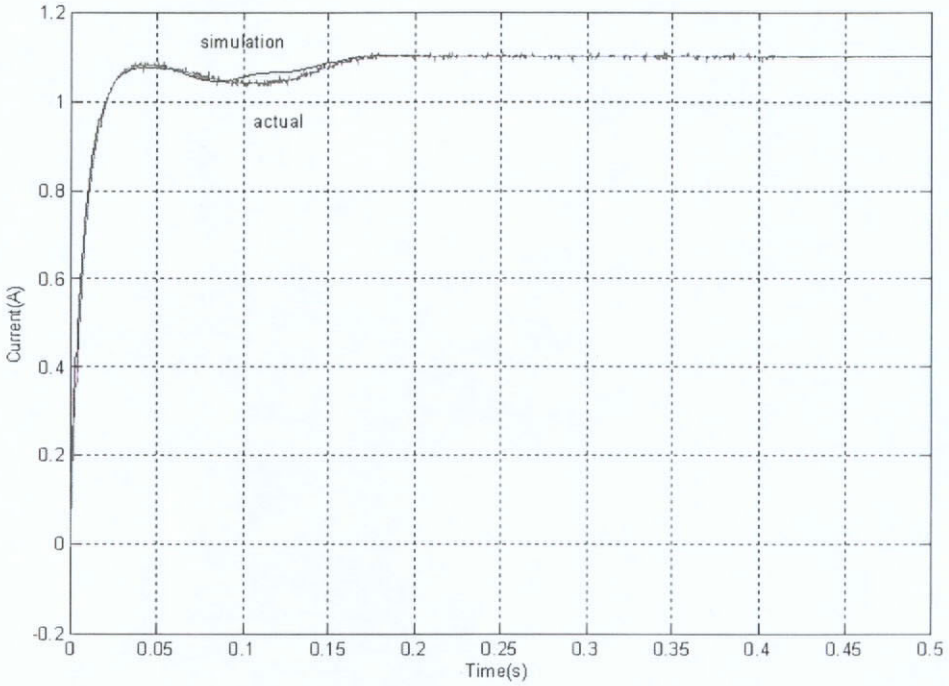

(a) Current step response

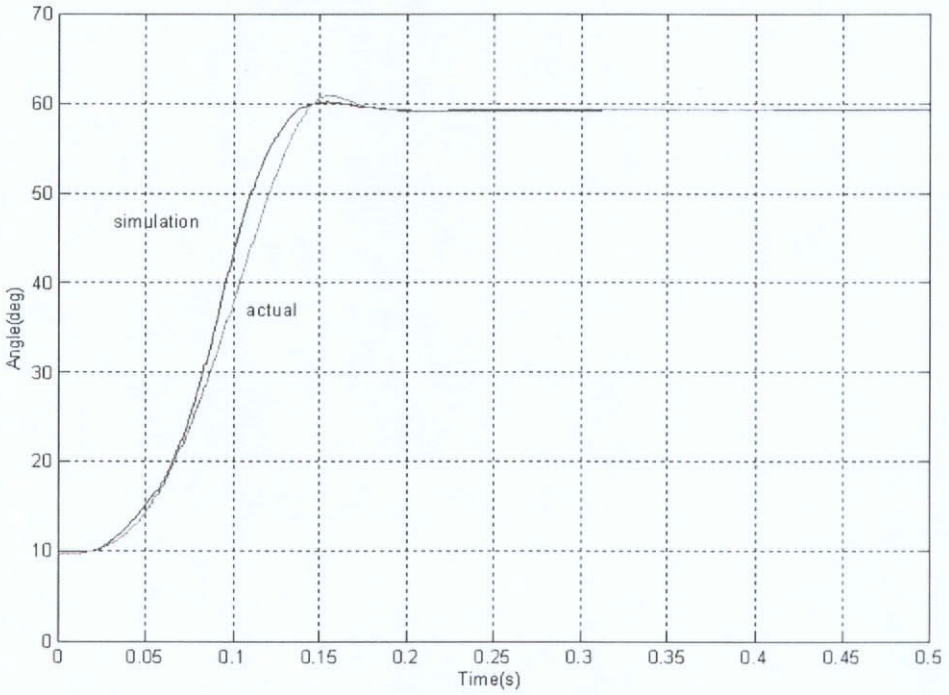

(b) Angle step response

Figure 5.3: Verification results for the right finger of the VR gripper

left finger is higher the right one. Since the mechanical structure of both fingers are symmetrical, which implies the torque production of both rotors are equal. This can be deduced that the left finger has a higher damping or frictional effect than the right finger.

Since the model employed is only a second-order model, higher order dynamics are omitted. This is one of the reason why there is discrepancy between the simulation and experimental results. Furthermore, as mentioned in previous section, some nonlinear properties like friction and hysteresis are omitted from the model.

Above all, it can be concluded that the two-finger VR gripper model is accurate enough for controller design and simulation purposes.

5.5 Summary

In this chapter, the measured flux-linkage characteristic of the two-finger VR gripper which inherits a non-uniform torque profile as a reluctance actuator is modeled with an exponential function. The developed dynamic model of the two-finger VR gripper model is verified with step responses. Results show that the experimental result matches closely with the simulation. It can be concluded that with the dynamic model developed, the two-finger VR gripper is ready for controller design and simulation purposes.

Chapter 6

Adaptive current regulation

This chapter reports on the adaptive current regulation employed in the two-finger VR gripper. The proposed adaptive current regulation scheme can be employed in most VR actuators. It is especially useful for high-precision applications. The inductance profile of a VR actuator is estimated based on the model described in the Chapter 5. Using position and current as input parameters, instantaneous inductance and control parameters can be calculated. It is shown that, the current regulator is capable of adapting to its inductance variation. The method was simulated and tested experimentally on the two-finger VR gripper.

Section 6.1 reviews the general current regulation schemes applied to VR actuators and motors. Section 6.2 proposes the adaptive current regulation scheme for the two-finger VR gripper. Then, simulation of PI control scheme and the adaptive current regulation schemes are conducted and compared with each other, as described in section 6.3. The hardware implementation is described in section 6.4. Finally, section 6.5 shows the experimental results for both PI and adaptive current regulation schemes. Results show that the proposed adaptive current regulation scheme has a faster and symmetrical current responses despite of inductance variation of the two-finger VR gripper.

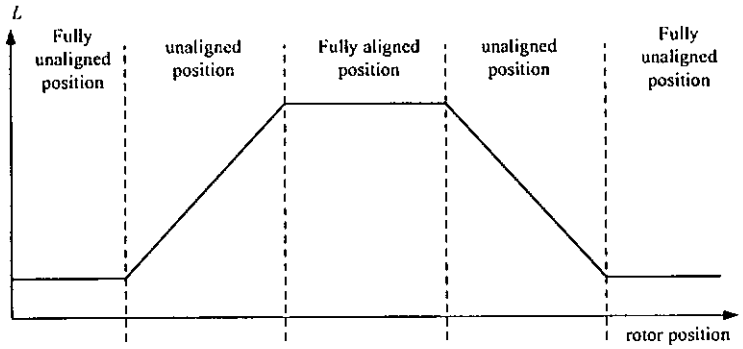

Figure 6.1: A typical inductance profile for VR motor

6.1 Current regulation schemes for VR actuators

The inductance of the VR actuator, the $\frac{\partial \lambda}{\partial i}$ term varies significantly with respect to changes of the rotor position sometimes by as much as 10 times. To achieve high precision motion control of the two-finger VR gripper, the development of a front-end driver with high-performance current regulation becomes a challenging problem.

Since the current regulation serves as the innermost loop within the entire motion control system, a poor current response has a severe impact upon overall system performances. In many high precision force control applications, for example, in wire-bonding of semiconductor chips, no force overshoot is allowed in the actuation system. For this reason, a good current regulation technique is needed.

In Chapter 4, Equation 4.5 shows that the motor inductance, L is a function of rotor position, θ and current, i. Designing an adaptive current regulator with a continuously varying inductance is a challenging problem. With a varying inductance, the $\frac{di}{dt}$ term, which is a dominant term in the motor's current dynamic, also varies. Figure 6.1 shows a typical inductance profile for a VR actuator.

For this type of actuator, its inductance is the lowest value, when the rotor is fully unaligned with the stator poles. Inductance increases as the rotor rotates toward its aligned position and reaches its maximum value as the rotor pole overlaps with the stator poles. For the control of current, two types of current regulation schemes are commonly

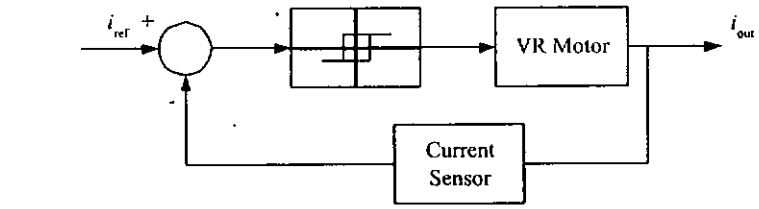

(a) Hysteresis regulator

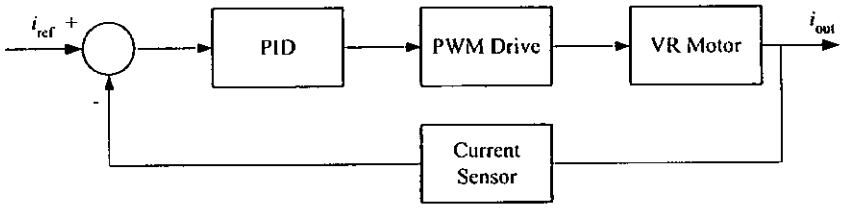

(b) PID regulator

Figure 6.2: Common current regulation block diagram for VR motors

used. They are hysteresis regulator, as shown in Figure 6.2(a) and Proportional, Integral and Differential (PID) regulator, as shown in Figure 6.2(b) [3].

Hysteresis regulator is easy to implement and robust to load variations. It is commonly adopted in stepper current drivers. However, it suffers from large current ripple, especially at low current levels. This is generally acceptable for stepper motor applications because the demand for current accuracy is not high.

PID regulator has less current ripple mainly due to the PWM, the switching frequency of which can be high. It provides a better solution for converter design, but it fails to adapt to inductance variations, especially during fast current dynamics. This regulation technique is commonly found in PM current amplifiers due to their small inductance variations. Conventionally, motor impedance matching technique with PID regulator is widely adopted, especially in industrial applications. This is a simple and effective method for slight inductance variations. However, for VR actuators, such technique cannot produce a flat frequency response with varying inductance. It is because the conventional current regulator is tuned for only a single inductance value, and it cannot accommodate the large inductance change in VR actuators.

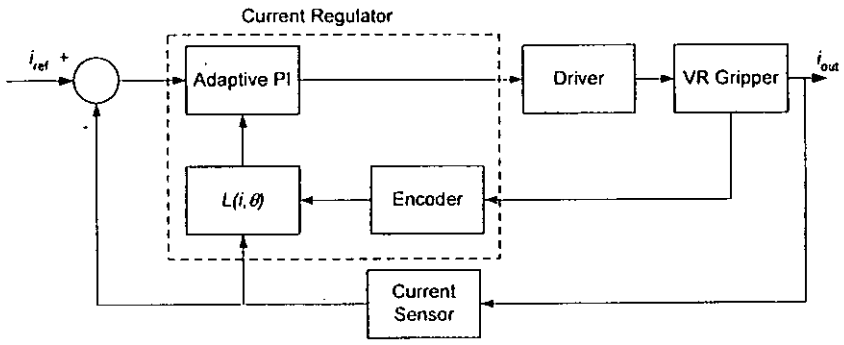

Figure 6.3: Adaptive current regulation block diagram for the two-finger VR gripper

6.2 Adaptive current regulation of the two-finger VR gripper

The block diagram for proposed adaptive current regulation scheme is shown in Figure 6.3. The main objective is to minimize its torque variations by adaptively varying control parameters.

The proposed current regulator structure is similar to classical PID regulator structure. Instead of having a classical PID regulator, it is replaced by an adaptive current regulator as highlighted in Figure 6.3.

In the proposed scheme, inductance and position of the VR actuator are continuously monitored. The measured inductance and the position information are used to vary the current regulator parameters. In this way, the system behaves as a first-order system at all times.

With the motor flux-linkage relationship against current and rotor position obtained in Chapter 5, its inductance profile is then modeled with a nonlinear function. Thus, inductance variation can be calculated on-line with position and current feedback. Therefore, PI parameters can be varied and adapt to inductance variation. The two-finger VR gripper inductance can be represented by the Equation 6.1 [49].

$$\begin{aligned} L(\theta,i) &= L_l(\theta,i) + \frac{\partial \lambda_s(\theta,i)}{\partial i} \\ &= L_l(\theta,i) + \lambda_{sat} f(\theta) e^{-f(\theta)i} \end{aligned} \tag{6.1}$$

where $f(\theta)$ is given by Equation 5.8.

By taking Laplace Transform of Equation 4.5, the transfer function of the two-finger VR gripper can be described as $G(s)$:

$$\begin{aligned} G(s) &= \frac{I(s)}{V(s)} \\ &= \frac{1}{sL(\theta,i) + R_m} \\ &= \frac{1/L(\theta,i)}{s + R_m/L(\theta,i)} \end{aligned} \tag{6.2}$$

Similarly, the transfer function, $T(s)$, of the PI controller is:

$$\begin{aligned} T(s) &= K_p + \frac{K_i}{s} \\ &= \frac{K_p}{s}(s + \frac{K_i}{K_p}) \end{aligned} \tag{6.3}$$

By combining Equation 6.2 and Equation 6.3, the forward transfer function, $C(s)$, can therefore be written as,

$$\begin{aligned} C(s) &= T(s)G(s) \\ &= \left[\frac{K_p}{sL(\theta,i)}\right]\left[\frac{s + K_i/K_p}{s + R_m/L(\theta,i)}\right] \end{aligned} \tag{6.4}$$

By equating $\frac{K_i}{K_p} = \frac{R_m}{L(\theta,i)}$, the pole and zero of Equation 6.4 can be canceled out and the closed-current-loop transfer function, $I_c(s)$ can be reduced to a first order one as:

$$I_c(s) = \frac{K_p/L(\theta,i)}{s + K_p/L(\theta,i)} \tag{6.5}$$

If ω_n is the required bandwidth of the current loop, then K_p and K_i can be found as:

$$K_p = \omega_n L \tag{6.6}$$

$$K_i = \omega_n R_m \tag{6.7}$$

R_m is the resistance of the VR actuator and it can be assumed as a constant. The proposed scheme therefore becomes an adaptive PI current regulator can be implemented with the control parameter continuously modified by the feedback information L. The resulting adaptive PI current regulation will have a consistent current dynamics that is independent of the changes of the reluctance of the actuator. The rotary incremental encoders monitor positions of the two-finger VR gripper and inductance values are calculated with Equation 6.1.

6.3 Simulation

Using the *MATLAB SIMULINK* simulation package, comparison between the performance of the adaptive current regulation and the PI current regulation is carried out. The PI current loop is tuned to a fully aligned position which has a higher inductance value and designed with the same bandwidth as the adaptive PI loop. A step response of $1A$ is put into the simulation models and varies the rotor position from $0^o - 65^o$, open finger to close finger positions.

Figure 6.4 shows the simulation current responses. When the finger is open, there is no overlap between the stator and rotor poles, the load inductance is low. As a result, the current responses are faster than when the fingers are closed. Under this condition, it takes the PI regulator approximately $2ms$ more to settle than its counterpart. However, when the fingers are closed with the load inductance increases, the PI current responses much slower than the adaptive regulated current. The settling time, T_s for the PI regulator at closing finger is $20ms$. On the contrary, it only takes the adaptive regulator $10ms$ to settle. In addition, the adaptive current regulator produces symmetrical current

responses irrespective to the load variations. This indicates that the adaptive current regulator is able to adapt to the load changes. This also shows that the adaptive current regulator has a better response than the PI in terms of both symmetry and settling time.

6.4 Hardware setup

6.4.1 Controller

Through the 16-bits ADC and 24-bits encoder interface, stator currents and rotor positions can be fed back to the regulator. The regulator reads in these inputs at each sampling interval, calculates the control signal by the regulator and issues at its PWM output channels.

The regulator has fast dynamics. Besides, any slight oscillation within this loop can be amplified and exhibited onto the outer loops and deteriorate the entire system performance. Thus, a $5kHz$ sampling rate is selected for this digital current regulator.

6.4.2 Switching power stage

The two-finger VR gripper is driven by a switching power stage. This switching power stage converts controlled PWM signals into the PWM high voltage source and excites the stator coils. The conditioned current signal and encoder position was sampled by the regulator for the calculation of the next controlled signal.

The PWM driver used in this project is a pair of high-low side power Metal Oxide Semiconductor Field effect Transistor (MOSFET)s, IRF740, half-bridge amplifier. It acts as a current amplifier for the motor. It has fewer components than full bridge amplifier and has a true ground that makes current measurement much simpler. The current feedback circuit has a gain of $1.2A/V$. The motor side and logic side is electrically isolated by the opto-couplers that introduces about $300nS$ delay. Dead-time delay protection against cross conduction of the high-low side MOSFETs is introduced. To ensure good

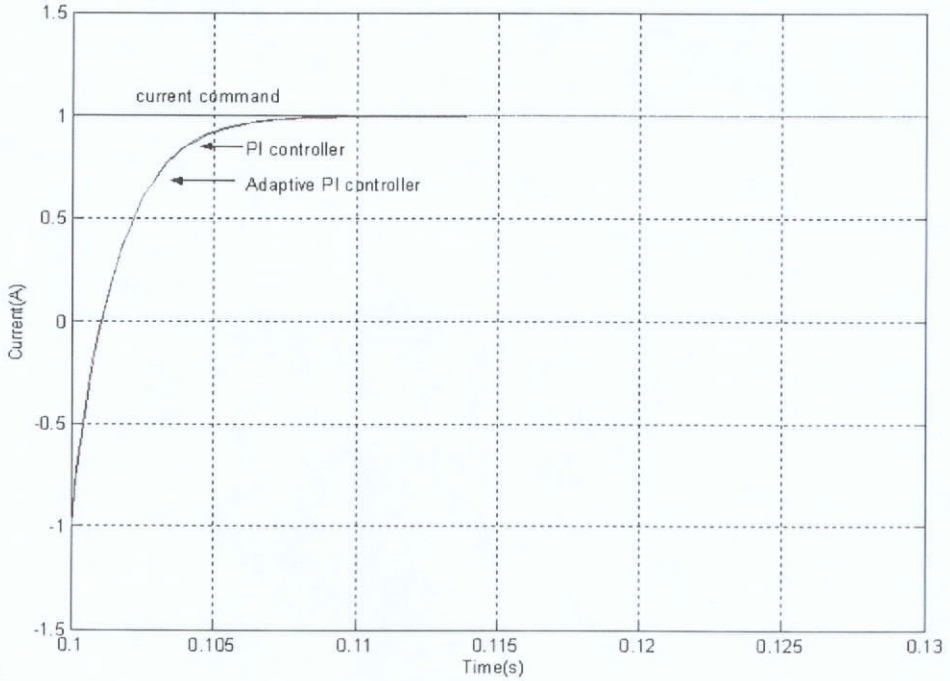

(a) at unaligned position

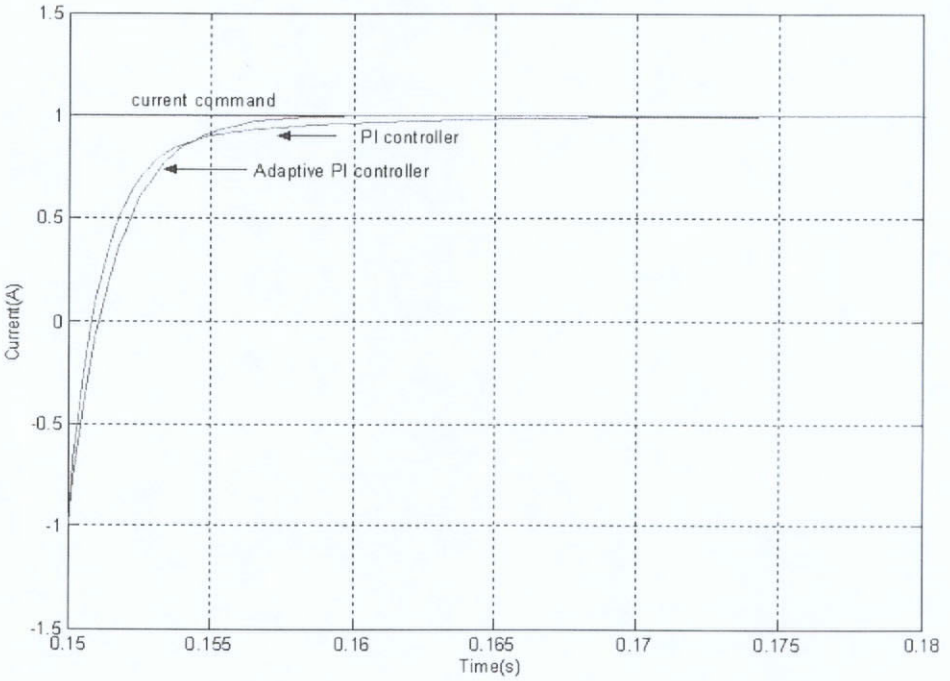

(b) at aligned position

Figure 6.4: Simulation current responses

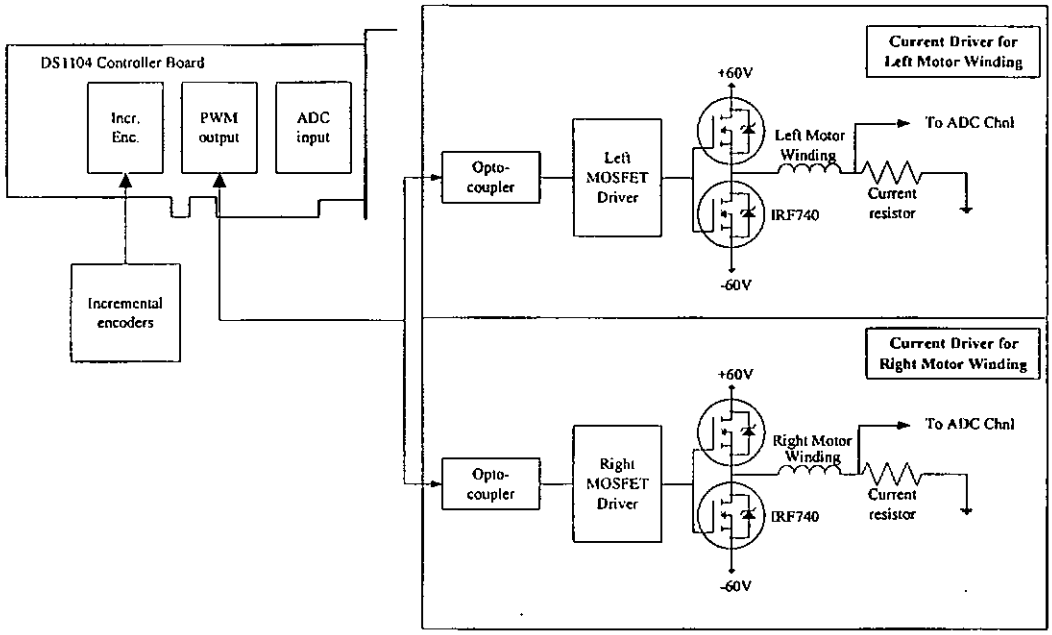

Figure 6.5: Experimental setup for adaptive current control

current dynamics and minimal current ripple, the chopping frequency is set at $24kHz$. Its schematic block diagram of the PWM chopper can be found in Figure 6.5. Figure 6.6 shows the prototype PWM half-bridge amplifier.

6.5 Results

Figure 6.7 shows current waveforms for the controller tracking $1A$ current step command at both open-finger and close-finger positions. Results for the PI and adaptive current regulators are acquired.

Figure 6.7(a) is the current response of the PI and adaptive current regulators with rotors rest at unaligned, open-finger, positions. It shows a good current tracking as both systems are matched with that particular low inductance value.

The current response of the PI and adaptive current regulators with rotors rest at aligned positions which has a 50% increase of the inductance value is shown in

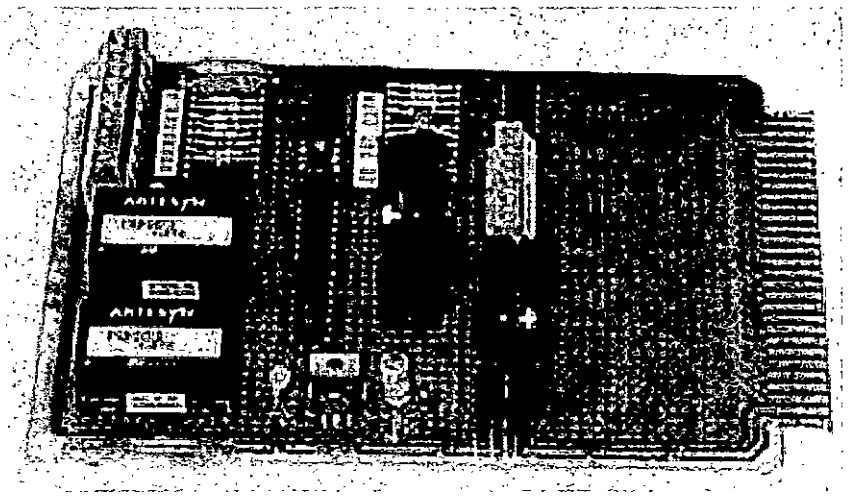

Figure 6.6: Prototype PWM half bridge amplifier

Figure 6.7(b). The adaptive PI loop exhibits a consistent response while the PI loop has a slight overshoot due to the decrease in inductance. This current overshoot lengthens the settling time by $20ms$ while the adaptive current regulator maintains the settling time at $35ms$. Conclusively, the adaptive current regulator is stable at the entire loading range and show good performance for this application.

6.6 Summary

The development of the adaptive current regulator for current drive of the two-finger VR gripper is described in this chapter. The fully digital PI current regulation and the adaptive PI current regulation have been implemented, tested and verified. Both current controllers provide stable results. However, the adaptive PI current regulator shows good tracking despite of 50% load variation. Therefore, the adaptive PI current regulator has been successfully developed and it can provide superior performance on a load with wide variation in inductance. This is especially useful in the current regulation of switched reluctance motors, because their reluctance change can be as high as 3–5 times.

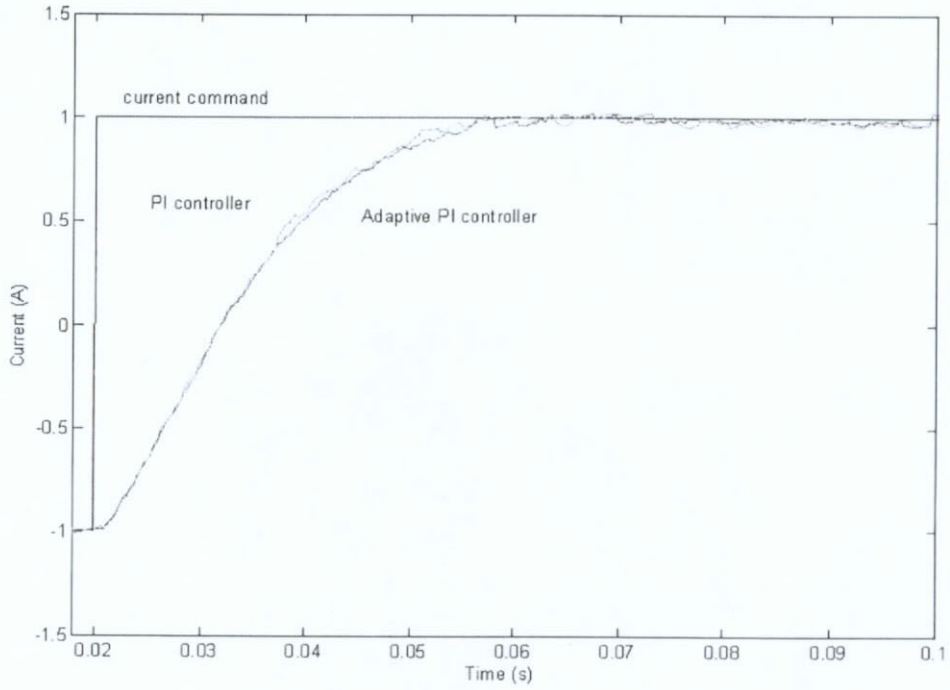

(a) at unaligned position

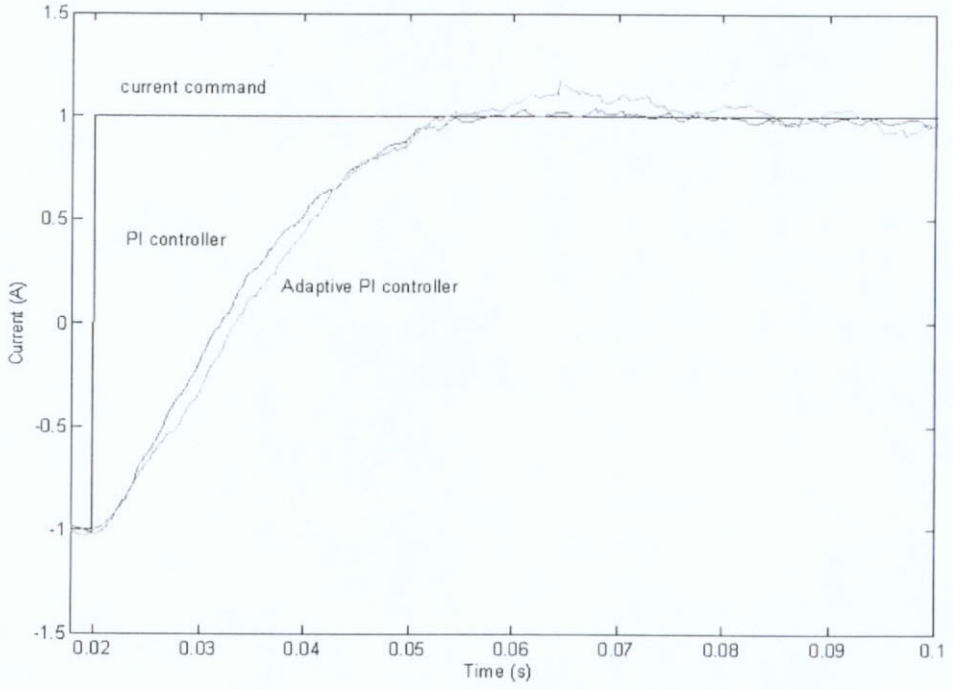

(b) at aligned position

Figure 6.7: Experimental current responses

Chapter 7

Trajectory control using nonlinear lookup table compensator

This chapter describes a nonlinear controller approach to deal with the nonlinear characteristics of the two-finger VR gripper. This approach is a reduced order lookup compensator. It is based on fundamental nonlinear characteristics to understand and relatively low-cost to implement.

Section 7.1 reviews some of the widely used control method for VR motors. Then in section 7.2, principles of the reduced order lookup compensator is proposed and explained in details. Section 7.3 explains the trajectory controller structure of the two-finger VR gripper and an S-curve position command generation is introduced. Lastly, section 7.4 and section 7.5 describe the simulation and experimental implementation results. Results show that the reduced order lookup compensator is a low-cost solution for general applications.

7.1 General control algorithms for VR motors

To convert the nonlinear VR actuator into a proportional device, researchers have developed numerous ideas and adopted various control algorithms to solve the problem.

7.1.1 Full order feedback

The first method is to use full order feedback technique. From nonlinear control perspective, the problem can be solved as a multiple-input nonlinear system [35]. This method provides the full and accurate picture of the VR motor. However, this method requires a large amount of computation power.

7.1.2 Sliding mode control

Another method for controlling nonlinear systems is sliding mode control [18, 36]. It can be considered as the control law switches along a surface [2]. At different operating points of the system, the controller varies its structure. This control method can be a powerful tool to control nonlinear plants.

However its main disadvantage is that once the system reaches its setpoint, the trajectory will move back and forth over the switching surface. This effect is called 'chattering'. For electric motors, this phenomena reduces the efficiency of the motor, generates unnecessary heat loss and reduces tracking precision.

7.1.3 Lookup table

The most common nonlinear compensator is based on lookup table [60, 72]. This method is easy to comprehend and involves much less computation. However, this method is costly in terms of memory storage. Besides, for simulation purposes, inverse lookup tables are also required for both flux-linkage and torque characteristics which places extra cost on memory storage.

7.2 Reduced order lookup table

In this section, a reduced order lookup table is proposed for linearizing the nonlinear properties of the two-finger VR gripper. This method is similar to the method suggested

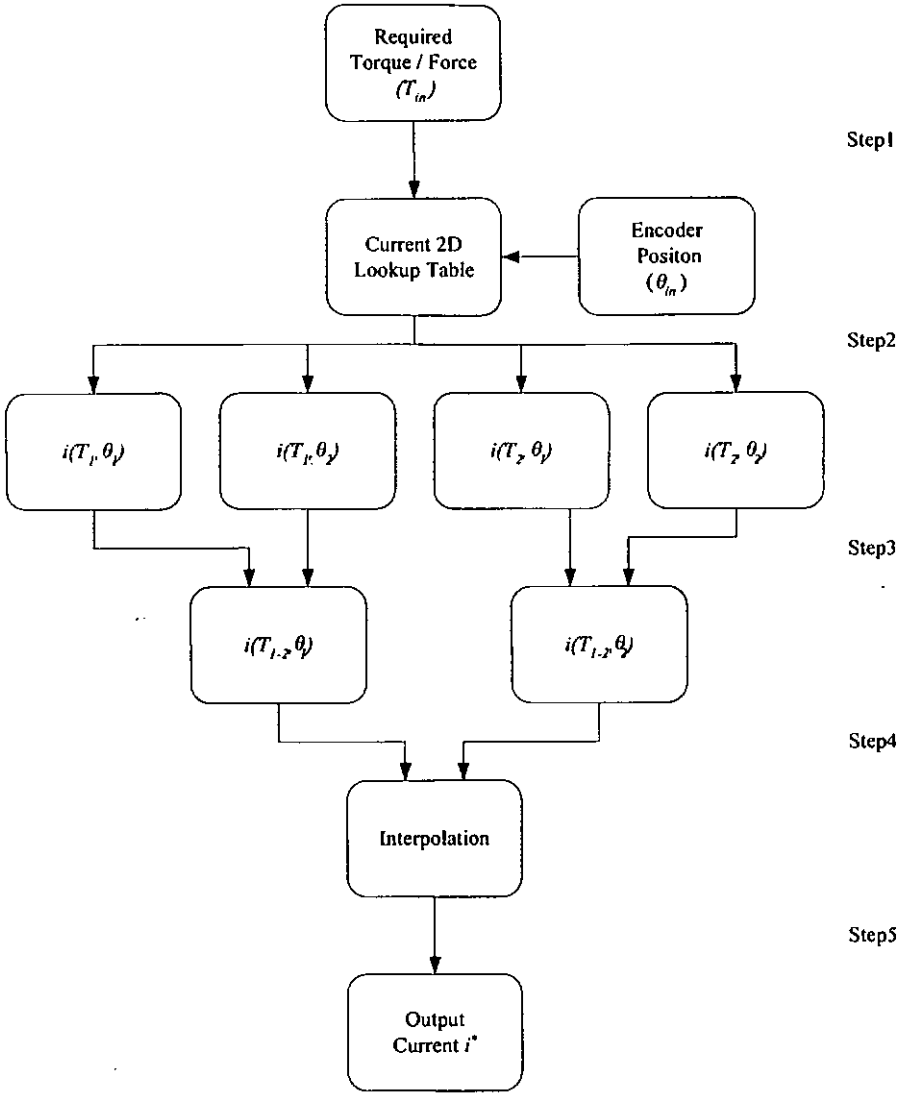

Figure 7.1: Flow chart for obtaining i^*

in section 7.1.3. On the contrary, with the use of interpolation, the reduced order lookup table uses much less memory.

This lookup table bridges the link between the torque command and current regulator. It receives torque command and position information and generates a linearized current command, i^* to the current controller. This nonlinear lookup table is built with the measured torque model, $T(i, \theta)$.

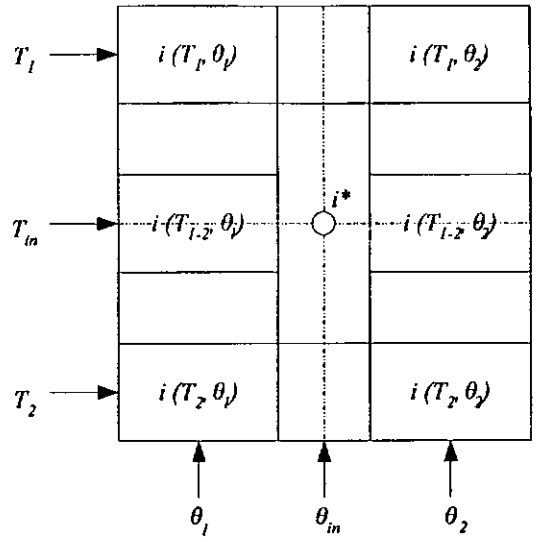

Figure 7.2: Bi-linear interpolation from the reduced order lookup table

For fast calculation and cost effective implementation, a reduced size of 10 × 10 nonlinear lookup table is constructed while the intermediate data points are obtained through interpolation. Figure 7.1 and Figure 7.2 show the flowchart and procedures of obtaining the required current Desired current, A (i^*) by bi-linear interpolation from the lookup table. This table reads the rotor position and desired torque command at each sampling period. Then with the pre-determined torque data, it locates two pairs of data in the lookup table, namely $i(T_1, \theta_1)$, $i(T_2, \theta_1)$ and $i(T_1, \theta_2)$, $i(T_2, \theta_2)$ where $T_1 < T_m < T_2$ and $\theta_1 < \theta_m < \theta_2$. For each pair, a linear interpolation is done, according to the ratio of T_1, T_2, and T_{in}. As a result two intermediate elements $i(T_{1-2}, \theta_1)$ and $i(T_{1-2}, \theta_2)$ are obtained. Finally, the output current command i^* is obtained by interpolating the two intermediate elements with θ_1, θ_2, and θ_{in}. The equivalent open loop transfer function, $G(s)$ can then be described as:

$$G(s) = \frac{1}{J_m s^2 + K_v s + K_{sp}} \tag{7.1}$$

where J_m, K_v and K_{sp} are rotor inertia, viscous damping and spring constant respectively. By comparing the coefficients of a second order equation, natural frequency, ω_n is equal to $\sqrt{\frac{K_{sp}}{J_m}}$.

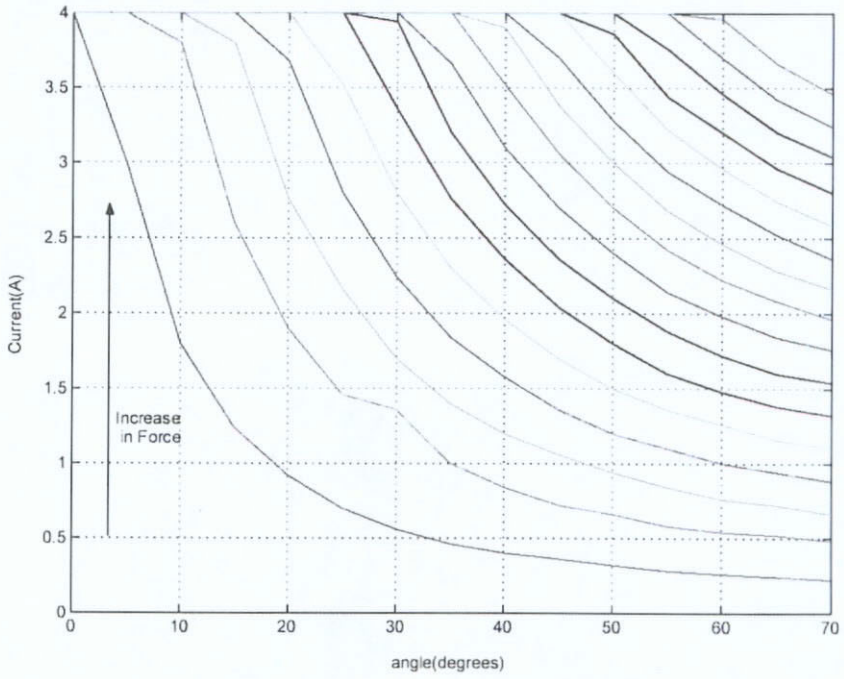

Figure 7.3: Linearized current profile of the two-finger VR gripper

In order to achieve high speed operation for the two-finger VR gripper, it is necessary to obtain a higher spring-to-inertia ratio, i.e. a stiffer spring and a lower inertia. However, inertia cannot be infinitely small, since it is dependent on the rotational mass. Moreover, a spring with high stiffness will reduce the gripping torque. In this experiment, K_{sp} and J_m are designed as $0.018Nm$ and $0.0015mNms^2$ or $0.015mNm^2$ respectively. Under this situation, ω_n has a respectable figure of $110rads^{-1}$ for high-precision applications.

Figure 7.3 shows the linearized current profile of the two-finger VR gripper. The controller's operation is based on the assumption that the current controller has perfect tracking capability and linearity. In order to have a good control of force, stator current must be highly stable, fast in dynamics and excellent in linearity with minimal drifting of current against time and temperature.

7.3 Trajectory control

With the reduced order lookup table compensator, the two-finger VR gripper can then be considered as a pseudo linear device. For simplicity, trajectory control of the two-finger VR gripper can then be achieved with a PID controller. In other words, the nonlinear trajectory controller consists of two major components, namely:

1. Reduced order lookup table compensator for linearizing the nonlinear characteristics of the two-finger VR gripper;
2. A classical PID controller for determining the required torque at every sampling instance with trajectory error information and providing robustness for the entire controlled system.

Generally, sharp overshoot in both position and current can result with a step command input. A command profile is required to provide a swift settling time and reduce the stress on the mechanical system. Furthermore, such command prevents the control signals from saturation and the overall trajectory tracking can then be improved.

An S-curve formula generates the high-speed point-to-point trajectory profile which is shown in Equation 7.2.

$$cmd = \frac{t}{t + e^{c_1 - c_2 t}} \tag{7.2}$$

where c_1 and c_2 are the parameters that shape the curve [25].

As a result, only certain frequency spectrum is allowed into the system and unnecessary high frequency are rejected. This reduces the excitation to the mechanical parts and increases in reliability of the motion process. With less excitation, the system enjoys a faster settling time and an increase in throughput.

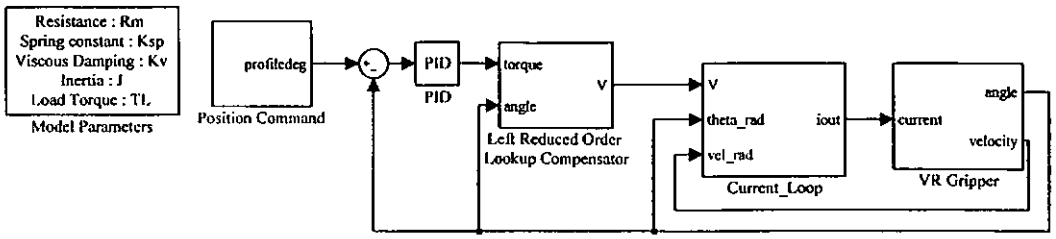

Figure 7.4: Simulation block diagram for reduced order lookup table compensator of the two-finger VR gripper

7.4 Simulation

Simulation is carried out with *MATLAB SIMULINK* and its block diagram is shown as Fig 7.4. The position command which begins from 20^o to 40^o, is generated with Equation 7.2. The entire profile time is $2sec$.

Simulation results show that the actuator is capable of achieving high trajectory response. The trajectory waveform and its error can be found in Figure 7.5(a) and Figure 7.5(b). Results indicate that the two-finger VR gripper follows the command smoothly without any steady state error. The dynamic tracking error is less than 0.5^o.

Figure 7.5(c) shows the tracking current waveform. As the finger rotates away from its initial angle, current increases. This is because as angle increases, the spring torque also increases which requires additional torque to compensate. Besides, extra torque is required for accelerating the rotor. As profile time, $t_{prof} = 1s$, the rotor begins to decelerate. At the same time, the rotor and stator poles begin to overlap and produce a sudden change in reluctance. Such changes generates a large torque and therefore the required current drops. When the profile finishes at $t_{prof} = 2s$, current holds still to compensate for the spring torque. Similar phenomena can be seen as the finger returns to its initial position.

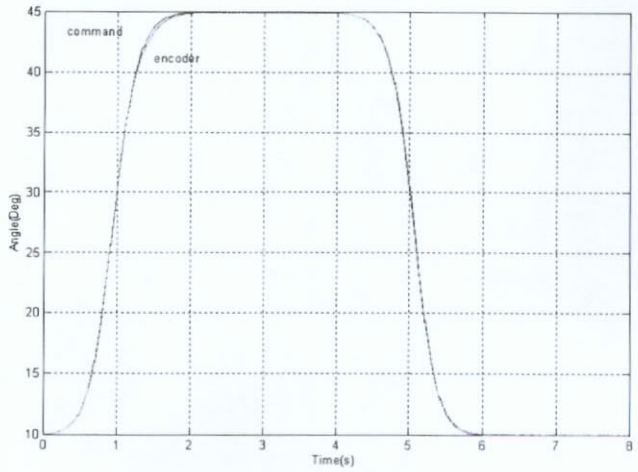

(a) position

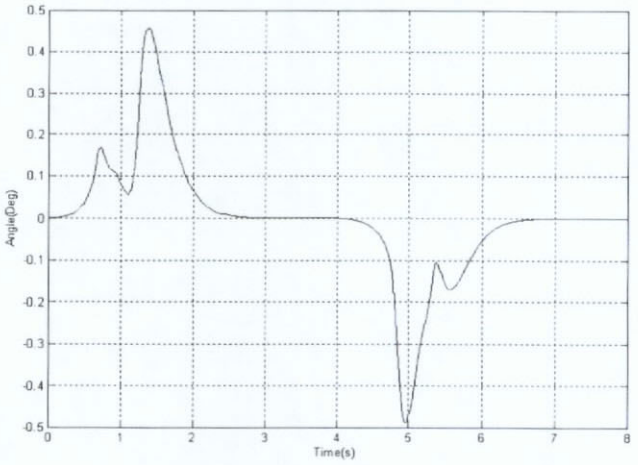

(b) error

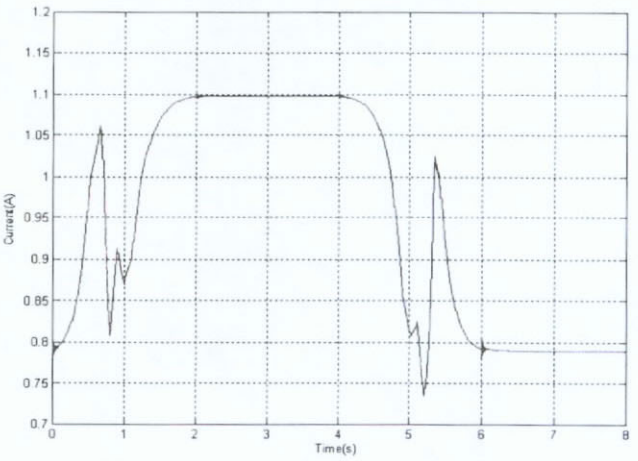

(c) current

Figure 7.5: Trajectory simulation responses of the two-finger VR gripper with reduced order lookup table compensator

7.5 Implementation

With the simulation result shown that the two-finger VR gripper is stable and exhibit high-performance tracking, the proposed reduced order lookup table is ready for implementation. The system is implemented onto the controller platform with the same position trajectory command.

Both fingers are linearized with the same nonlinear compensator and the tracking controller is implemented with a PID controller. The fingers are commanded to move from 20^o to 40^o, similar to the simulation. Figure 7.6 and Figure 7.7 show the actual trajectory responses for both fingers of the VR gripper.

Position responses shown in Figure 7.6(a) and Figure 7.7(a) for both left and right finger show similar result as the simulation predicted with no significant steady state error is found when the profile finishes. However, the tracking error results are worse than what the simulation expected. In Figure 7.6(b) and Figure 7.7(b), the maximum tracking error for the left and right finger are 1.2^o and 2.5^o respectively. Figure 7.6(c) and Figure 7.7(c) show the trajectory current responses for left and right fingers of the VR gripper respectively. The waveforms show similar trends as the simulation. Similar to the position response, some discrepancies are found. These discrepancies from the simulation can be explained by the absence of frictional effect and core loss from the simulation model.

Moreover, the reduced order lookup table is setup with evenly spaced current levels and angular positions. As a result, the incremental level for the variables might be fine enough for most of the regions, however, when the stator and rotor poles begin to overlap, significant flux-linkage saturation can be found as the flux-linkage and torque exhibit sudden changes, a separate lookup table with finer data points would be able to reduce the interpolation error. The main source of torque compensation error is contributed by the interpolation with a maximum compensation error of 7%.

Although the reduced order lookup table compensator successfully linearized the

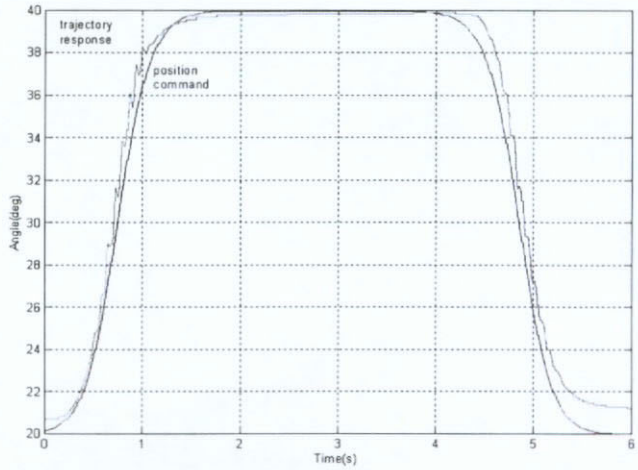

(a) position

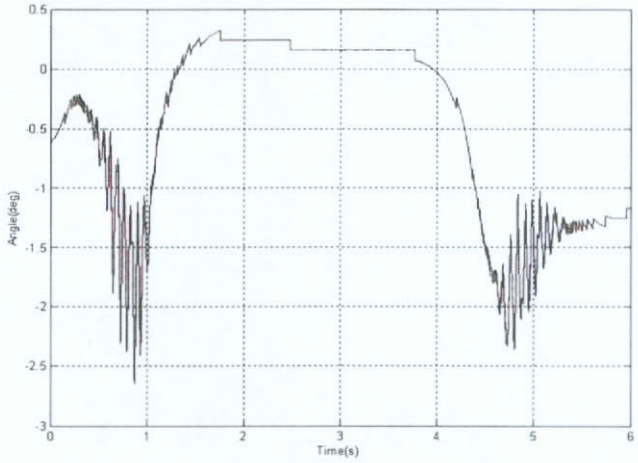

(b) error

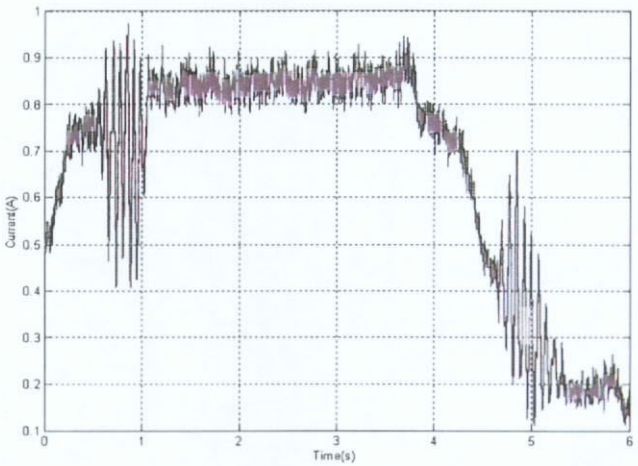

(c) current

Figure 7.6: Trajectory experimental responses of the right finger of the VR gripper with reduced order lookup table compensator

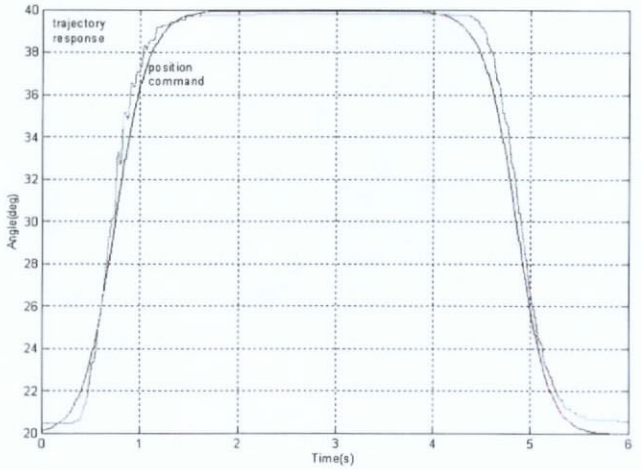

(a) position

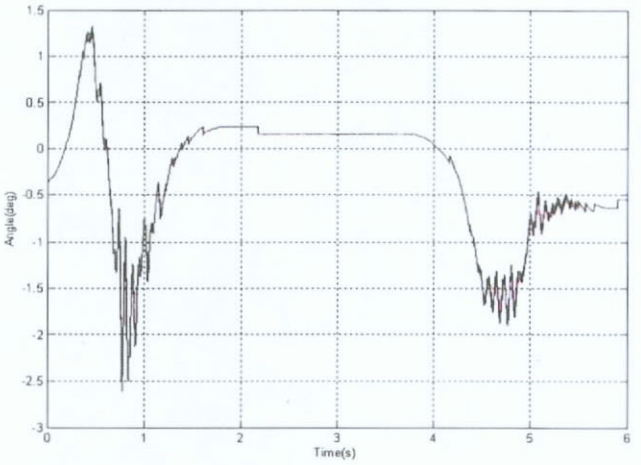

(b) error

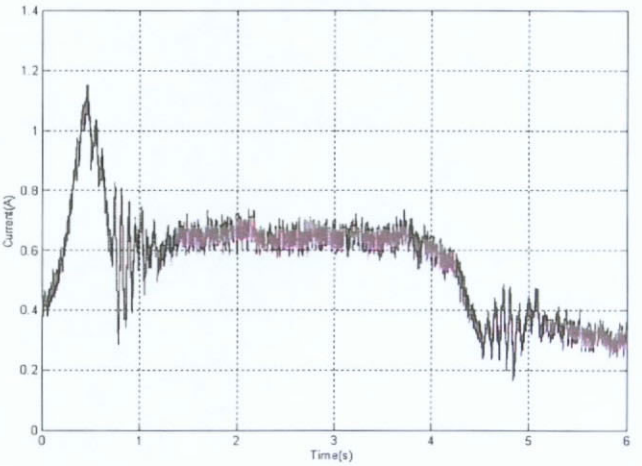

(c) current

Figure 7.7: Trajectory experimental responses of the left finger of the VR gripper with reduced order lookup table compensator

two-finger VR gripper and the performance result is suitable for most of the general applications, there is still room for control performance improvement. A more efficient nonlinear control algorithm is necessary for high-precision application.

7.6 Summary

In this chapter, a straightforward and low-cost position control solution is proposed for the two-finger VR gripper. Various general control methods were reviewed. The proposed position controller is mainly made up of a reduced order lookup table compensator and a classical PID controller block. With the implementation of the reduced order lookup table compensator, the two-finger VR gripper can be considered as a pseudo-linear device, therefore, a classical linear controller can be used for the trajectory controller. Simulation results show that the proposed method is stable and offer good tracking result. However, the implementation results show that the proposed method with the use of interpolation method, inherits a maximum compensation error of 7%. This would be a suitable for most of the general applications, however, a controller with higher performance is required for application with stringent requirement.

Chapter 8

Flux-linkage control with passivity-based control

For any controller design, system stability and global convergence are some of the prime objectives that a controller must guarantee. In chapter 7, the nonlinear compensation is achieved with a reduced order lookup table. Without an accurate mathematical description, it is difficult to ensure the stability, robustness and disturbance rejection capability. As a result, an advanced and efficient nonlinear controller needs to be introduced.

In this chapter, a novel controller design methodology, Passivity-based Control (PBC) is introduced. A PBC controller bases on transformation of energy as the controller design method. It guarantees global asymptotic convergence and stability. Besides, the PBC inherits certain system robustness with respect to modeling errors and parameter variations.

Section 8.1 and section 8.2 introduces the concept PBC and proves the system passivity for the two-finger VR gripper. This follows by section 8.3 which provides the Port-controlled Hamiltonian (PCH) modeling for the two-finger VR gripper. Section 8.4 and section 8.5 describe the detailed PBC flux-linkage regulator design and its simulation. After that, the PBC nonlinear controller is implemented and experimental results

are shown in section 8.6. The results confirmed that the proposed PBC can be an effective solution for the control of the two-finger VR gripper. Section 8.7 describes how the trajectory control of the two-finger VR gripper can be achieved. Simulation and experimental results are provided to demonstrate its tracking performance and stability. Results show that the PBC controller is more favorable, robust and stable under all conditions.

8.1 Improving system robustness through PBC

Although the method mentioned in section 7.2 is straightforward and easy to comprehend, it introduces extra error into the system due to interpolation. Moreover, lacking of a mathematical description of the motor, the close loop system fails to provide any stability proof and disturbance rejection.

Modern intelligent control strategies like fuzzy logic and neural network are also employed in VR motors [59, 62, 63]. They can deal with the nonlinearity problem and have adaptive capability for torque ripple minimization. These strategies do not require a full mathematical description of the target plant. However, some successful simulation and experiment examples using non-model based intelligent control methods are lacking in proofs on the control stability. They cannot guarantee global system stability, consistent performance and high-robustness at all operating conditions.

Passivity means the exchange of energy of the system with its environment. From a different perspective, the energy interpretation of passivity can be related to system stability. In passive systems the rate at which energy flows into the system is not less than the increase in storage. In other words, for a passive system can never store more energy than it is supplied [56].

PBC is a controller design approach which makes use of *energy-shaping*. PBC yields a closed-loop energy that is equal to the difference between the stored and the supplied

energies, namely energy-balancing [41]. While designing a PBC controller, a desired energy function is first selected. Then the controller would be designed to ensure this objective. This energy-balancing property is clearly an universal property of passive physical systems, including nonlinear and time-varying ones. With presence of dissipation, energy of the system is clearly non-increasing, thus the rate of convergence of the energy function can be increased by increasing the system damping through control effort, namely *damping injection*. The attractive features of this approach are the enhanced robustness and the lack of controller calculation singularities. These properties are based on the fact that cancellation of system nonlinear terms is avoided through PBC.

In recent years, PBC strategy has been adopted by power electronics researchers to solve various problems ranging from power converters, power factor compensators and electric motor control [1, 24, 54].

In this chapter, a PBC strategy is adopted and a nonlinear flux regulator of the two-finger VR gripper is developed in replace of the reduced order lookup table compensator. The two-finger VR gripper model is presented in the PCH model which encompasses a very large class of physical nonlinear systems. It provides a classification of the variables and the equations into those associated to the phenomenological properties and those defining the interconnection structure related with the exchanges of energy. Therefore, they are well-suited to carry out the basic steps of PBC of modifying the energy function and damping injection. The PBC is designed by reshaping the system's natural energy and injecting the required damping to achieve the control objective [55]. The proposed control scheme guarantees the global asymptotic stability and system robustness with response to some plant variations and modeling uncertainties.

8.2 System passivity

The two-finger VR gripper being an electromagnetic actuator, its proof of passivity is similar to traditional electric machines described in [56]. It can be decomposed into an

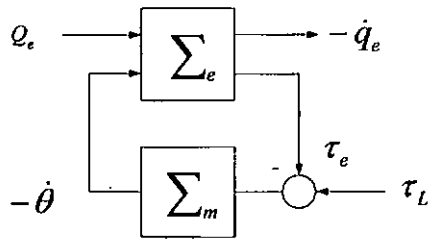

Figure 8.1: Feedback decomposition of an Euler-Lagrange system

electrical and a mechanical subsystem. The Lagrangian, L can be represented as:

$$L(q,\dot{q}) = L_e(q_e,\dot{q}_e,\theta) + L_{mec}(\theta,\dot{\theta}) \tag{8.1}$$

The VR finger gripper can then be represented as the negative feedback interconnection of two passive subsystems as shown in Figure 8.1.

$$\sum_e : \begin{bmatrix} Q_e \\ -\dot{\theta} \end{bmatrix} \rightarrow \begin{bmatrix} \dot{q}_e \\ \tau_e \end{bmatrix} \tag{8.2}$$

$$\sum_m : \tau_L - \tau_e \rightarrow -\dot{\theta} \tag{8.3}$$

where $\tau_e = \frac{L_e}{\theta}(q_e,\dot{q}_e,\theta)$ serves as the subsystems coupling signal and Q_e as the external force for the electrical subsystem. $\dot{q}_e$ and θ represent current and rotor position. Noticing that, the derivative of the Lagrangian of the electrical subsystem can be expanded as:

$$\dot{L}_e = \frac{\partial L_e}{\partial q_e}\dot{q}_e + \frac{\partial L_e}{\partial \dot{q}_e}\ddot{q}_e + \frac{L_e}{\theta}\dot{\theta} \tag{8.4}$$

By product rule, Equation 8.4 can be rearranged as:

$$\frac{d}{dt}\left[\frac{L_e}{\partial \dot{q}_e}\dot{q}_e\right] - \dot{L}_e = \left[\frac{d}{dt}\frac{\partial L_e}{\partial \dot{q}_e} - \frac{L_e}{q_e}\right]\dot{q}_e - \tau_e\dot{\theta} \tag{8.5}$$

Define energy function as

$$H_e = \frac{\partial L_e}{\partial \dot{q}_e}\dot{q}_e - L_e \tag{8.6}$$

Substitute $\frac{d}{dt}\left(\frac{\partial L_e}{\partial \dot{q}_e}\right) - \frac{L_e}{q_e} = Q_e$ into Equation 8.4 becomes

$$\dot{H}_e = Q_e \dot{q}_e - \tau_e \dot{\theta} \tag{8.7}$$

Since $Q = Mu - \frac{\partial F}{\partial \dot{q}} \dot{q}$, then

$$H_e + \frac{\partial F}{\partial \dot{q}_e} \dot{q}_e + \tau_e \dot{\theta} = M u \dot{q}_e \tag{8.8}$$

By integrating above result from 0 to T, it clearly illustrates that the supplied energy is larger than the storage energy. Consequently, this proves that the electrical subsystem is passive. Similarly, the mechanical subsystem can also be proved passive by considering the time derivative of the co-energy given by $\dot{H}_m = -\dot{\theta}(\tau_L - \tau_e)$. Again time integration of the above expression completes the proof. Conclusively, the two-finger VR gripper is a passive system and PBC strategy can be implemented onto it.

8.3 PBC and PCH

The electrical characteristic of the two-finger VR gripper can be rewritten as below:

$$u = R_m i + \dot{\lambda} \tag{8.9}$$

$$L_s \dot{i} = u - \left[R_m i + L_l \dot{i} + \left(\frac{\partial \lambda_s}{\partial \theta} + \frac{\partial \lambda_l}{\partial \theta} \right) \dot{\theta} \right] \tag{8.10}$$

where L_s and L_l are self and leakage inductance. u is the input voltage across stator winding and R_m is the stator winding resistance.

If the magnetic circuit is pseudo-linear, the inductance profile may be described by using the first two terms of the Fourier series approximation [51, 71].

$$L_s(\theta) = L_0 + L_1 \cos(\theta) \tag{8.11}$$

On the mechanical side, it is worth-mentioning that for a finger gripper, there is stroke limit and thus prevents the rotors from achieving extremely high speed. In other words, the

current loop response is much faster than the mechanical one. As a result, by combining Equation 3.21 and Equation 3.20, the torque production can be approximated as:

$$T_m \approx i\frac{\partial\lambda(\theta,i)}{\partial d\theta} \tag{8.12}$$

Therefore, the mechanical dynamic equation can be rewritten as:

$$J_m\ddot{\theta} = -K_{sp}\theta - K_v\dot{\theta} + i\frac{\partial\lambda_s}{\partial\theta} - T_L \tag{8.13}$$

The state vector, x is chosen as $x = [L_s i \quad K_{sp}\theta \quad J_m\dot{\theta}]^T$:

$$H(x) = \frac{1}{2}\left(L_s i^2 + K_{sp}\theta^2 + J_m\dot{\theta}^2\right) \tag{8.14}$$

With this energy function, the model of the two-finger VR gripper stated in Equation 8.10 and Equation 8.13 can be rearranged as the formula of PCH [56]:

$$\dot{x} = [J(x) - R]\frac{\partial H(x)}{\partial x} + gu + \zeta \tag{8.15}$$

where J is a skew symmetric matrix, R is a positive definite matrix, g is the input voltage vector and ζ is the disturbance vector. R represents the dissipative elements and it must be positively defined. Otherwise the energy stored within the system will not be less than the energy supplied into the system. Under this situation, the system will not be a passivity system. Using Equation 8.10 and Equation 8.13 and the selected state vector, x, dynamic model in PCH format can be represented as:

$$\dot{x} = \left\{ \begin{bmatrix} 0 & 0 & -\frac{\partial \lambda_s}{\partial \theta} \\ 0 & 0 & K_{sp} \\ \frac{\partial \lambda_s}{\partial \theta} & -K_{sp} & 0 \end{bmatrix} - \begin{bmatrix} R_m & 0 & 0 \\ 0 & K & 0 \\ 0 & 0 & K_v \end{bmatrix} \right\} D^{-1}x + \begin{bmatrix} 1 \\ 0 \\ 0 \end{bmatrix} u + \begin{bmatrix} -L_l\dot{i} - \frac{\partial \lambda_l}{\partial \theta}\dot{\theta} \\ \frac{K}{K_{sp}}x_2 \\ -T_L \end{bmatrix} \tag{8.16}$$

where

$$D^{-1} = \begin{bmatrix} \frac{1}{L_s} & 0 & 0 \\ 0 & \frac{1}{K_{sp}} & 0 \\ 0 & 0 & \frac{1}{J_m} \end{bmatrix}$$

In this context, K is a positive number and it is artificially inserted into the equation to maintain the positive definiteness of R. However, with the natural dissipative elements of the actual plant, the system damping will be small and it will reduce the close loop system performance. Additional damping injection is required. It can be realized by inserting an additional constant, K' into the dissipative matrix, R, as shown in Equation 8.17.

$$\dot{x} = \left\{ \begin{bmatrix} 0 & 0 & -\frac{\partial \lambda_s}{\partial \theta} \\ 0 & 0 & K_{sp} \\ \frac{\partial \lambda_s}{\partial \theta} & -K_{sp} & 0 \end{bmatrix} - \begin{bmatrix} R_m & 0 & 0 \\ 0 & K & 0 \\ 0 & 0 & K_v + K' \end{bmatrix} \right\} D^{-1}x + \begin{bmatrix} 1 \\ 0 \\ 0 \end{bmatrix} u + \begin{bmatrix} -L_l\dot{i} - \frac{\partial \lambda_l}{\partial \theta}\dot{\theta} \\ \frac{K}{K_{sp}}x_2 \\ \frac{K'}{J_m}x_3 - T_L \end{bmatrix} \tag{8.17}$$

8.4 PBC design

In this section, a PBC flux regulator is designed which attempts to handle the nonlinearity within the two-finger VR gripper [31]. The state error can be defined as: $e = x - x_d$. x_d is the reference state vector, which defines the desired system performance. Substituting $e = x - x_d$ into Equation 8.10, the model of the state error becomes:

$$\dot{e} + [R - J]D^{-1}e = \Phi \tag{8.18}$$

where $\Phi = -\dot{x}_d + [J - R]D^{-1}x_d + gu + \zeta$. According to Lyapunov stability [29], the scalar function $V(x)$ representing the system energy must process the following properties:

1. $V(0) = 0$;
2. $V(x) > 0$, $\|x\| \neq 0$;
3. V is continuous and has continuous derivatives *w.r.t.* all components of x;
4. $\dot{V(x)} \leq 0$ along trajectories of the equation.

This control problem is defined as a trajectory problem. The system energy function, $V(x)$ can be defined as:

$$V = \frac{1}{2} e^T D^{-1} e \tag{8.19}$$

where e represents trajectory error.

$$\begin{aligned} \dot{V} &= e^T D^{-1} \dot{e} \\ &= e^T D^{-1} [(J - R) D^{-1} e + \Phi] \\ &= e^T D^{-1} J D^{-1} e - e^T D^{-1} R D^{-1} e + e^T D^{-1} \Phi \end{aligned} \tag{8.20}$$

where

$$JD^{-1} = \begin{bmatrix} 0 & 0 & -\frac{1}{J_m}\frac{\partial \lambda_s}{\partial \theta} \\ 0 & 0 & \frac{K_{sp}}{J_m} \\ \frac{1}{L_s}\frac{\partial \lambda_s}{\partial \theta} & -1 & 0 \end{bmatrix} \qquad RD^{-1} = \begin{bmatrix} \frac{R_m}{L_s} & 0 & 0 \\ 0 & \frac{K}{K_{sp}} & 0 \\ 0 & 0 & \frac{K_v + K'}{J_m} \end{bmatrix} \tag{8.21}$$

From Equation 8.20, $e^T D^{-1} J D^{-1} e$, the first term, consists of a matrix J which is skew-symmetric and clearly becomes zero. It imposes no action on stability and is named as workless force. The second term, $-e^T D^{-1} R D^{-1} e$, has matrix R and D^{-1} which are both positive definite and make the entire term negative. In order to maintain the system stability in the sense of Lyapunov, Φ needs to be zero through suitable control effort which yields $\dot{V} = -e^T D^{-1} R D^{-1} e$. The state error system is asymptotically stable. Furthermore, the state error converges exponentially, i.e. $\|e\| < k_0 e^{-\mu_0} \|e(0)\|$, where k_0 and μ_0 are positive scalars. Besides Equation 8.18 shows that, for tracking problem, $\dot{e} = e = 0$ and $\Phi = 0$ is a correct choice. Furthermore, system stability can still be preserved to some extent despite of the presence of certain parameters variations. It is because parameter variations in λ introduced through un-modeled hysteresis effect, assumed pseudo linear flux-linkage characteristics and modeling error of K_{sp}, still maintain the skew-symmetric property in matrix J. Similarly, variations in R_m and K_v,

do not influence the positive definiteness of matrix R. Such property ensures the system can automatically preserve certain robustness.

Expanding Equation 8.20 with $\Phi = 0$, three differential equations can be obtained:

$$-\dot{x}_{d1} - \frac{1}{J_m}\frac{\partial \lambda_s}{\partial \theta}x_{d3} - \frac{R_m}{L_s}x_{d1} + u - L_l\dot{i} - \frac{\partial \lambda_l}{\partial \theta}\dot{\theta} = 0 \tag{8.22}$$

$$-\dot{x}_{d2} + \frac{1}{J_m}K_{sp}x_{d3} - \frac{K}{K_{sp}}x_{d2} + \frac{K}{K_{sp}}x_2 = 0 \tag{8.23}$$

$$-\dot{x}_{d3} + \frac{1}{L_s}\frac{\partial \lambda_s}{\partial \theta}x_{d1} - x_{d2} - \frac{K_v + K'}{J_m}x_{d3} + \frac{K'}{J_m}x_3 - T_L = 0 \tag{8.24}$$

Rearranging Equation 8.23 in terms of x_{d2}, it becomes:

$$x_{d3} = \frac{J_m}{K_{sp}}\left(\dot{x}_{d2} + \frac{K}{K_{sp}}x_{d2} - \frac{K}{K_{sp}}x_2\right) \tag{8.25}$$

By substituting Equation 8.23 into Equation 8.24, Equation 8.24 becomes a second order differential equation,

$$\begin{aligned}&\ddot{x}_{d2} + \left[\frac{K}{K_{sp}} + \frac{(K_v + K')}{J_m}\right]\dot{x}_{d2} + \left[\frac{K_{sp}}{J_m} + \frac{(K_v + K')}{J_m}\frac{K}{K_{sp}}\right]x_{d2} \\ =&\frac{K_{sp}}{J_m}\frac{i}{L_s}\frac{\partial L_s}{\partial \theta}x_{d1} + \frac{(K_v + K')}{J_m}\frac{K}{K_{sp}}x_2 + \left(\frac{K}{J_m} + \frac{K_{sp}K'}{J_m^2}\right)x_3 - \frac{K_{sp}}{J_m}T_L\end{aligned} \tag{8.26}$$

As a result, valid sets of K and K' can be determined by equating the coefficients of a general second order differential equation, i.e.

$$\frac{K}{K_{sp}} + \frac{(K_v + K')}{J_m} = 2\zeta\omega_n \tag{8.27}$$

$$\frac{K_{sp}}{J_m} + \frac{(K_v + K')}{J_m}\frac{K}{K_{sp}} = \omega_n^2 \tag{8.28}$$

Solving Equation 8.27 and Equation 8.28 with quadratic equations and select ζ and ω_n as 1 and $700 rads^{-1}$, K and K' can be calculated as $6 kgms^{-1}$ and $1 kgmsrad^{-1}$ respectively. Classically, it is common to choose ζ equals to 0.7. However, for the

two-finger VR gripper, to prevent the two-finger VR gripper from experiencing any mechanical overshoot and introducing a high impact force onto the target object, ζ equals to 1 is chosen. Similarly, ω_n is chosen in such a way that the controller would have a high close loop bandwidth while not exciting system resonance.

Note that change of current falls to zero at steady state and thus $\dot{x}_{d1} = 0$. The control law, Equation 8.22 becomes,

$$u = \frac{R_m}{L_s} x_{d1} + \frac{1}{J_m} \frac{\partial \lambda_s}{\partial \theta} x_{d3} + L_l \dot{i} + \frac{\partial \lambda_l}{\partial \theta} \dot{\theta} \tag{8.29}$$

System output damping can be further increased without altering the control law and affecting the stability. The alterations can be made at the command input, using the command shaping with equation below:

$$x'_{d1} = x_{d1} - K'' \dot{\theta} \tag{8.30}$$

After command shaping, x'_{d1} becomes system reference input, x_1 becomes flux-linkage estimated output. PBC controller takes x_{d3} as feedback which is obtained by solving Equation 8.25 and Equation 8.26 with current and angular velocity.

8.5 PBC Simulation

As the experiment will be implemented onto the controller system described in section 4.2, certain simulation settings need to be matched with the actual hardware to obtain an accurate simulation result. The simulation of the PBC controller was done using *MATLAB SIMULINK*. The controller needs to be, on one hand, fast in dynamics but on the other hand, robust enough to stay stable within the entire range of load variation. Slight oscillation can be amplified mechanically and exhibited onto the finger tip and deteriorate the entire system performance. Thus, a $5kHz$ sampling rate was selected. To solve the differential equations, an integration solver using Euler numerical method was employed. Same method was selected for the actual hardware implementation.

In the simulation, a step flux-linkage input of $15mWb$ with a period of one second and 80% duty cycle was injected into the simulation model. Figure 8.2 and Figure 8.3 show the simulation results for states responses and the corresponding tracking errors respectively. Results show that all states have fast tracking responses. Peak time of x_1 is $30ms$, and the mechanical tracking error for x_2 and x_3 settle within $200ms$. Simulation results show that the PBC controlled system is stable and offers fast tracking responses.

8.6 Experimental results

8.6.1 Responses of both fingers

To verify with the simulation results, experiment was carried out. Initially the two-finger VR gripper was at open positions. Then a step input flux-linkage command of $15mWb$ was injected into the PBC flux regulator. Figure 8.4 and Figure 8.7 show the experimental result for the two fingers of the VR gripper.

Results show that responses of both fingers are stable and show good tracking performances. For simplicity of the controller, only one set of model parameters was used for both fingers. From the results, it shows that despite of the presence of modeling error, the PBC controller still remains stable and robust. For x_1 states, it settles within $50ms$ and the mechanical states, x_2 and x_3 settle within $350ms$.

8.6.2 Responses with command shaping

From Figure 8.4 and Figure 8.6, results show that there are overshoots mainly at the x_2 which represents the position response dynamically. In order to reduce the mechanical overshoot, command shaping mentioned by Equation 8.30 can be used.

Figure 8.8 shows the response of the left finger with command shaping implemented. With command shaping, gain K'' selected as 0.001, the flux-linkage command is reshaped.

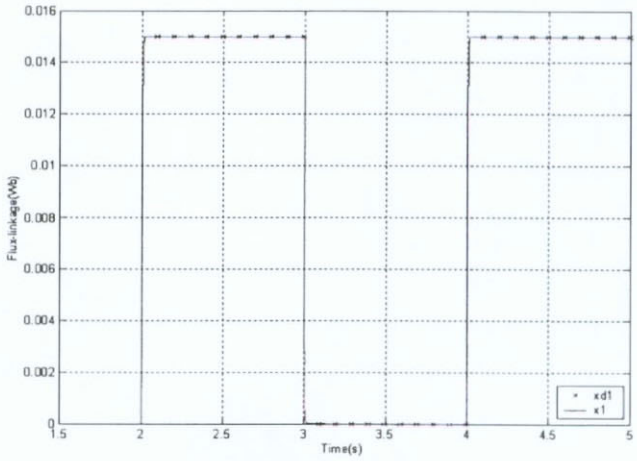

(a) x_1 tracking response

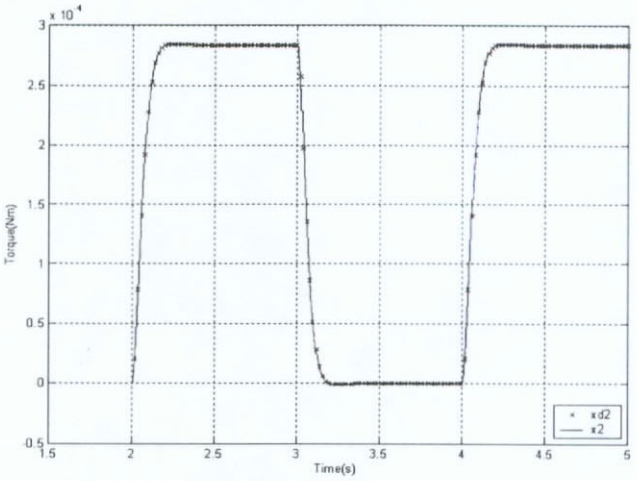

(b) x_2 tracking response

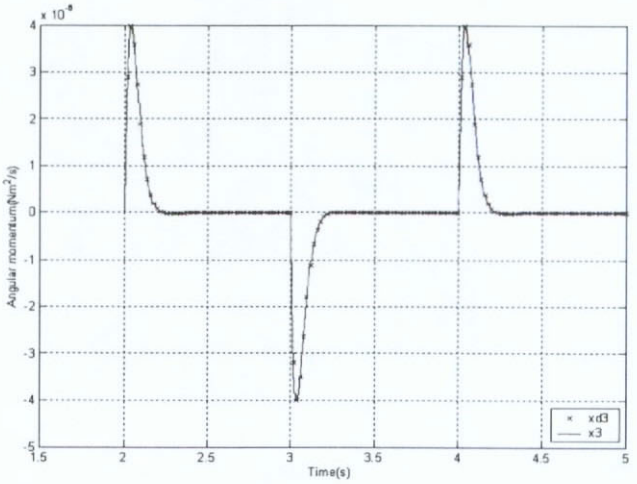

(c) x_3 tracking response

Figure 8.2: States simulation responses of the two-finger VR gripper

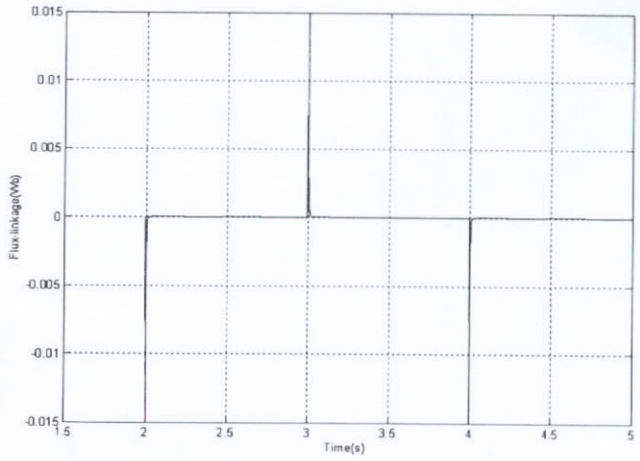

(a) x_1 tracking error

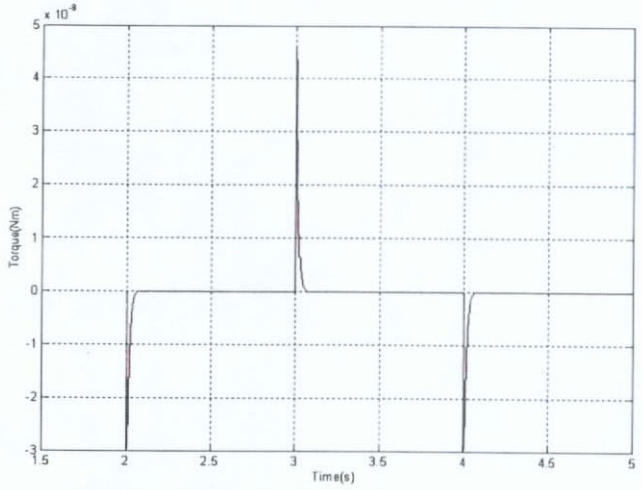

(b) x_2 tracking error

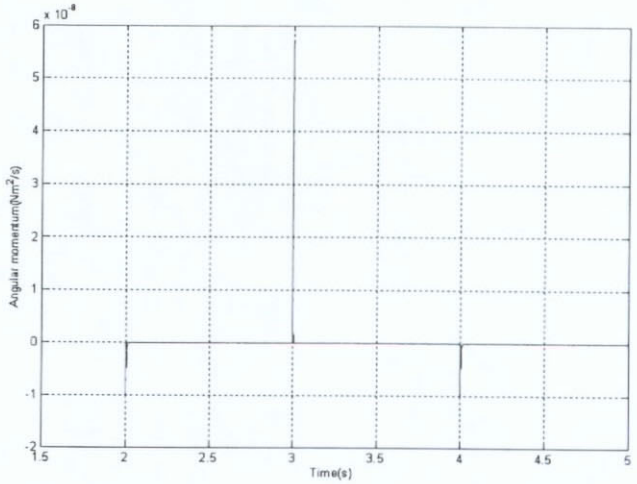

(c) x_3 tracking error

Figure 8.3: States error of the two-finger VR gripper

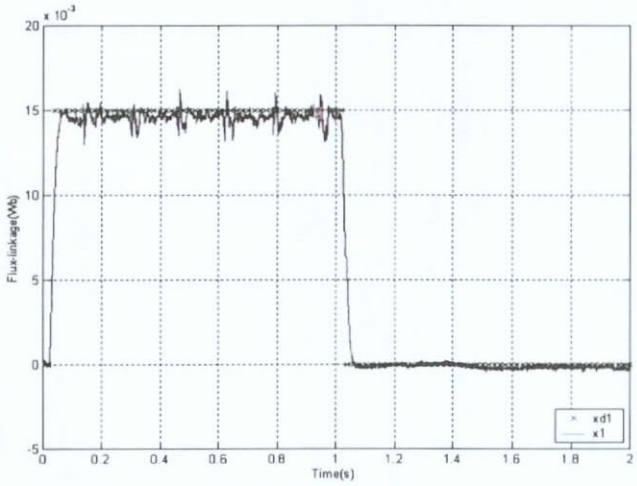

(a) x_1 tracking response

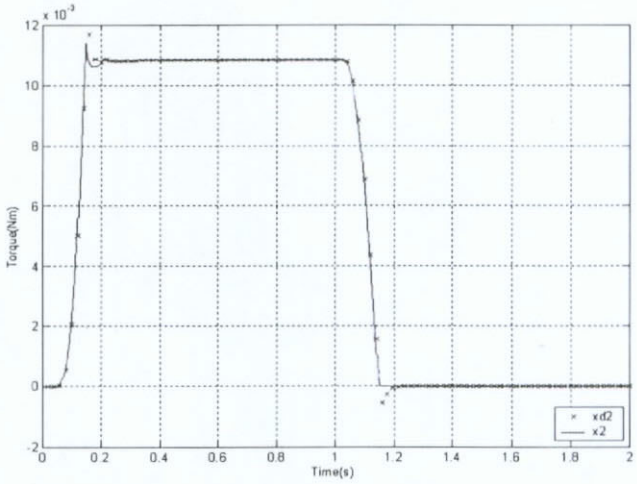

(b) x_2 tracking response

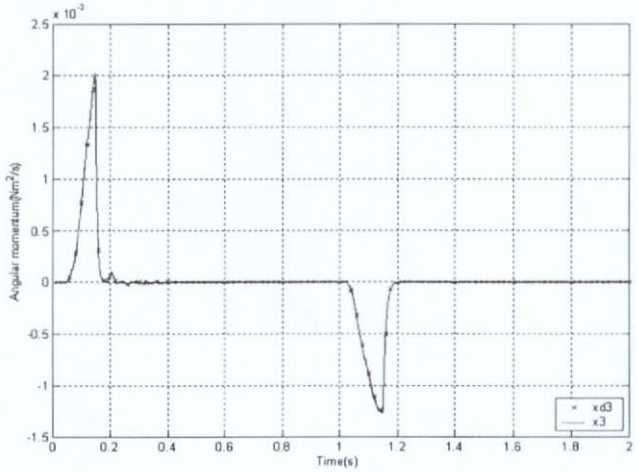

(c) x_3 tracking response

Figure 8.4: States experimental responses of the left finger

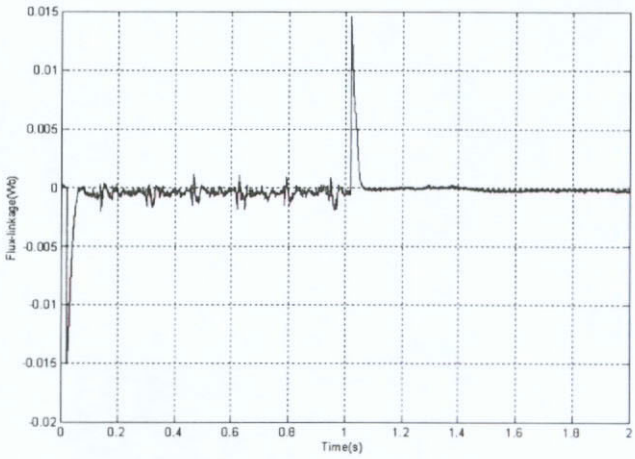

(a) x_1 tracking error

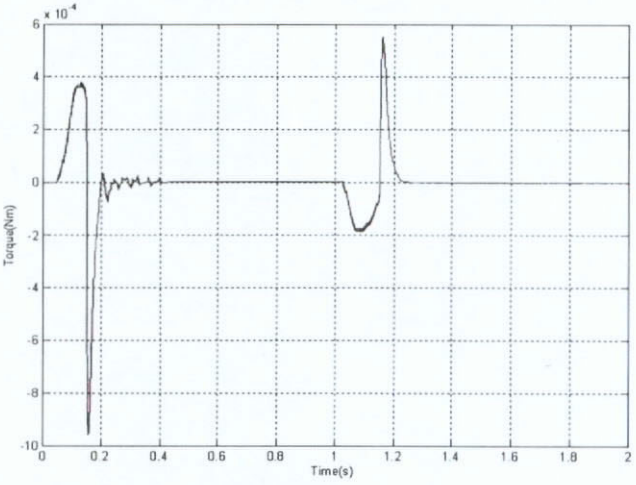

(b) x_2 tracking error

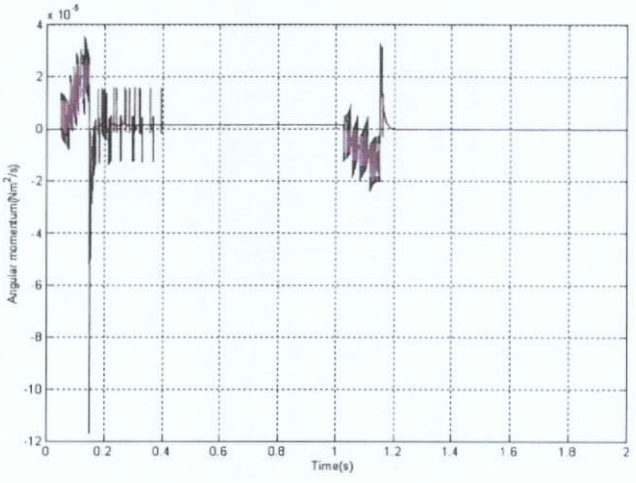

(c) x_3 tracking error

Figure 8.5: States error of the left finger

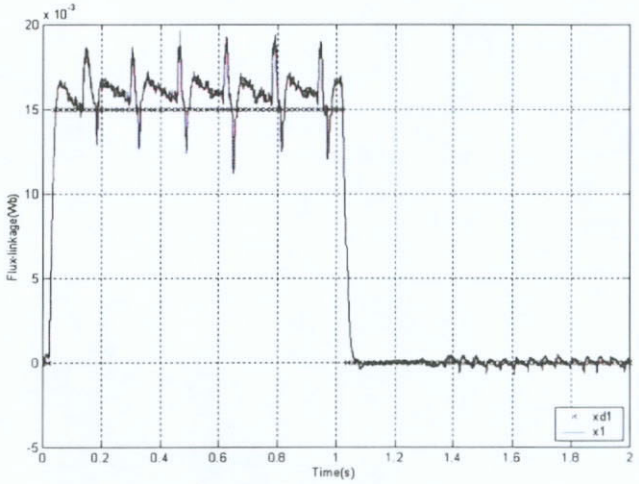

(a) x_1 tracking response

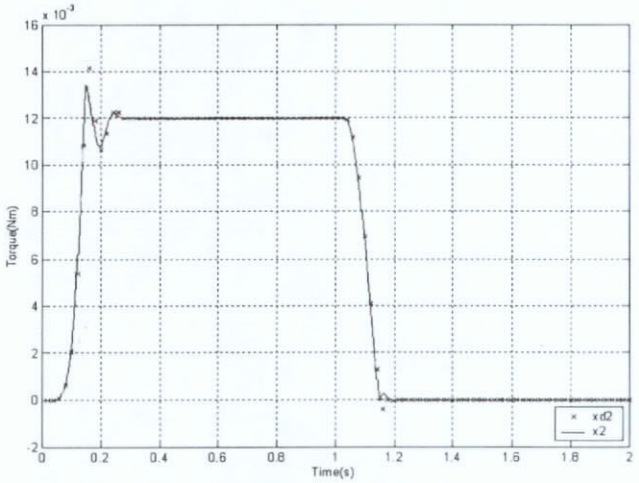

(b) x_2 tracking response

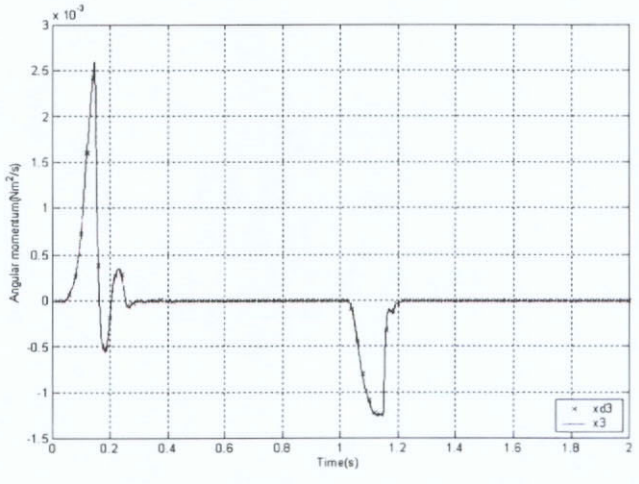

(c) x_3 tracking response

Figure 8.6: States experimental responses of the right finger

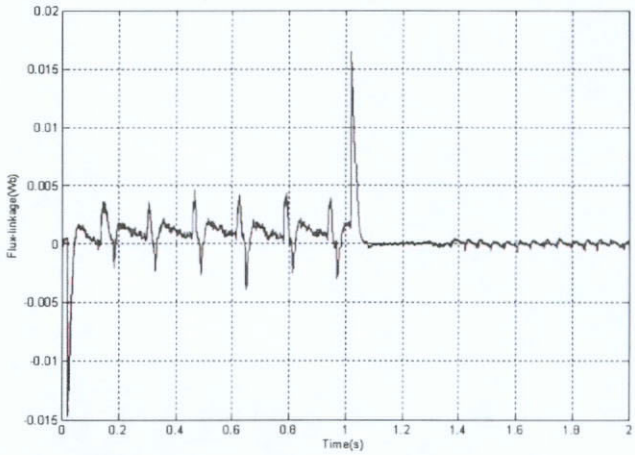

(a) x_1 tracking error

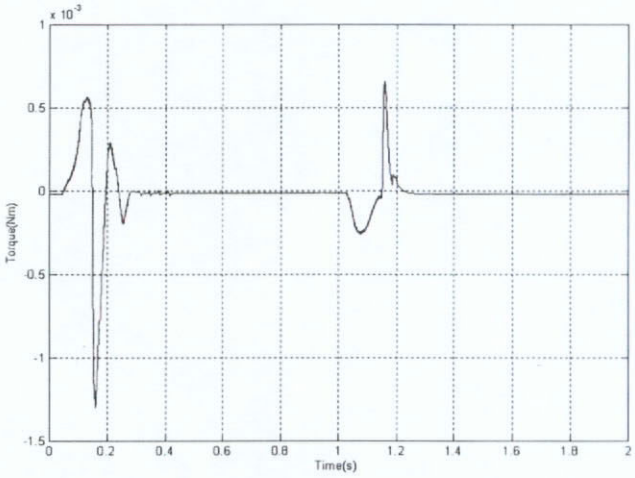

(b) x_2 tracking error

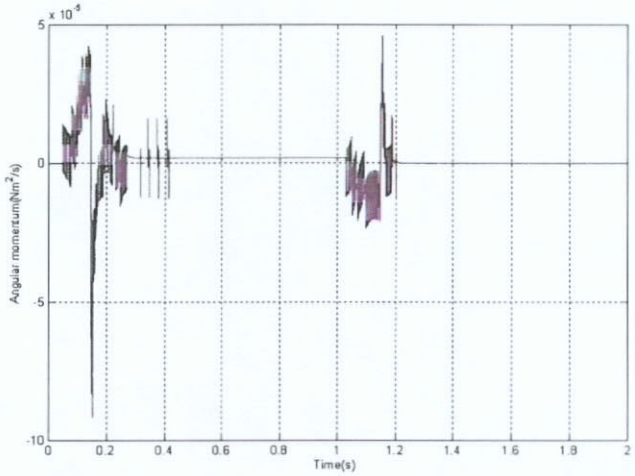

(c) x_3 tracking error

Figure 8.7: States error of the right finger

However, it benefits the tracking error for both x_2 and x_3 states by 50%. Besides, overshoot of x_2 is successfully suppressed.

8.6.3 Robustness evaluation

A good way of demonstrating the robustness of the PBC control algorithm implemented is to introduce parameter variation or modeling error into the system. One of the simplest way is to increase the spring constant. Figure 8.10 shows the states tracking responses with spring constant doubled.

As clearly shown from the experimental results, all states still remain stable and exhibit asymptotic convergence. With the spring constant doubled, the mechanical bandwidth is also increased with higher rigidity. System responses show higher frequency components and thus have smaller dynamic tracking error. With the same set of gains, system successfully remains stable.

8.7 Trajectory controller

With the implementation of the PBC flux-linkage regulator, the actuator can now be considered as a linear device and a simple PID be easily employed to control it effectively. The equivalent open loop transfer function can be described as:

$$G(s) = \frac{J_m}{J_m s^2 + K_v s + K_{sp}} \tag{8.31}$$

The trajectory controller gains can be obtained through a classical pole placement method. The derivative term should be large enough to provide a fast dynamic response, which brings along small amplitude oscillations at settling. A smaller derivative term was chosen to avoid unnecessary vibrations. A small integrative term is introduced once the profile ends. This prevents the integrative term from hindering the dynamic response while reduces the settling time and steady state error.

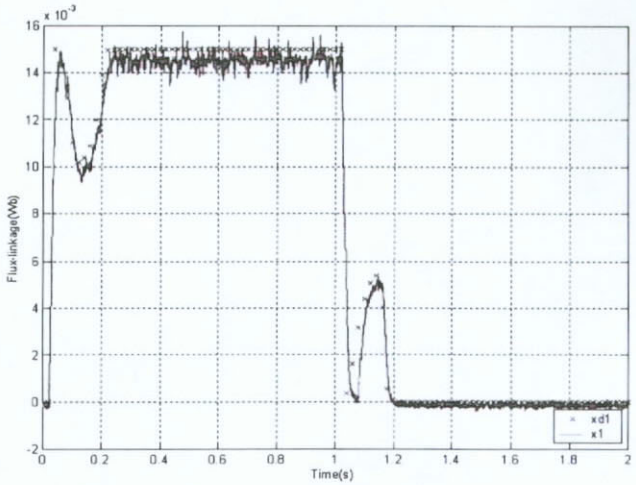

(a) x_1 tracking response

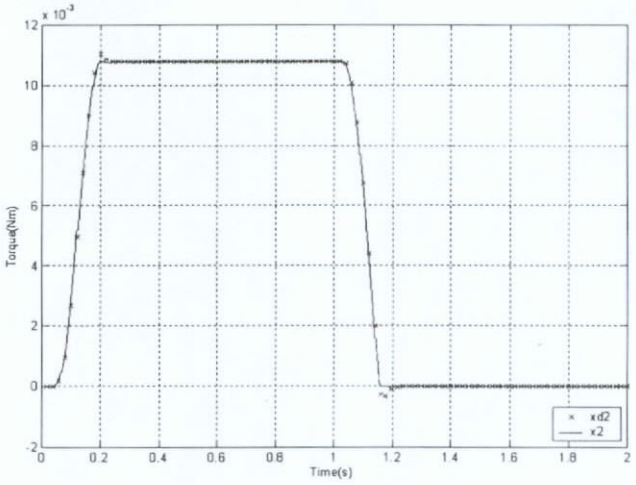

(b) x_2 tracking response

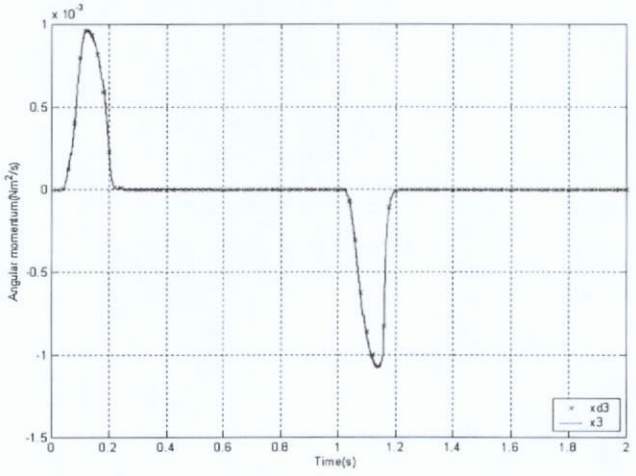

(c) x_3 tracking response

Figure 8.8: States experimental responses with command shaping of the left finger

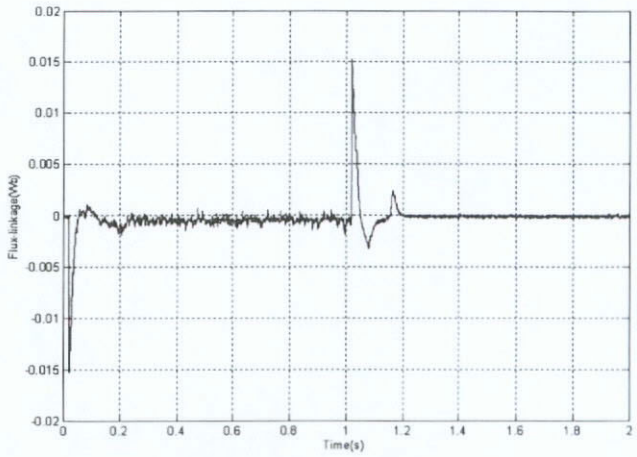

(a) x_1 tracking error

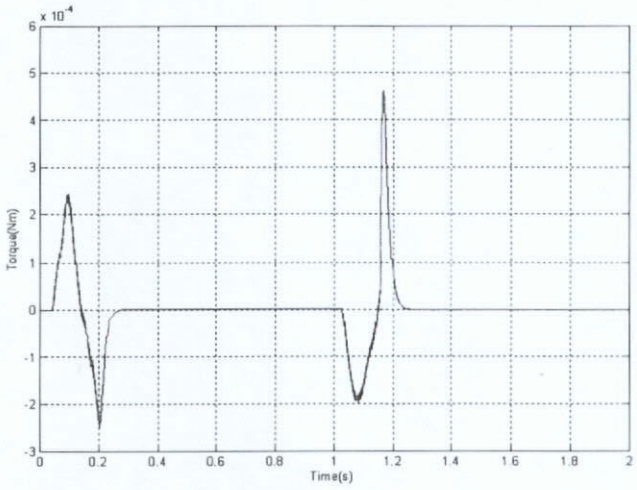

(b) x_2 tracking error

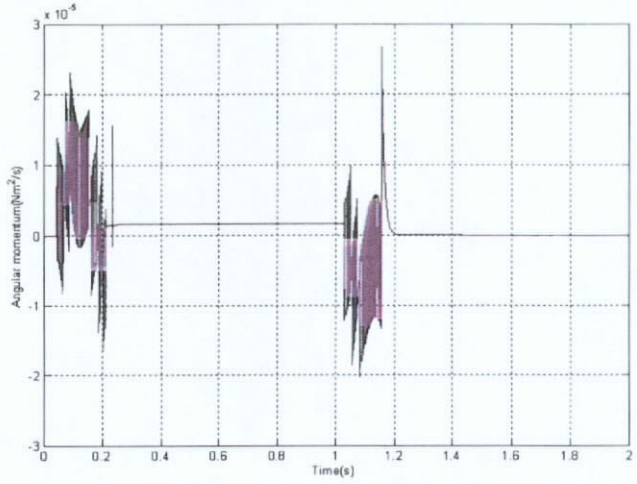

(c) x_3 tracking error

Figure 8.9: States error with command shaping of the left finger

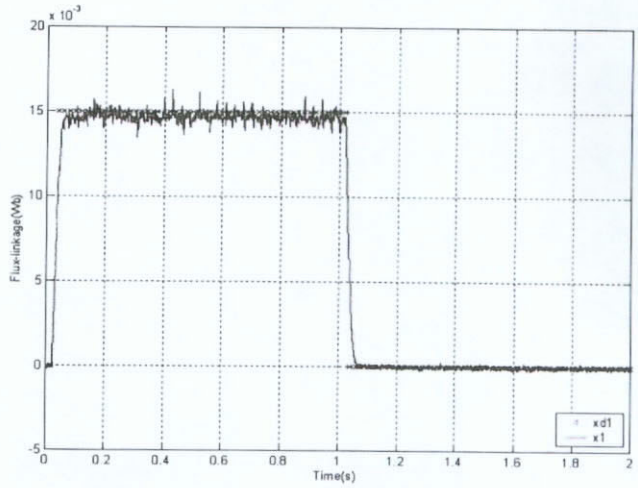

(a) x_1 tracking response

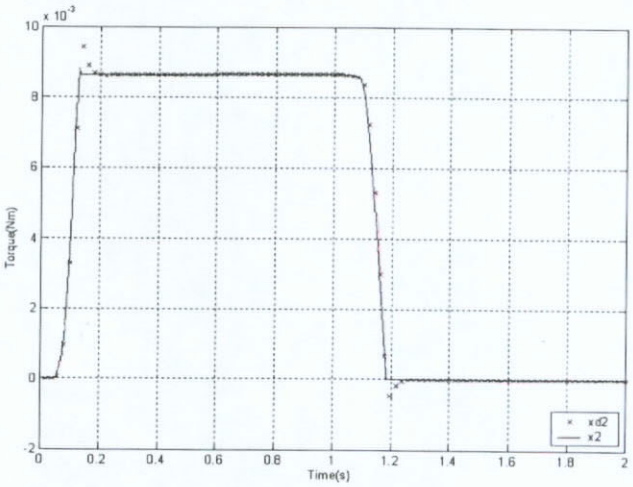

(b) x_2 tracking response

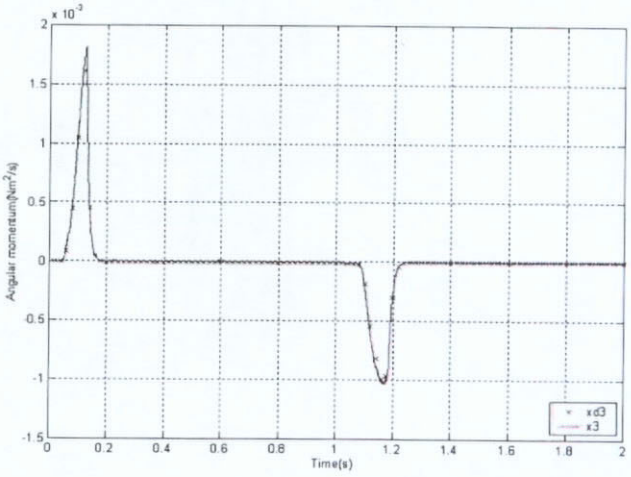

(c) x_3 tracking response

Figure 8.10: States experimental responses with spring constant doubled of the left finger

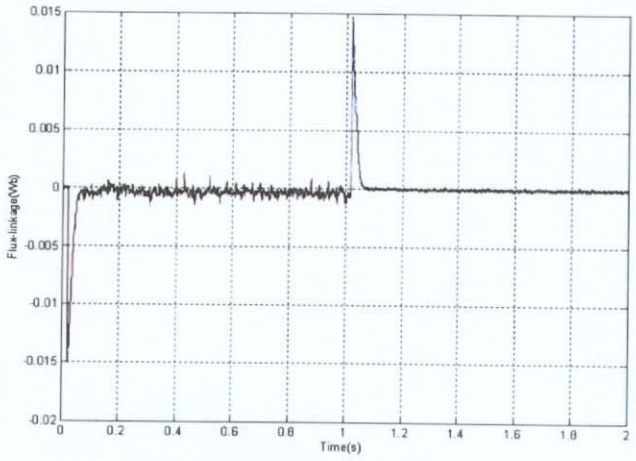

(a) x_1 tracking error

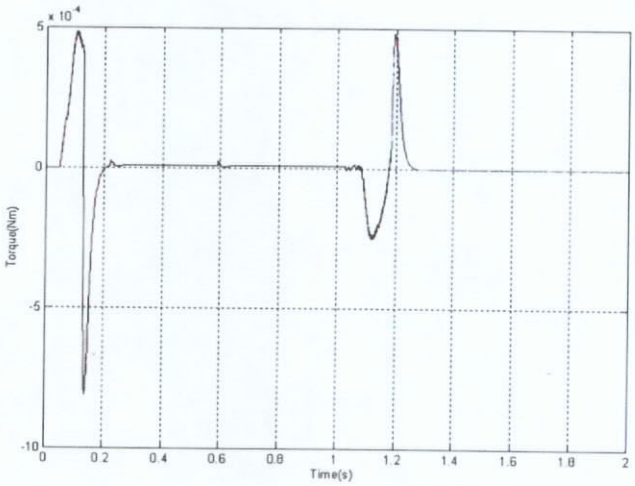

(b) x_2 tracking error

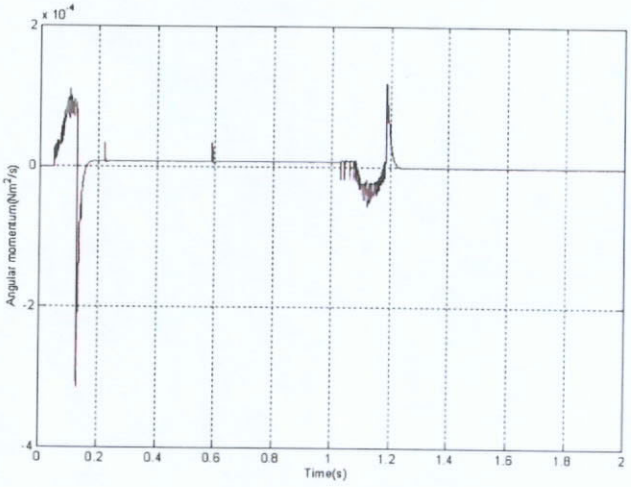

(c) x_3 tracking error

Figure 8.11: States error with spring constant doubled of the left finger

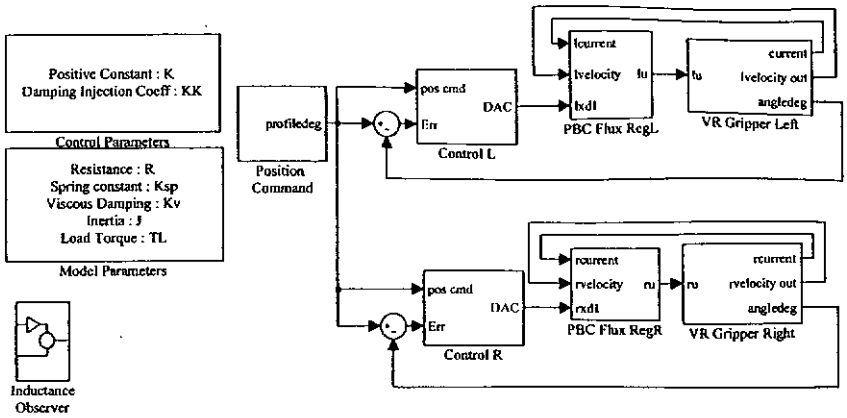

Figure 8.12: Simulation block diagram for trajectory control of two-finger VR gripper

8.7.1 Simulation

Figure 8.12 shows the simulation block diagram for trajectory control of the two-finger VR gripper. The PID controller, acts as the trajectory controller calculates the torque command with the error signal obtained. The nonlinear PBC compensator evaluates flux-linkage command with the torque command and thus position control can be achieved.

Figure 8.13 shows the simulation results with the proposed trajectory tracking method. As shown in the results, the gripper is stable and enjoys small dynamic and steady errors. Consequently, it is ready to be verified with experimental implementation.

8.7.2 Experimental results

Figure 8.14 and Figure 8.15 show the trajectory tracking experimental results of the two-finger VR gripper. Similar to the simulation results, the gripper is stable and show small dynamic and steady errors. Without frictional effects and other losses included into the simulation, slight discrepancy can be found when comparing simulation and actual trajectory tracking errors.

By comparing to the tracking performance with the reduced order lookup table implemented in Chapter 7, the PBC trajectory controller clearly shows a better performance. The PBC dynamic tracking error shown in Figure 8.14(b) and Figure 8.15(b)

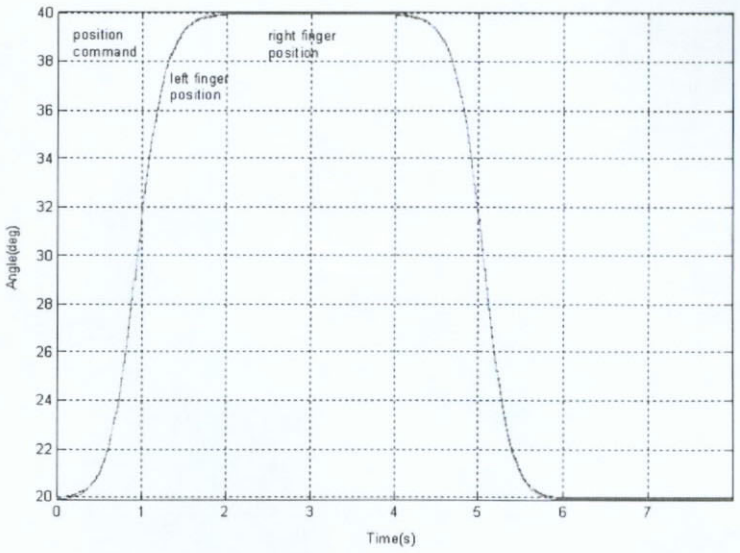

(a) angular position

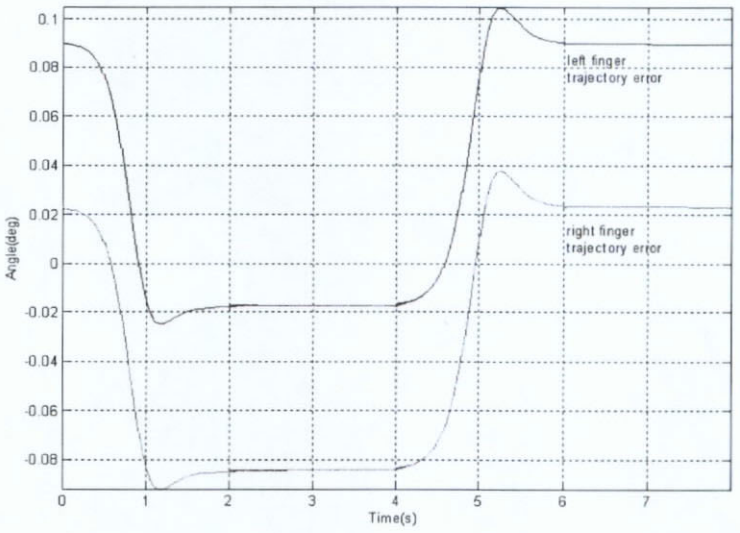

(b) tracking error

Figure 8.13: Trajectory tracking simulation results of the two-finger VR gripper

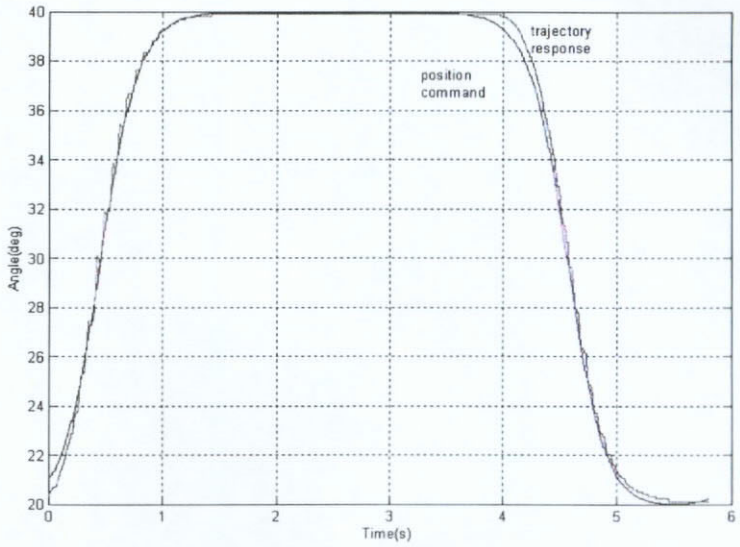

(a) angular position

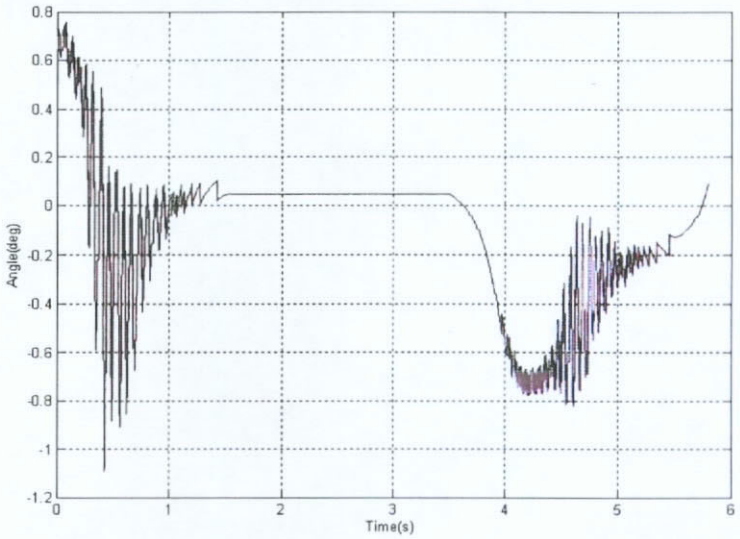

(b) tracking error

Figure 8.14: Trajectory tracking experimental results of the left finger

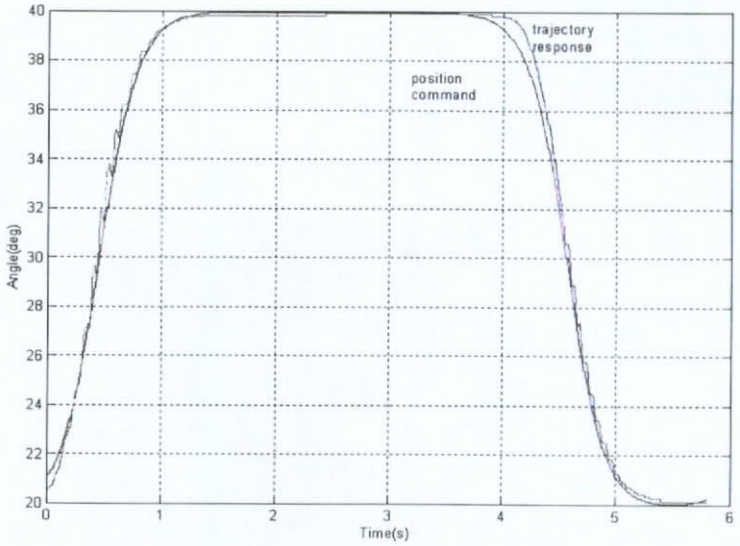

(a) angular position

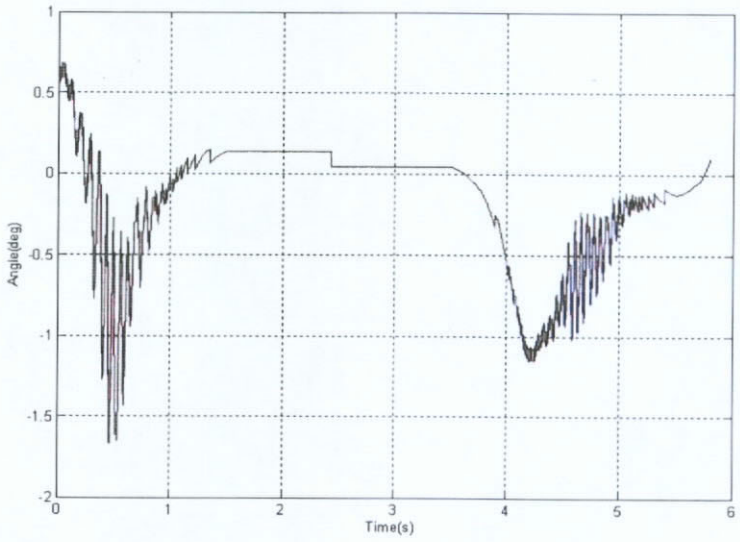

(b) tracking error

Figure 8.15: Trajectory tracking experimental results of the right finger

show a maximum of 0.7^o and a minimum of -1.5^o. Instead, the dynamic error of the reduced order lookup table shows maximum and minimum tracking error of 1.3^o and -2.5^o respectively. In addition, the PBC trajectory controller achieves a steady state error of 0.09^o which performs better than its counterpart.

8.8 Summary

This chapter describes the detail controller design, simulation and experimental implementation of PBC controllers for the flux regulation and trajectory control of the two-finger VR gripper. The reduced order lookup compensator is simple to implement and easy to comprehend. However, no system stability and convergence can be guaranteed. To overcome this, the PBC controller is also introduced. The controller can overcome the inherent nonlinear characteristics of the two-finger VR gripper and it guarantees global stability and asymptotical convergence of all state errors. It also avoids the cancellation of system nonlinear terms and enhances the overall system's robustness.

A comprehensive PCH model is constructed. By reshaping the system's natural energy and injecting the required damping, a nonlinear flux controller for the two-finger VR gripper is developed. Through computer simulation, the proposed control scheme guarantees the global asymptotic stability and system robustness with response to some plant variations and modeling uncertainties.

To confirm the effectiveness of the PBC controller, experimental implementation is carried out. When comparing with the simulation results, it is found that they match closely. The experimental results confirm that the proposed PBC controller can guarantee global stability, asymptotical convergence and robustness against changes of plant parameters. It also shows that the PBC controller has a better performance than the reduced order lookup table compensator in terms of trajectory performance and robustness.

Conclusively, all the results proof that the proposed PBC controller for the two-finger VR gripper is stable, robust and has high performance.

Chapter 9

High-precision grasping of delicate objects

In this chapter, a high-precision grasping algorithm for delicate objects, is proposed. The control algorithm bases on the development of the nonlinear PBC controller described in chapter 8. Position and force control can be achieved by means of selecting different mode of trajectory profile and by optimizing between speed and force precision under different conditions.

A mixed-mode control with command scheduling control algorithm is proposed and implemented in section 9.1 and section 9.2 respectively. The force response, current and angular position measurements are described in section 9.3. Results show that the project two-finger VR gripper is a suitable, robust and low-cost solution while offering high-precision grasping of delicate objects.

9.1 Mixed-mode control with command scheduling

To achieve high-speed grasping control of the two-finger VR gripper, a special position and force control strategy is required. The control strategy, on one hand, has to allow the VR finger gripper to operate at high-speed, and on the other hand, achieve a high-precision grasping force control. Making use of the nonlinear PBC controller implemented in

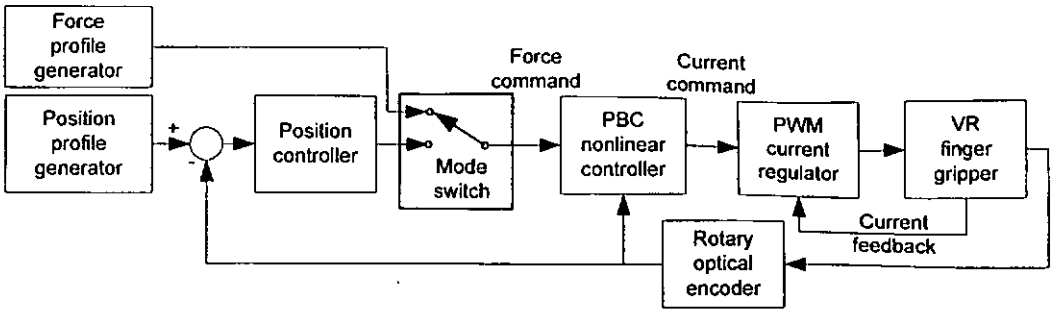

Figure 9.1: Mixed-mode control with command scheduling block diagram for the two-finger VR gripper

Chapter 8, a mixed-mode control with command scheduling is proposed.

Figure 9.1 shows the entire controller block diagram. It consists of a PBC nonlinear controller, a mixed-mode switch and a trajectory controller [10]. The entire controller block diagram can be separated into two different control modes, namely position mode and force mode.

9.1.1 Mixed-mode strategy

With the use of mixed-mode switch, different control modes can be implemented. When the two-finger VR gripper is under position control, the control block diagram is in fact equivalent to the trajectory control implemented in section 8.7.

For force control, the two-finger VR gripper torque and force relationship can be described as:

$$F_f \cong T_m \times K \tag{9.1}$$

where T_m, F_f and K are motor torque, force at the finger tip and a constant. Both trajectory and force control modes can share the same nonlinear compensator. Under such implementation, nonlinear controller design effort can be shared despite the change of control modes. As a result, when the two-finger VR gripper is under force control mode, position controller is by-passed and the nonlinear controller receives force command directly.

9.1.2 Command scheduling

To enable fast grasping of delicate object with minimal impact on the object, the VR gripper goes through a predetermined trajectory planning or command scheduling. The detailed flow chart is shown in Figure 9.2. The entire motion consists of six steps.

1. Initially, the control mode begins with the trajectory control mode and accepts torque command input from the trajectory controller. The finger gripper begins at its fully opened position, *home position* to a predefined location with high-speed point-to-point motion which is generated by the S-curve from Equation 7.2. This predefined location is named as the *search position.*

2. After that, it is followed by a low constant speed for object search until it hits the object. When the finger reaches its contact, *contact position* and once the force exceeds a predefined threshold, the controller registers the impact and changes the control mode switch from trajectory control mode to a force control mode.

3. The force profile ramps until the desired force level is achieved.

4. The gripping force holds for a certain time period, depending on the application requirement.

5. Then the force is relieved by applying current in opposite direction. Afterwards, the control mode switches back to the trajectory mode.

6. Trajectory control takes place again and the finger gripper returns to its initial *home position.*

The full trajectory profile for command scheduling is shown in Figure 9.3. The control mode begins with the trajectory control mode. From the waveform, it clearly shown that there is an S-curve trajectory profile for high-speed point-to-point motion. Afterwards, a linear motion profile is generated for contact searching purpose. Once the finger reaches its object, a constant force is applied to its object and no change in position can be

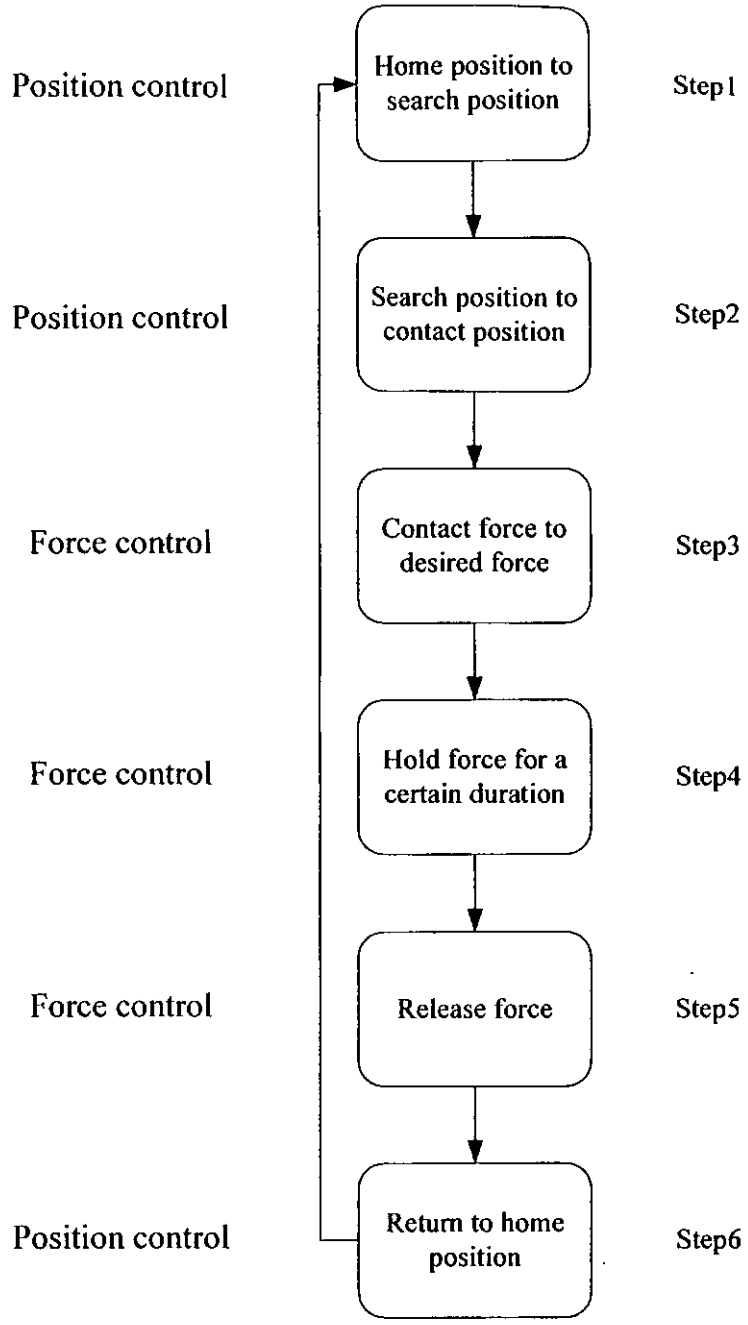

Figure 9.2: The full motion flow chart

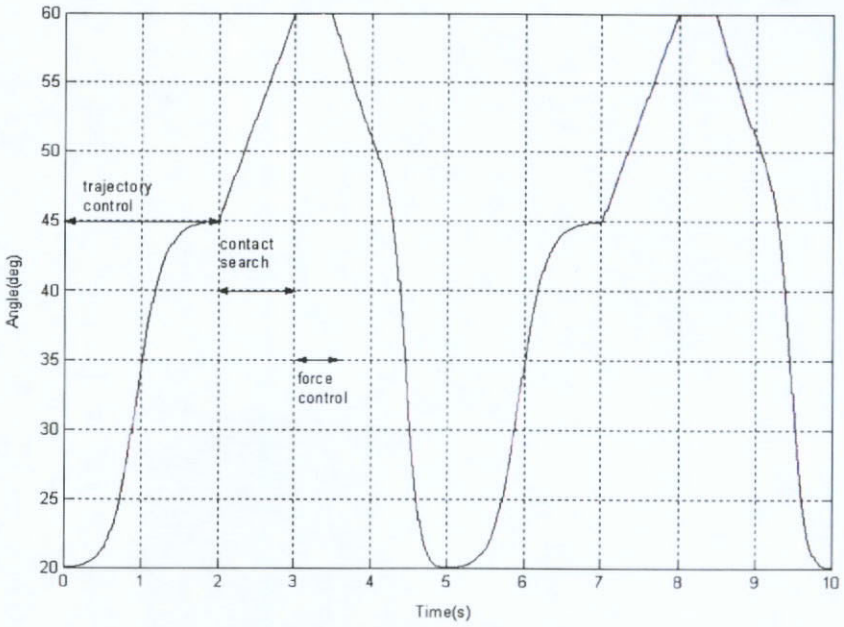

Figure 9.3: The full motion profile

found. Once force control is finished, the finger leaves the object and another S-curve is generated for returning back to its initial *home position.*

For simplicity, the S-curve motion profile can be removed and the finger gripper can close its fingers merely with a constant search speed. However, with a high search speed, the impact force, F_{imp}, on the object would also be increased. This is because impact force can be represented by Equation 9.2.

$$F_{imp} = \frac{m\Delta v}{\Delta t} \tag{9.2}$$

where m, v and t represent the moving mass impact onto the object, search velocity at the instance of impact and the duration of impact respectively. As clearly shown in Equation 9.2, with an increase of search velocity, the impact force must increase. As a result, the S-curve motion profile can increase the throughout of the finger gripper while it does not trade-off with its impact force performance.

With the implementation of mixed mode control strategy, there are a few precautions have to be considered. Firstly, the handling of transient mode changes have to be carefully taken care of. Once the contact is found, the trajectory controller injected a torque command, T_c into the nonlinear controller. In the next sample, when the control mode switch changes to force control and if the torque command T_f is not equal to T_c, then a sudden change in torque command appears and a sharp spike to force would be introduced. This could be harmful during grasping of delicate objects.

Secondly, the choice of search command is critical. If the search speed is low, e.g. $< 20\%$ of the maximum of the high-speed trajectory command, reducing the speed to zero before the start of search command is a preferable choice. This is because this allows more time for the finger to settle and damp out this vibration due to the acceleration of the trajectory command. This would perform a more stable constant search speed and leads to a more repeatability search *contact position*. However, if the search speed is high, it is not necessarily to reduce the trajectory command to zero. Since the constant search speed is a step command, this can easily excite the finger and as a result additional time is needed for the finger to damp away its vibration. Instead, when the speed of the trajectory command, S_{traj} is equal to the constant search speed, S_{srh} the speed command should hold at S_{srh} and search for the contact directly.

Thirdly, the *search position* must be carefully selected. The minimum *search position*, θ_{srhmin} allocated for the finger is described by the Equation 9.3.

$$\theta_{srhmin} = \theta_{vary} + S_{srh}T_{srh} \tag{9.3}$$

where θ_{vary} and T_{srh} represents the size variation of the object being grasped and the settling time for the search command respectively. Put it simply, the minimum *search position* must be far enough to include the variation of the grasping object and extra distance allocated for the search command to settle.

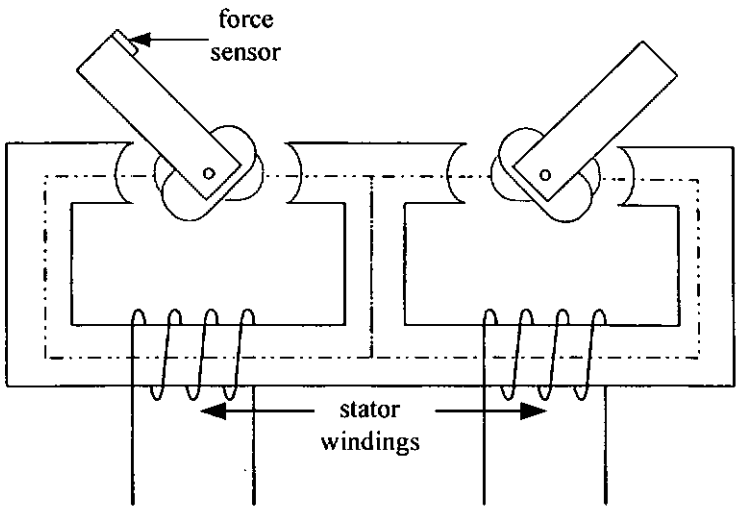

Figure 9.4: Force control setup for the two-finger VR gripper

In this force control strategy, the control loop suggested is open-loop instead of close-loop. Under close-loop force control, any force change shown in the environment can be immediately compensated with the control effort. However, this would increase the complexity of the controller. The accuracy with open-loop controller is guaranteed by assuming that the changes of friction and spring torque against θ_{vary} are not significant. Under these conditions, an open-loop force controller is satisfactory.

9.2 Implementation

Figure 9.4 shows the force control experimental setup for the two-finger VR gripper. In this experiment, a miniature quartz force sensor is mounted onto the contact surface of one of the finger. The force sensor's ground face and the mounting face needs to be flat and must be parallel with each other. This force sensor provides a signal sensitivity of $1N/V$ without external amplification. Apart from the force sensor, no additional hardware is required in this experiment. Implementing the mixed-mode control with command scheduling requires the controller system to monitor the position sensor, current and force sensor feedback, calculates the control signals and generates PWM signals to the current drivers correspondingly. With the force sensor connected to the 16-bits ADC channel, the force sensor has a resolution of $0.15mN$.

In this implementation, finger speed search is set at $15degs^{-1}$ or $0.262rads^{-1}$. Under such search speed level, it is better to allow the trajectory command to zero before start of search command. The finger *search position* is set at 8^o such that it satisfies the condition described in Equation 9.3 while minimizing the search time. Two force responses $600mN$ and $2N$ are measured.

9.3 Experimental results

Figure 9.5 and Figure 9.6 show the force profile responses of $600mN$ and $2N$. For each force profile responses, angular position, force measurement and stator current are recorded. With the assumptions mentioned in section 4.6, current, position and force responses in both fingers are assumed equal, only the left finger are shown.

Figure 9.5 shows force response for $600mN$. From Figure 9.5(a), it clearly shows that the entire motion sequence is divided into several stages as proposed. The motion begins at the initial *home position*. Fingers move from *home positions* with a fast trajectory profile to the pre-determined *search position* at 28^o. Current is also increased to $0.8A$ as the fingers rotate away from the *home positions* due to the increase in spring torque. Then the fingers close at a constant speed of $0.262rads^{-1}$ until the controller registers the force signal exceeds $10mN$ threshold point. At this instance, the contact position is found and the control mode switch changes from trajectory control to force control and the fingers hold at their *contact positions*. With the proposed low impact force profile, impact force is $100mN$. Then force profile generator ramps up to $600mN$ and holds for $50ms$ with current settles at $2.2A$. Then the force profile generator ramps begin with the impact force until it reaches the desired force level. Afterwards, the fingers open by removing current out of the stator winding. This allows the control mode switch changes back to trajectory control and return to their initial *home positions*. During the retreat motion, force is sharply removed and no bouncing is found.

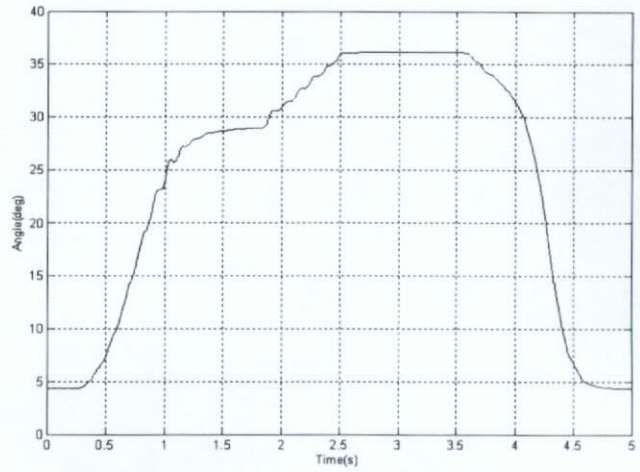

(a) angular position

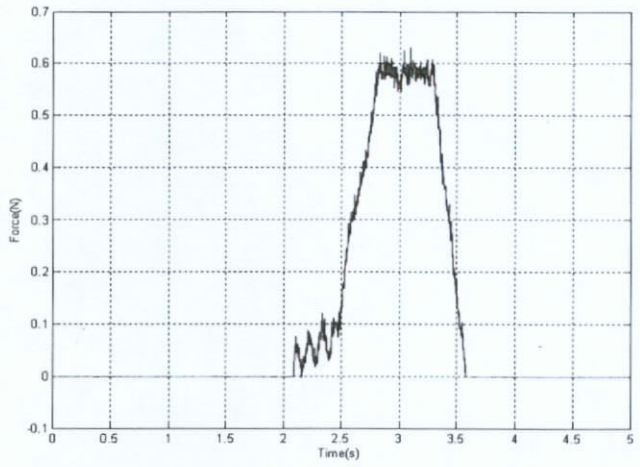

(b) force response

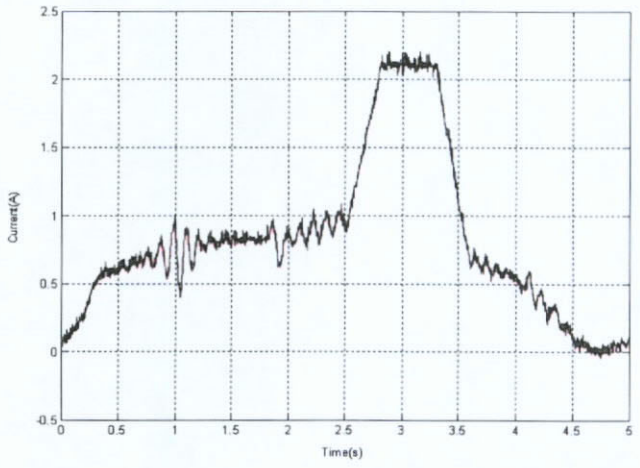

(c) current

Figure 9.5: 600mN force response of the two-finger VR gripper

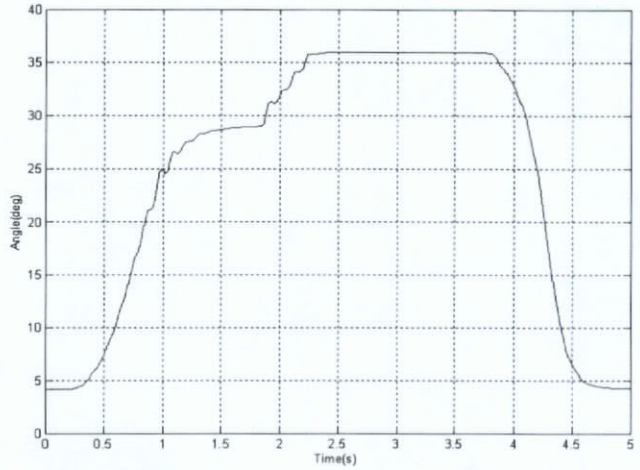

(a) angular position

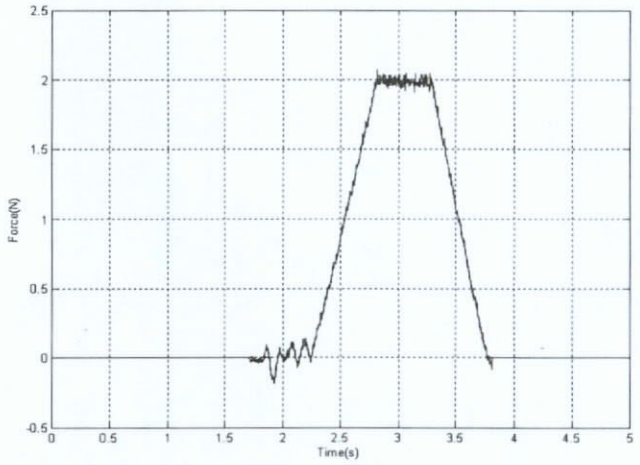

(b) force response

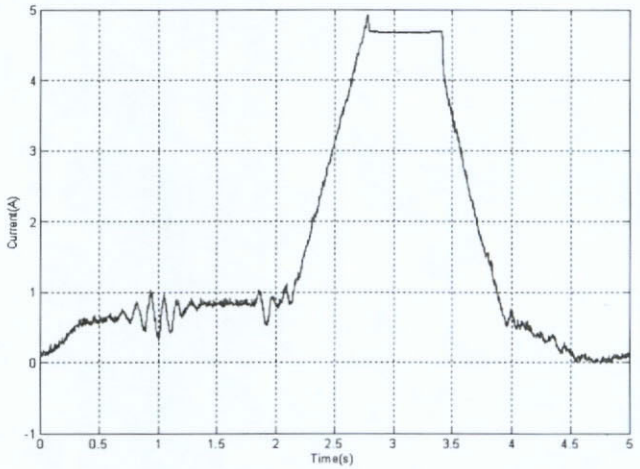

(c) current

Figure 9.6: 2N force response of the two-finger VR gripper

Similarly, Figure 9.6 shows $2N$ force responses. The entire motion sequence is same as the previous one. During the high-speed trajectory motion and search contact motion, the trajectory response, slope of the search contact motion and current waveform are the same as Figure 9.5(c) as expected. The main difference occurs when the fingers hit the object being grasped is found. At this instance, the control mode is switched to force control and force command ramps up to $2N$. However, since the force command has to ramp up to $2A$ within the same period of time, the slope of force response is much steeper than the $600mN$ one with its current level peaks at $4.6A$. After the gripping force holding time is expired, the fingers retreat to their *home positions* and once again, the current waveform behaves similarly to the former one.

Before any contact occurs, the force sensor shows no signal. On the other hand, once the fingers grasp the object, the angular positions are fixed and last for the duration of gripping force holding time. In addition, Figure 9.5(c) and Figure 9.6(c) show that the force constant of the two-finger VR gripper is obviously not a fixed value. At steady state of the force responses, the force constant for $600mN$ and $2N$ are $0.27N/A$ and $0.43N/A$ respectively. By merely comparing these two force responses, it clearly indicates that once the efficiency of the VR finger gripper is doubled, when the current level drives it into the saturation. This efficiency can be further increased if the *contact position* coincides with the overlapping position of the stator and rotor poles where significant flux-linkage saturation can be found.

9.4 Summary

In this chapter, a high-precision position and force algorithm is proposed and implemented onto the two-finger VR gripper. This is achieved by a mixed-mode control with command scheduling. Noticing the fact that the linearization effect can be achieved by making use of the same nonlinear controller trajectory control and force control, therefore, two control modes, namely trajectory control and force control, and a control mode switch are incorporated. The trajectory control is achieved with close-loop control while the

force control is realized in an open-loop manner.

The entire trajectory profile for command scheduling and its flow chart are described in details. A low speed contact search is used to provide an accurate and repeatable means of finding the object being grasped while not introducing a large impact force onto it. Assumptions, determination of *search positions* and search speed are carefully selected. Then the implementation of the control algorithm is carried out and experimental results are recorded.

Force responses of $600mN$ and $2N$ are recorded. These two different force levels represent the two different operating regions of the two-finger VR gripper which are the linear and saturation regions. Results show that the trajectory responses are same for both force response. However for $2N$ force response, with a high required force, the slope of the force command is steeper than the other one. With the implementation of the low search speed profile, low impact force of $100mN$ can be found. When the two-finger VR gripper operates within the saturation region, experimental results further confirmed that efficiency can be doubled. By choosing the *contact positions* at the overlapping positions of the stator and rotor poles, efficiency can be further increased due to the significant flux-linkage saturation effect.

Experimental results confirmed that the two-finger VR gripper is simple, low-cost and at same time capable in delivering gripping force efficiently. This solution can be widely accepted in industrial gripping applications with its high-precision gripping performance.

Chapter 10

Conclusions

This thesis describes a novel and unique two-finger gripper utilizing VR technology. This thesis also describes the needs, design, analysis, construction, characterisation, modeling and implementation of the two-finger VR gripper. This conclusion chapter summaries the research work and findings in four different areas.

Section 10.1 concludes the work done relating the actuator, ranging from its design analysis and construction. Then characterisation techniques, instrumentation and modeling simulation are concluded in section 10.2. After that, the work related to the control methods and techniques their simulation and eventually implementation, are summarized in section 10.3. Then, achievements of this research work is summarized in section 10.4. Finally, further work for this research project are suggested in section 10.5.

10.1 On the actuator

This research aims at developing a novel two-finger gripper using VR technology taking the advantages of high-torque efficiency, robust characteristics and simple construction. The needs to develop a new finger gripper are addressed. It was found that the VR motors matches most of the requirements for an ideal gripper. In addition, the production and material cost of a VR motor is extremely low. This is found to be extremely attractive to a highly demanding market. After investigating the developed grippers, these grippers fail

to fulfill the purposes of an ideal gripper. The main problem associated with VR motor is its uneven torque ripple originated from its unique torque generating principle. With the advent of semiconductor industries, costs of microprocessors are lowered. Advanced control algorithm can be now realized to solve the nonlinearity problems of VR actuators.

To design a two-finger gripper, various types of two-finger VR gripper have been proposed. Besides, it has shown that energy conversion analysis is most suitable for analysing the magnetic circuit in the VR gripper especially in the presence of magnetic saturation. Analysis shows that by combining the magnetic circuits, the finger gripper has higher torque efficiency than separate magnetic circuits. Next, the coupled two-finger VR gripper was fabricated. This finger gripper is the first gripper making use of VR technology. Direct torque measurement verified that the analysis is correct and it generates higher torque with combined magnetic circuits by more than 30% at $4A$ current level.

10.2 On the modeling simulation

In order to describe the finger gripper accurately, a mathematical model was built to identify all the parameters within the model. Amongst all, magnetic flux-linkage measurement is of the most difficult. AC current excitation method is chosen to be the most appropriate and flux-linkage measurement is implemented with the controller platform. A series of measurement of flux-linkage versus current and angular position is then carried out. Measurement results reveals that the two-finger VR gripper has magnetic characteristics similar to a rotary VR actuator. Spring constant and other losses parameters are measured and estimated to complete the characterisation of the two-finger gripper. Core losses and eddy current losses are confirmed to be negligible. However, it is necessary to incorporate leakage flux-linkage into the model.

Basing on these information, a third order dynamic model described with states equations is constructed. This model includes the nonlinear magnetic characteristics

modeled with an exponential function. For modeling simplicity, some information including friction and core losses are omitted from the dynamic model.

Simulation model of the two-finger VR gripper model is verified with current step responses. Experimental result matches closely with the simulation. This shows that the two-finger VR gripper is accurate enough for controller design and simulation purposes.

10.3 On the control

Various innovative control algorithms have been proposed, simulated and implemented.

10.3.1 Current regulation

On the control perspective, a few important contributions have been made. Firstly, an adaptive current regulation method was proposed. With the measured nonlinear flux-linkage characteristics, it has been investigated that current loop response varies at different current levels and angular positions. This might be acceptable for general control purposes provided that the control specifications are not stringent. However, for high-precision applications, especially for gripping of delicate objects, slight oscillations within the current loop affects the performance at outer loops. As a result, an adaptive current regulation method is proposed.

In the investigation, it is found that commonly used current regulations are not capable of handling load variations and system nonlinearity. In this proposed method, the nonlinearity is included into the controller design and simulation. In this research, both the fully digital PI current regulation and the adaptive PI current regulation has been implemented, tested and verified. Results show that the adaptive PI current regulator has been successfully developed and it can provide superior performance on a load with wide variation in inductance. This is especially useful in the current regulation of switched reluctance motors, because their reluctance variation can be as high as 3–5 times.

10.3.2 Nonlinear compensation

After that, it is important to develop a novel nonlinear compensator to tackle the nonlinear behavior of the VR finger gripper. In this research, different methods have been reviewed and finally two methods have been proposed and implemented, namely reduced order lookup table compensator and PBC controller.

The former method is found to be extremely easy to implement and comprehend. However, its main deficiency is its fail to show global convergence and robustness. Consequently, another approach, PBC is proposed. This approach is a modern controller design concept making use of energy transformation. It treats its state variables as energy and with energy transformation, i.e. energy shaping and damping injection, to perform the desired control actions. The PBC controller guarantees global asymptotic convergence and stability. It also inherits certain extent of robustness against parameter variations and modeling error.

Both mentioned methods are implemented onto the controller platform. Measured results confirmed that the PBC controller is more favorable than the reduced order lookup table compensator. Results also show that its stability is robust against parameter variation and it converges asymptotically.

10.3.3 Position and force control

On the last stage of the work, a mixed-mode control with command scheduling control algorithm is proposed and implemented. For simplicity, a classical PID trajectory controller is used. The closed-loop system is simulated and result show that it is stable and capable of achieving high-accuracy. An S-curve trajectory command is implemented to reduce the mechanical stress onto the gripper and settling time. For force control, a simple control mode switch is added to the controller. This switch receives different commands under different conditions. Lastly, the controller is implemented and measured

results demonstrate that the system has good force accuracy. It can be an alternate solution to gripping mechanism.

10.4 Achievements of this research work

The achievement of this research work can be summarized as followed:

1. Designed an innovative mutually coupled two-finger VR gripper. Various commonly found gripping mechanisms have been reviewed. By making use of the VR technology, the gripper can benefit from low EMI and reduction in manufacturing costs. In addition, torque production is further raised by combining the magnetic circuits of the two VR motors of the finger gripper. Direct torque measurement confirmed that torque production is increased by $> 30\%$ compared with the ordinary non-coupled VR finger gripper.

2. Researched into general flux-linkage modeling methods employed by general VR motors. Flux-linkage characteristics of the VR finger gripper with respect to current levels and angular positions are examined. Amongst all the methods reviewed, exponential description function is found to be the most appropriate and cost-effective for modeling the two-finger VR gripper. Modeling simulation and experimental responses show that the constructed model is accurate enough for controller design and simulation purposes.

3. Proposed and implemented the adaptive current regulator for the two-finger VR gripper. Noticing the significant flux-linkage variation of the two-finger VR gripper, an adaptive current regulation scheme is proposed and implemented. With the ordinary PI current regulators, current response suffers from significant overshoot and asymmetric responses. In the proposed adaptive current regulation scheme, flux-linkage variation is continuously monitored. To adapt to such changes, control parameters are varied accordingly such that same current responses can be guaranteed despite the changes of angular positions and current levels. Simulation and experimental results show that the proposed adaptive current regulator can

adapt to load variations and provide same current responses at all operating current levels and angular positions. This solution can also be applicable in general VR motors which suffer from the same problem.

4. Proposed and implemented two nonlinear compensators for the two-finger VR gripper. The first method bases on the reduced-order lookup table method and the second one is the PBC method. Reduced-order lookup table is a simple, easy-to-comprehend and low-cost nonlinear compensator for the two-finger VR gripper. With a small amount of flux-linkage data being recorded in the controller, the nonlinear effect of the two-finger VR gripper can be linearized with bi-linear interpolation. Results show that the reduced-order lookup table method is applicable in tackling the nonlinear problem. However, for high-precision applications, an advanced and efficient algorithm is required.

   The second method, PBC, designs a controller basing on the transformation of energy. Several advantages can be found using PBC. This method guarantees global asymptotic convergence, system stability and inherits certain degrees of robustness. Such controller design method is the first time being implemented onto VR motors. Experimental results show that the trajectory performance offered by the PBC controller is more favorable compared with the reduced-order lookup table. Dynamic and steady state trajectory errors is maintained within 1.5^o and 0.09^o respectively.

5. Proposed and implemented a force control algorithm using a mixed-mode control with command scheduling. For high-speed and high-precision grasping of delicate objects, a force control algorithm using mixed-mode control with command scheduling is proposed. At different operating stages, different trajectory or force commands are injected into the nonlinear PBC controller of the two-finger VR gripper. Precautions are carefully taken to prevent sudden force spikes to occur during the contact in particular control mode transitions. Experimental results show that the proposed algorithm can successfully maintain the impact force within $100mN$. It is also confirmed that the two-finger VR gripper is capable of delivering higher gripping force at saturation region and doubling its efficiency.

10.5 Suggestions for further research

To further improve the research project, a few of areas are required to explore and develop.

1. FEM analysis can be incorporated into the early design stage. With the aid of FEM analysis, certain parameters of the two-finger VR gripper can be optimized and thus improve its overall efficiency. Besides, thermal management can be considered at the design stage. In addition, simulated magnetic and nonlinear characteristics can be produced. Then simulation result can be provided before the actual gripper construction being made. All these can benefit the gripper as a whole.

2. Developing a position estimation technique for the two-finger VR gripper is a good way in extending its application and robustness. This can be achieved with additional information feed back to the controller, for example, voltage, instantaneous change of inductance etc. With position estimation, sensorless control can be applied. The entire finger gripper system does not have any electronics system incorporated. Consequently, it can then be operated at extremely wide range of temperature, further reduced in cost and increased in reliability.

Appendix

List of publications generated from this research project

Journal Papers

[1] N. C. Cheung, P. JianFei, G. W. Chuen, and K. K.-C. Chan. Using variable reluctance actuators in automated manufacturing machines. *Invited Paper, Power Supply Technologies and Applications*, 4(7):17–23, April 2004.
Available from: `http://www.china-power.net/6zhounian/2.htm`.

[2] J. M. Yang, X. Jin, J. Wu, N. C. Cheung, and K. K.-C. Chan. Passivity-based control incorporating trajectory planning for a variable-reluctance finger gripper. *Proceedings of the Inst. of Mechanical Engineers Part I Journal of Systems and Control Engineering*, 218(2):99–109, April 2004.

[3] K. K.-C. Chan and N. C. Cheung. A novel two-finger variable-reluctance gripper for high-speed grasping of delicate objects: an implementation case study. *IEEE Transactions on Industrial Electronics - accepted for published*, December 2004.

[4] K. K.-C. Chan, J. M. Yang, and N. C. Cheung. Passivity-based control for flux regulation in a variable reluctance finger gripper. *IEE Proceedings - Electrical Power Applications - accepted for published*, December 2004.

[5] K. K.-C. Chan and N. C. Cheung. Modelling and characterisation of a novel two-finger

variable reluctance finger gripper. *ISA Transactions - The Science and Engineering of Measurement and Automation - accepted for published*, December 2004.

Conference Proceedings

[1] N. C. Cheung and K. K.-C. Chan Magnetic modeling of a mutually-coupled two-finger variable reluctance gripper. In *28th Annual Conference of IEEE Industrial Electronics Conference*, volume 4, pages 2733–2738, November-December 2002.

[2] N. C. Cheung. and K. K.-C. Chan Pid control of a novel variable reluctance gripper. In *27th Annual Conference of IEEE Industrial Electronics Conference*, volume 1, pages 456–461, November-December 2001.

[3] K. K.-C. Chan and N. C. Cheung. Grasping of delicate objects by a novel two-finger variable reluctance gripper. In *36th Annual Conference of Industrial Application Society*, volume 3, pages 1969–1974, September-October 2001.

[4] K. K.-C. Chan and N. C. Cheung. Modelling and characterisation of a novel two-finger variable reluctance gripper. In *16th Annual IEEE Applied Power Electronics Conference and Exposition*, volume 2, pages 1116–1120, March 2001.

[5] K. K.-C. Chan, S. W. Tam, and N. C. Cheung. Adaptive current control of a variable reluctance finger gripper. In *Annual International Power Electronics Conference*, volume 1, pages 260–265, 2001.

[6] K. K-C. Chan and N. C. Cheung Modeling and characterisation of high performance variable reluctance finger gripper In *Annual International Power Electronics Conference*, volume 1, pages 370–375, 2001.

References

[1] M. I. Angulo-Núñez and H. Sira-Ramírez. Flatness in the passivity based control of dc-to-dc power converters. In *Proceedings of the 37th Conference on Decision and Control*, volume 4, pages 4115–4120, December 1998.

[2] K. J. Åström and B. Wittenmark. *Adaptive Control.* Addison-Wesley, USA, second edition, 1995.

[3] F. Blaabjerg, P. C. Kjaer, P. O. Rasumussen, and C. Cossar. Improved digital current control methods in switched reluctance motor drives. *IEEE Transactions on Power Electronics*, 14(3):563–572, May 1999.

[4] S. A. Bortoff, R. R. Kohan, and R. Milman. Adaptive control of variable reluctance motors: A spline function approach. *IEEE Transactions on Industrial Electronics*, 45(3):433–444, June 1998.

[5] D. G. Caldwell, G. A. Medrano-Cerda, and M. Goodwin. Control of pneumatic muscle actuators. *IEEE Control Systems Magazine*, 15(1):40–48, 1995.

[6] D. G. Caldwell and N. Tsagarakis. Soft grasping using a dextrous hand.

[7] H.-D. Chai. *Electromechanical Motion Devices.* Prentice-Hall PTR, USA, 1998.

[8] K. K.-C. Chan and N. C. Cheung. Modelling and characterisation of a novel two-finger variable reluctance finger gripper. *ISA Transactions - The Science and Engineering of Measurement and Automation - accepted for published.*

[9] K. K.-C. Chan and N. C. Cheung. A novel two-finger variable-reluctance gripper for high-speed grasping of delicate objects: an implementation case study. *IEEE Transactions on Industrial Electronics - accepted for published.*

[10] K. K.-C. Chan and N. C. Cheung. Grasping of delicate objects by a novel two-finger variable reluctance gripper. In *36th Annual Conference of Industrial Application Society*, volume 3, pages 1969–1974, September-October 2001.

[11] K. K.-C. Chan and N. C. Cheung. Modelling and characterisation of a novel two-finger variable reluctance gripper. In *16th Annual IEEE Applied Power Electronics Conference and Exposition*, volume 2, pages 1116–1120, December 2001.

[12] K. K.-C. Chan, S. W. Tam, and N. C. Cheung. Adaptive current control of a variable reluctance finger gripper. In *Annual International Power Electronics Conference*, volume 1, pages 260–265, 2001.

[13] K. K.-C. Chan, J. M. Yang, and N. C. Cheung. Passivity-based control for flux regulation in a variable reluctance finger gripper. *IEE Proceedings - Electrical Power Applications - accepted for published.*

[14] A. D. Cheok and N. Ertugrul. Computer-based automated test measurement system for determining magnetization characteristics of switched reluctance motors. *IEEE Transactions on Instrumentation and Measurement*, 50(3):690–696, June 2001.

[15] N. C. Cheung. *A Nonlinear, Short Stroke Proportional Solenoid.* PhD thesis, The University of New South Wales, Australia, Sydney, July 1995. 311 pages.

[16] N. C. Cheung. A compact and robust variable reluctance actuator for grasping applications. In *24th Annual Conference of the IEEE Industrial Electronics Society*, volume 2, pages 1072–1076, August/September 1998.

[17] N. C. Cheung and K. K.-C. Chan. Pid control of a novel variable reluctance gripper. In *27th Annual Conference of the IEEE Industrial Electronics Society*, volume 1, pages 456–461, November/December 2001.

[18] T.-S. Chuang and C. Pollock. Robust speed control of a switched reluctance vector drive using variable structure approach. *IEEE Transactions on Industrial Electronics*, 44(6):800–808, December 1997.

[19] D. H. Cowden. Torsional springs [online]. 1995. Available from: `http://www.srl.gatech.edu/vprs/primer/torsion.htm`.

[20] M. R. Cutkosky. On grasp choice, grasp models, and the design of hands for manufacturing tasks. *IEEE Journal of Robotics and Automation*, 5(3):269–279, June 1989.

[21] dSPACE. dspace catalog ds1104 [online]. 2004. Available from: `http://www.dspace.de/shared/data/pdf/katalog2004/dspace_catalog2004_ds1104.pdf`.

[22] H. Du, C. Su, M. K. Lim, and W. L. Jin. A micromachined thermally-driven gripper: a numerical and experimental study. *Smart Material Structure*, 8:616–622, 1999.

[23] M. Ehsani, I. Husain, and K. R. Ramani. Low cost sensorless switched reluctance motor drives for automotive applications. In *IEEE Workshop on Electronic Applications in Transportation*, pages 96–101.

[24] G. Escobar and H. Sira-Ramírez. A passivity based-sliding mode control approach for the regulation of power factor precompensators. In *Proceedings of the 37th Conference on Decision and Control*, volume 3, pages 2423–2424, December 1998.

[25] P. D. Fenhout and C. F. Kurtz. Garden with insight v1.0 help: S curve [online]. May 1998. Available from: `http://www.gardenwithinsight.com/help100/00000467.htm`.

[26] A. Ferrero and A. Raciti. A digital method for the determination of the magnetic characteristic of variable reluctance motors. *IEEE Transactions on Instrumentation and Measurement*, 39(4):604–608, August 1990.

[27] A. Ferrero, A. Raciti, and C. Urzí. An indirect method for the n indirect method for the characteristization of variable reluctance motors. *IEEE Transactions on Instrumentation and Measurement*, 42(6):1020–1025, December 1993.

[28] A. E. Fitzgerald and C. Kingsley, Jr. *Electric Machinery.* McGraw-Hill, Tokyo, Japan, 1961.

[29] G. F. Franklin, J. D. Powell, and A. Emami-Naeini. *Feedback control of dynamic systems.* Addison Wesley, USA, second edition, 1991.

[30] P. I. GmbH and C. KG. Pic tutorial [online]. 2004. Available from: `http://www.piceramic.de/pdf/PIC_Tutorial.pdf`.

[31] A. A. Goldenberg, I. Laniado, P. Kuzan, and C. Zhou. Control of switched reluctance motor torque for force control applications. *IEEE Transactions on Industrial Electronics*, 41(4):461–466, August 1994.

[32] M. P. Groover, M. Weiss, R. N. Nagel, and N. G. Odrey. *Industrial robotics : technology, programming, and applications.* McGraw-Hill, New York, 1986.

[33] S. A. Hossain and I. Husain. A geometry based simplified analytical model of switched reluctance machines for real-time controller implementation. *IEEE Transactions on Power Electronics*, 18(6):1384–1389, November 2003.

[34] M. Ilic'-Spong, R. Marino, S. M. Peresada, and D. G. Taylor. Feedback linearizing control of switched reluctance motors. *IEEE Transactions on Automatic Control*, 32(5):371–379, May 1987.

[35] A. Isidori. *Nonlinear control systems: an introduction.* Springer-Verlag, New York, second edition, 1989.

[36] M. S. Islam, R. J. V. Iqbal Husain, and C. Batur. Design and performance analysis of sliding-mode observers for sensorless operation of switched reluctance motors. *IEEE Transactions on Control Systems Technology*, 11(3):383–389, May 2003.

[37] J. M. Kokernak and D. A. Torrey. Magnetic circuit model for the mutually coupled switched-reluctance machine. *IEEE Transactions on Magnetics*, 36(2):500–507, 2000.

[38] P. C. Krause, O. Wasynczuk, and S. D. Sudhoff. *Analysis of Electric Machinery and Drive Systems.* John Wiley and Sons Pub., USA, 2002.

[39] R. Krishnan. *Switched Reluctance Motor Drives : Modeling, Simulation, Analysis, Design, and Applications.* CRC Press, Boca Raton, Florida, 2001.

[40] P. J. Lawrenson, J. M. Stephenson, J. C. P. T. Blenkinson, and N. N. Fulton. Variable-speed switched reluctance motors. *IEE Proceedings - part B, electric power applications*, 127(4):253–265, 1980.

[41] P. Li and R. Horowitz. Passive velocity field control of mechanical manipulators. *IEEE Journal of Robotics and Automation*, 15(4), August 1999. Available from: `citeseer.ist.psu.edu/article/li99passive.html`.

[42] H. Liu, J. Butterfass, S. Knoch, P. Meusel, and G. Hirzinger. A new control strategy for dlr's multisensory articulated hand. *IEEE Control Systems Magazine*, 19(2):47–54, April 1999.

[43] R. D. Lorenz, J. J. Zik, and D. J. Sykora. A direct-drive, robot parts, and tooling gripper with high-performance force feedback control. *IEEE Transactions on Industry Applications*, 27(2):275–281, 1991.

[44] J. D. Lü and K. D. Zong. *General Electric Engineering and Electronics Handbook.* China Chemical Industry Press, Beijing, 1995.

[45] R. C. Luo, K. L. Su, and S. H. Phang. An implementation of gripper control using the new slipping detector by multisensor fusion method. In *26th Annual Conference of the IEEE Industrial Electronics Society*, volume 2, pages 888–893, 2000.

[46] T. J. E. Miller. *Brushless Permanent-Magnet and Reluctance Motor Drivers.* Oxford Science Pub., Oxford, 1989.

[47] T. J. E. Miller. *Switched Reluctance Motors and Their Control.* Magna Physics Publishing and Clarendon Press, Oxford, 1993.

[48] T. J. E. Miller. *Electronic Control of Switched Reluctance Machines.* Newnes Power Engineering Series, Oxford, 2001.

[49] S. Mir, I. Husain, and M. E. Elbuluk. Switched reluctance motor modeling with on-line parameter identification. *IEEE Transactions on Industry Applications*, 34(4):995–1000, July/August 1998.

[50] G. Monkman. Precise piezoelectric prehension. *Industrial Robot: An International Journal*, 27(3):189–193, 2000.

[51] N. J. Nagel and R. D. Lorenz. Rotating vector methods for smooth torque control

of a switched reluctance motor drive. *IEEE Transactions on Industry Applications*, 36(2):540–548, March/April 2000.

[52] S. A. Nasar, I. Boldea, and L. E. Unnewehr. *Analysis of Electric Machinery and Drive Systems*. CRC Press, USA, 1993.

[53] S. Y. Nof. *Handbook of industrial robotics*. John Wiley, New York, 1999.

[54] R. Ortega and G. Espinosa. Torque regulation of induction motors. *Automatica*, 29(3):621–633, 1993.

[55] R. Ortega, A. van der Schaft, B. Maschke, and G. Escobar. Energy-shaping of port-controlled hamiltonian systems by interconnection. In *Proceedings of the 38th Conference on Decision and Control*, volume 2, pages 1646–1651, December 1999.

[56] R. Ortega, A. J. van der Schaft, I. Mareels, and B. Maschke. Putting energy back in control. *IEEE Control Systems Magazine*, 21(2):18–33, April 2001.

[57] A. V. Radun. High-power density switched reluctance motor drive for aerospace applications. *IEEE Transactions on Industry Applications*, 28(1):113–119, January/February 1992.

[58] K. M. Rahman, B. Fahimi, G. Suresh, A. V. Rajarathnam, and M. Ehsani. Optimized torque control of switched reluctance motor at all operational regimes using neural network. *IEEE Transactions on Industry Applications*, 36(1):111–121, January/February 2000.

[59] K. M. Rahman, S. Gopalakrishnan, B. F. A. V. Rajarathnam, and M. Ehsani. Optimized torque control of switched reluctance motor at all operational regimes using neural network. *IEEE Transactions on Industry Applications*, 37(3):904–913, May/June 2001.

[60] K. M. Rahman and S. E. Schulz. High-performance fully digital switched reluctance motor controller for vehicle propulsion. *IEEE Transactions on Industry Applications*, 38(4):1062–1071, July/August 2002.

[61] V. Ramanarayanan, L. Venkatesha, and D. Panda. Flux-linkage characteristics of switched reluctance motor. In *Proceedings of the IEEE International Conference on Power Electronics, Drives and Energy Systems for Industrial Growth*, pages 281–285, 1996.

[62] D. S. Reay, M. Mirkazemi-Moud, T. C. Green, and B. W. William. Switched reluctance motor control via fuzzy adaptive systems. *IEEE Control Systems Magazine*, 15(3):8–15, June 1995.

[63] M. Rodrigues, P. J. C. Branco, and W. Suemitsu. Fuzzy logic torque ripple reduction by turn-off angle compensation for switched reluctance motors. *IEEE Transactions on Industrial Electronics*, 48(3):711–715, June 2001.

[64] C. Roux and M. M. Morcos. On the use of a simplified model for switched reluctance motors. *IEEE Transactions on Energy Conversion*, 17(3):400–405, September 2002.

[65] V. K. Sharma, S. S. Murthy, and B. Singh. An improved method for the determination of saturation characteristics of switched reluctance motors. *IEEE Transactions on Instrumentation and Measurement*, 48(5):995–1000, October 1999.

[66] G. R. Slemon. *Electric Machines and Drives.* Addison-Wesley Pub., Canada, 1980.

[67] G. R. Slemon and A. A. Straughen. *Electric Machines.* Addison-Wesley Pub., Canada, 1980.

[68] F. Soares and P. J. C. Branco. Simulation of a 6/4 switched reluctance motor. *IEEE Transactions on Aerospace and Electronic Systems*, 37(3):989–1009, July 2001.

[69] M. Stewart, M. G. Cain, and W. Battrick. Surface displacement mapping of piezoelectric multilayer actuators. In *Eighth International Conference on Dielectric Materials, Measurements and Applications*, pages 445–447, September 2000.

[70] M. Stiebler and K. Liu. An analyical model of switched reluctance machines. *IEEE Transactions on Energy Conversion*, 14(4):1100–1107, December 1999.

[71] P. Tando, A. V. Rajarathnam, and M. Ehsani. Self-tuning control of a

switched-reluctance motor drive with shaft position sensor. *IEEE Transactions on Industry Applications*, 33(4):1002–1010, July/August 1997.

[72] D. G. Taylor. An experimental study on composite control of switched reluctance motors. *IEEE Control Systems Magazine*, 11(2):31–36, February 1991.

[73] K. Uchino. *Piezoelectric actuators and ultrasonic motors.* Kluwer Academic Publishers, Boston, USA, 1997.

[74] X.-D. Xue, K. W. E. Cheng, and S. L. Ho. Simulation of switched reluctance motor drives using two-dimensional bicubic spline. *IEEE Transactions on Energy Conversion*, 17(4):471–477, 2002.